UNIVERSITY OF TWENTE.

ECN

Double wake model for separated flows over airfoils

A thesis submitted in partial fulfillment of the requirements for the degree of

Master of Science by

Rajesh Vaithiyanathasamy

Faculty of Engineering Technology - Engineering Fluid Dynamics

Sustainable Energy Technology

August 2017

EFD- 261

Assessment committee

Supervisor
Dr.ir. A. van Garrel
University of Twente.

Chairman
Prof.dr.ir. C.H. Venner
University of Twente.

Supervisor from company
Dr. H. Özdemir
ECN.

Supervisor from company
Dr. G. Bedon
ECN.

External member
Dr. G.G.M. Stoffels
University of Twente.

Abstract

Industry standard aerodynamic design tool RFOIL's performance can be improved at high angles of attack by incorporating the double wake inviscid model in the separated flow region. As a precursor, single wake inviscid model is developed using 2-D panel method to replicate the outcome of the standard tools. Then the double wake inviscid model is established on top with changes in the Kutta condition and local vorticity at the separation point. The solution is calculated by iterative procedure by establishing two wake sheets one from the trailing edge and the other from the separation point. The wake shapes are established from induced velocities of the airfoil vorticity distribution. The double wake inviscid model could establish better results than XFOIL and results closer to the experiment in the separated flow region over airfoils. This model can be combined with the viscous effects to mitigate the convergence problem at very high angles of attack with separated flows. Furthermore, improvement in the prediction of the lift coefficient is expected when this model is coupled with viscous effects calculations of RFOIL. As a second major study a dynamic stall model for pitching airfoils using modified Leishman-Beddoes (LB) method for wind turbine application is implemented. The implementation combines the best of two previous implementations. One is the usage of separation point function from Theordorsen theory instead of empirical relations. The other is the inclusion of the lift contribution from leading edge vortex formation. The model successfully predicts the dynamic stall phenomena with small discrepancies when compared with experimental data.

Acknowledgements

This report is the result of the graduation work I performed as MSc student at the faculty of Engineering Fluid Dynamics at University of Twente. All of my work is performed at the Wind Energy Unit of Energy research Center of the Netherlands (ECN). There are several people who contributed towards completion of my MSc thesis.

Firstly, I would like to thank my academic mentor Dr.ir. A. van Garrel for his continuous guidance and input during the tenure of my master thesis. His support and availability has been invaluable.

I would also like to thank Dr. H. Özdemir for giving me the opportunity to do the thesis at the Energy research Center of the Netherlands. I am grateful to both my supervisors at ECN Dr. H. Özdemir and Dr. G. Bedon for their technical guidance and timely inputs. I really appreciate the pleasant and unconstrained working environment that was given by my supervisors which helped me finish the work successfully.

Further, I would like to thank the Chair Engineering Fluid Dynamics, Prof.dr.ir. C.H. Venner for his valuable time and encouragement during the interim meeting. Also, I like to thank his secretary Brenda Benders for answering all my queries patiently. I am equally thankful to Dr. Kisorthman Vimalakanthan and Dr. Marco Caboni at ECN for their insight and discussions during the course of my thesis. Also, I am very much grateful to Shafiek Ramdin for his useful reviews.

I gratefully acknowledge the scholarship provided by the University of Twente for doing my MSc study. Without this scholarship it would not have been possible to do my studies in University of Twente.

Last but not least, I would like to thank my friends, family and my girlfriend for putting up with me during this period and I want to dedicate my work to them.

Declaration

I declare that, this written submission represents my ideas in my own words and where others' ideas or words have been included. I have adequately cited and referenced the original sources. I declare that, I have properly and accurately acknowledged all sources used in the production of the thesis. I also declare that, I have adhered to all the principles of academic honesty and integrity and have not misrepresented or fabricated or falsified any idea/data/fact/source in my submission.

Contents

List of Figures

Acronyms

AoA Angle of Attack.

CFD Computational Fluid Dynamics.

ECN Energy research Center of the Netherlands.

IBL integral boundary layer.

LB Leishman-Beddoes.

SA Spalart Allmaras.

SU2 Stanford University Unstructured (an open source CFD solver).

List of symbols

Alphanumeric

a_x	distance along x axis between the collocation point and the beginning of each panel in panel coordinates	m
b_x	distance along x axis between the collocation point and the end of each panel in panel coordinates	m
c	chord length	m
C	mean angle of attack	$^\circ$
C_d	drag coefficient	-
C_D	dissipation rate	-
C_f	skin friction coefficient	-
C_l	lift coefficient	-
$C_{l,\alpha}$	slope of lift coefficient in the attached flow regime	-
C_l^{circ}	lift coefficient due to circulatory loading	-
C_l^{ds}	dynamic potential lift coefficient	-
C_l^{ds}	Total lift coefficient	-
C_l^{fs}	lift coefficient for separated flow	-
C_l^{imp}	lift coefficient due to non-circulatory loading	-
C_l^{ps}	static potential lift coefficient	-
C_l^{vor}	vortex lift coefficient	-
C_p	pressure coefficient	-
c_y	distance along y axis between the collocation point and the end points of each panel in panel coordinates	m
D	amplitude for angle of attack	$^\circ$
d_1	distance between the collocation point and the beginning of each panel in panel coordinates	m
d_2	distance between the collocation point and the end of each panel in panel coordinates	m
f_{dy}	dimensionless dynamic separation point	-
f_{st}	dimensionless static separation point	-

H	shape factor	-
H_1	Head's shape parameter	-
h^-_{SEP}	pressure after separation point	$\mathrm{N\,m^{-2}}$
h^+_{SEP}	pressure before separation point	$\mathrm{N\,m^{-2}}$
H^*	energy shape parameter	-
k	reduced frequency	-
L	aerodynamic lift	$\mathrm{N\,m^{-1}}$
L_1	length from trailing edge till the separation point along the airfoil surface	m
L_2	length from the separation point till the trailing edge along the airfoil surface measured in the same direction	m
m	mass deficit	$\mathrm{m^2\,s^{-1}}$
N	number of airfoil panels	-
N_w	number of wake panels	-
q	total tangential velocity	$\mathrm{m\,s^{-1}}$
s	dimensionless time	-
t	maximum thickness of airfoil	-
t_1	angle corresponding to d_1 in panel coordinates	$^\circ$
t_2	angle corresponding to d_2 in panel coordinates	$^\circ$
T_f	time lag to account for the dynamic separation point	s
T_p	time lag for the delay in the dynamic stall onset	s
T_v	time lag for the vortex lift contribution	s
u	tangential velocity component	$\mathrm{m\,s^{-1}}$
U	total velocity	$\mathrm{m\,s^{-1}}$
U_0	freestream velocity	$\mathrm{m\,s^{-1}}$
U_1	tangential velocity at the beginning of each panel in panel coordinates	$\mathrm{m\,s^{-1}}$
U_2	tangential velocity at the end of each panel in panel coordinates	$\mathrm{m\,s^{-1}}$
U_{ac}	tangential velocity at the beginning of each panel in global coordinates induced by constant vortex singularity element	$\mathrm{m\,s^{-1}}$
U_{al}	tangential velocity at the beginning of each panel in global coordinates induced by linear vortex singularity element	$\mathrm{m\,s^{-1}}$
U_{bl}	tangential velocity at the end of each panel in global coordinates induced by linear vortex singularity element	$\mathrm{m\,s^{-1}}$
U_e	viscous layer edge velocity	$\mathrm{m\,s^{-1}}$
U_{ei}	inviscid velocity	$\mathrm{m\,s^{-1}}$
U_{ev}	viscous velocity	$\mathrm{m\,s^{-1}}$
u_l	local tangential velocity after the wake panel	$\mathrm{m\,s^{-1}}$
U_s	surface velocity	$\mathrm{m\,s^{-1}}$
u_u	local tangential velocity before the wake panel	$\mathrm{m\,s^{-1}}$

v	normal velocity component	$\mathrm{m\,s^{-1}}$
V	velocity	$\mathrm{m\,s^{-1}}$
W_1	normal velocity at the beginning of each panel in panel coordinates	$\mathrm{m\,s^{-1}}$
W_2	normal velocity at the end of each panel in panel coordinates	$\mathrm{m\,s^{-1}}$
W_{ac}	tangential velocity at the end of each panel in global coordinates induced by constant vortex singularity element	$\mathrm{m\,s^{-1}}$
W_{al}	normal velocity at the beginning of each panel in global coordinates induced by linear vortex singularity element	$\mathrm{m\,s^{-1}}$
W_{bl}	normal velocity at the end of each panel in global coordinates induced by linear vortex singularity element	$\mathrm{m\,s^{-1}}$
W_f	wake factor	-
W_h	wake height	m
W_l	wake length	m
x_1, x_2	x coordinate of the panel end points	m
y_1, y_2	y coordinate of the panel end points	m

Greek letters

α	angle of attack	$^\circ$
α_0	zero lift angle of attack	$^\circ$
α_0	static stall angle	$^\circ$
$\dot{\alpha}$	time derivative of angle of attack	$^\circ\,\mathrm{s^{-1}}$
α_E	effective angle of attack	$^\circ$
α_f	quasi-steady angle of attack	$^\circ$
α_j	panel inclination with respect to the global coordinate	$^\circ$
C_τ	shear stress coefficient	-
$C_{\tau_{eq}}$	equilibrium shear stress coefficient	-
δ	boundary layer thickness	m
Δ_1	panel length at separation point	m
Δ_2	panel length at trailing edge	m
Δh	pressure jump before and after the separation point	$\mathrm{N\,m^{-2}}$
δ^*	displacement thickness	m
δt	small time interval	s
γ	vortex singularity element	$\mathrm{m\,s^{-1}}$
γ_{SEP}	vortex singularity element at separation point	$\mathrm{m\,s^{-1}}$
Γ	total circulation	$\mathrm{m^2\,s^{-1}}$
Γ^t	circulation at time instant t	$\mathrm{m^2\,s^{-1}}$
γ_{TE}	vortex singularity element at trailing edge	$\mathrm{m\,s^{-1}}$
μ	dynamic viscosity	Pa s
ν	kinematic viscosity	$\mathrm{m^2\,s^{-1}}$

ω	rotational velocity	$\mathrm{rad\,s^{-1}}$
ϕ	indicial response function for circulatory load	-
Re_θ	critical Reynolds number	-
ρ	density	$\mathrm{kg\,m^{-3}}$
θ	momentum thickness	m
θ_{SEP}	separation point panel inclination angle	$^\circ$
θ_{TE}	trailing edge panel inclination angle	$^\circ$
ϕ	velocity potential	-
τ_w	wall shear stress	Pa
ξ	thin shear layer coordinate	-

Subscripts

0	free stream value	-
n	normal	-
t	tangential	-
i, j	counters	-
max	maximum value	-

Chapter 1

Introduction

1.1 Thesis objective

RFOIL is an engineering model for aerodynamic design of airfoils developed by ECN, NLR and TU Delft [7] that is based on XFOIL [8]. RFOIL has radial flow corrections, an addition of coriolis and centrifugal force (rotational effects) to the boundary layer, which solves steady state flows implementing a single wake from the trailing edge of the airfoil. This gives acceptable predictions for attached flows and flows with moderate separation. However, for flows with high separation the prediction of lift from RFOIL needs to be improved. One of the ways this can be done is by incorporating the continuous vorticity emitted at the separation point in the form of additional wake (i.e. double wake implementation). The main objective of the thesis is to develop an inviscid double wake model which could be later coupled with the viscous effects.

In engineering tools, panel method is used to model the inviscid flow around the airfoil using a doublet/vortex singularity elements. In the classical inviscid panel method, a single wake from trailing edge is released. The integral boundary layer equations are then solved using source terms on the airfoil surface and the wake, to get the mass deficit and account for the streamlines displacement away from the surface. Then the viscous effects are incorporated with the obtained inviscid solution using one of the available viscous-inviscid coupling procedures. In the proposed double wake implementation method for RFOIL, the second wake is released from the separation point in addition to the primary wake at the trailing edge to model the inviscid flow region. Then the source terms need to be coupled to get the mass deficit and eventually the final solution. The separation point required for modelling the second wake has to be given externally. The idea of double wake implementation can be extended to both conventional sharp trailing edge airfoils and blunt trailing edge airfoils. As the double wake model is developed to be implemented in the aerodynamic design tool RFOIL, all the illustrations that are referred throughout this thesis will be based on RFOIL.

The secondary objective is to develop a dynamic stall model for pitching airfoils.

1.2 Rationale for double wake model

The future generation of wind turbines increase in size to reap high power. These new design requires long blades and so the structural requirement demands thicker airfoils at the root section of the blade. This design of thick airfoils is the major challenge for the aerodynamicist. Thick airfoils exhibit flow separation at lower angles of attack than thin airfoils. The flow separation is the result of unfavourable pressure gradient due to flow deceleration developed by finite body width. For the thin body, the adverse pressure gradients are weak for moderate AoA and so the flow remains attached. As the body becomes thicker, the adverse pressure gradient becomes stronger leading to flow separation, recirculation, and vortex shedding. The existence of flow separation has been a major difficulty in the field of fluid dynamics and the design of thick airfoils only increases the difficulty to model the separation. When the flow separates, complex vortex shedding phenomena takes place behind thick bodies. It has been difficult to capture the correct phenomena even with the use of sophisticated Navier-Stokes equation set accompanied by turbulence models and also involves high computational cost as the flow region requires fine mesh refinement. When the flow separation occurs in thick airfoils, the usage of traditional engineering models combining the panel method and integral boundary layer (IBL) equations for solving the flow in the separation region also becomes inefficient for the following reasons: these models have convergence problem as the model assumption based on equilibrium flows is not anymore valid, when the flow is separated. The integral boundary layer equations along with the empirical closure sets can not handle the complex vortex shedding with the separated flow. Furthermore the turbulence closure sets associated with the integral boundary layer formulation is not simple to solve in separated flow region.

The shear layer in the separated region can be considered as negligible, as a result of continuous shedding of vorticity from the point of separation on the airfoil surface. Hence, to predict the correct behaviour of the separated flow, for a cost effective model than the detailed CFD, a model capturing the vortex shedding from separation point needs to be employed. The flow in the separated region has negligible vorticity leading to negligible losses and constant total pressure. Therefore, the flow can assumed to be purely inviscid and the separated region can be modelled without the integral boundary layer (IBL) formulation. The non-separated flow region is modelled using panel method combined with IBL equations. The concept of double wake is to model the separated region with a wake from the trailing edge and another wake from the separation point with the separated reversed flow in between the two wakes. The continuous vortex shedding from the separation point and the trailing edge can be calculated using streamlines as the wakes. Due to vorticity shedding, the velocity gradients becomes smaller and reaches zero. The zero-gradient situation is enforced in the potential flows through the Kutta condition. With the influence of the vorticity on both the wakes enclosing the separated region and a suitable Kutta condition an unique solution of constant pressure region can be obtained.

1.3 Research approach and methodology

To accomplish the goal of the thesis, following steps are taken in a systematic manner.

Main objective

- Learning panel method, RFOIL source code and previous works on double wake models.
- Creating FORTRAN algorithm to model inviscid flow using 2D panel method.
- Validating the model with industry standard tools.
- Developing inviscid double wake model to represent the separated flow over airfoils.
- Testing and validating with experimetal and numerical results.

Secondary objective

- Learning existing dynamic stall models.
- Implementing a semi-empirical dynamic stall model for wind turbines.

1.4 Thesis layout

To meet the main objective of developing the double wake inviscid model, literature study is carried out indicating some of the previous works in chapter 2. A general description of inviscid flow modelling is given in chapter 3. A single wake inviscid model is developed and compared with the industry standard aerodynamic design tools, XFOIL and RFOIL. This is followed by necessary corrections to accurately replicate the results of the tools. This is also shown in chapter 3. Following this, different procedures are attempted to model the double wake inviscid method. Chapter 4 shows them along with the successful implementation methodology. Chapter 5 is concerned with the results of the double wake inviscid model and its comparison to experimental data and numerical results including one from XFOIL. Chapter 6 is dedicated to the secondary objective of dynamic stall model for pitching airfoil showing different dynamic stall models and implementation of one such model along with the experimental comparison. The conclusions analyzing the double wake inviscid model with its drawback and possible ways of improvements are indicated in chapter 7.

Chapter 2

Literature review

The size of the wind turbines increases in order to extract maximum power from the available wind. This requires wind turbines to operate at very high Reynolds numbers. For most of the flow fields, only potential flow can be considered. However, even at these high Reynolds numbers, closer to the solid boundary, the effect of viscous layer cannot be neglected. In order to predict drag effectively, boundary layer and wake calculations need to be included along with the inviscid flow calculations. Industry standard aerodynamic desgin tools i.e. (XFOIL or RFOIL [7, 8, 9, 10]) solve the inviscid flow around the airfoil using panel methods coupled with an IBL formulation to account for viscous effects. The methodology in the aerodynamic desgin tools involves inviscid formulation, boundary layer formulation and coupling of viscous-inviscid solutions.

2.1 Inviscid formulation

The region around airfoil where the flow has negligible viscous effects is called as inviscid region. The inviscid flow over airfoil has no vorticity i.e. $\nabla \times V = 0$, due to the absence of the shear layer and so it is irrotational (the flow has only translation motion and no angular velocity). The flow over the wind turbine blades are subsonic and the assumption of this flow as incompressible holds good as isentropic variation of density in this Mach number regime is negligible. Hence, most of the flow field over wind turbine blades can be considered as inviscid, incompressible, irrotational flow. This case is called potential flow and simplifies the differential equations used to describe the flow. In contrast with using velocity components as unknowns, requiring several equations to represent the velocity components, only velocity potential need to be solved. Therefore only one equation is required to describe the potential flow field. Once the velocity potential is calculated, the velocity component can be directly obtained from it, thus facilitating easy solution.

To compute the potential flow over airfoil, there are two methods namely, classical small disturbance and numerical panel method. The former approach does not account for the effect of thickness on airfoil lift effectively. This method can be applied only with major geometry simplification and the boundary conditions used are applied to these simplified surfaces. On the other hand, numerical panel method can be used for more realistic geometries. This method focusses on calculating combination of elementary flows on the body surface of the airfoil rather than CFD methods like finite difference and finite volume methods where the focus is on the entire fluid volume. The elementary flows can be described by means of *source*(σ), *doublet* (μ) or *vorticity* (γ) and are used in combination. The *sources* are used to represent the thickness of the airfoil. Other aerodynamics properties are described by the *doublet* or *vorticity* elementary methods. It is to be noted that *doublet* element of n^{th} order is equivalent to the *vorticity* element of $(n-1)^{th}$ order in terms of accuracy and so implementation of *vorticity* is a preferred option [6]. In order to account for the continuous surface with aerodynamics properties, the airfoil surface can be divided into large number of small panels with point, constant, linearly varying, quadratic varying strength singularity elements described in each panel. The point elements are inefficient near stagnation point of thick airfoils. The constant element gives pressure distribution accurately but results in singularity in panel edges and so linearly varying strength elements are used in RFOIL. Any higher order elements can be used to increase the accuracy but involve difficulty in implementation.

In RFOIL the surface geometry of airfoil is represented by flat panels for simplicity. The streamline is expressed as a combination of freestream velocity, source distribution to couple the viscous effects and vortex distribution for aerodynamics effects (mainly C_l) and the wake. The wake is modelled as per Kutta condition which states that the fluid leaving the trailing edge must be smooth, i.e. velocity leaving the airfoil trailing edge from both suction and pressure side must be equal or zero in magnitude. The formulated streamline equation is implemented with solid wall boundary condition to calculate the strength of each elementary flows (vortex) described. The zero normal flow boundary condition can be prescribed by ϕ (Dirichlet) or v (Neumann) equals zero, to solve for the unknown singularity strength and obtain the pressure distribution which corresponds to direct panel method [8]. However, an inverse panel method is also possible, whereby the airfoil geometry is modelled based on the input pressure distribution. The numerical solution can be improved by change of grid spacing, panel density, wake model, boundary condition, collocation points.

2.2 Boundary layer formulation

The boundary layer can be solved by either one equation or two equation method [6, 11, 12]. The one equation model from Thwaites solves the boundary layer in terms of the parameter λ and so it is faster and stable for attached flows.

$$\frac{U_e\theta}{\nu}\frac{d\theta}{dx} + (H+2)\frac{\theta^2}{\nu}\frac{dU_e}{dx} = \frac{\tau_w\theta}{\mu U_e}. \tag{2.1}$$

The profile shape parameter function λ is given by

$$\lambda = \frac{\theta^2}{\nu}\frac{dU_e}{dx}. \tag{2.2}$$

In the one equation method, the pressure and velocity as calculated from the inviscid flow are used to find the boundary layer properties. For separated flows, on integration, this leads to singularity at trailing edge and at separation point when steady-state solution is considered. So a stronger formulation is necessary where the inviscid and viscous part are not solved separately but coupled in a manner as shown in section (2.3).

The two equation method involves von Karman momentum equation and kinetic energy shape parameter equation in the integral form to calculate displacement thickness δ^* and momentum thickness θ and given by the equations (2.3) and (2.4) respectively.

$$\frac{d\theta}{dx} + (H+2)\frac{\theta}{U_e}\frac{dU_e}{dx} = \frac{C_f}{2}, \tag{2.3}$$

$$\theta\frac{dH^*}{dx} + (1-H)H^*\frac{\theta}{U_e}\frac{dU_e}{dx} = 2C_D - H^*\frac{C_f}{2}. \tag{2.4}$$

where, H is the shape factor, U_e is the velocity at the edge of the boundary layer, C_f is the skin friction coefficient, C_D is the dissipation coefficient and H^* is the kinetic energy shape parameter. Furthermore, e^n transition and lag-entrainment equations given by [13], are used for laminar/ transition and turbulent flows respectively. The e^n transition model is used to predict transition location and to determine associated losses with bubble size and given by,

$$\begin{aligned} \frac{d\bar{n}}{d\xi}(H_k,\theta) &= \frac{d\bar{n}}{dRe_\theta}(H_k)\frac{f_1(H_k)+1}{2}f_2(H_k)\frac{1}{\theta}, \\ \bar{n}(\xi) &= \int_{\xi_0}^{\xi}\frac{d\bar{n}}{d\xi}d\xi, \end{aligned} \tag{2.5}$$

where, ξ_0 is at $Re_\theta = Re_{\theta 0}$. ξ is the shear layer coordinate, Re_θ is the momentum thickness Reynolds number, $Re_{\theta 0}$ is the critical Reynolds number, $\bar{n}$ is the transition amplification variable, H_k is the kinetic shape parameter, f_1 and f_2 are the empirical functions of H_k. The lag-entrainment equation used for turbulent flow to incorporate the response of shear stress to the flow is

$$\frac{\delta}{C_\tau}\frac{dC_\tau}{d\xi} = 4.2(C_{\tau EQ}^{1/2} - C_\tau^{1/2}). \tag{2.6}$$

where C_τ and $C_{\tau EQ}$ are the shear stress coefficient and equilibrium shear stress coefficient respectively. With these equations the system is not closed as the unknowns are more than the number of equations available and so six closure sets are used. The closure sets are for skin-friction coefficient C_f, head's shape parameter versus shape parameter H_1-H, energy shape parameter versus shape parameter H^*-H, equilibrium shear stress $C_{\tau_{eq}}$, surface velocity U_s, dissipation rate C_D based on empirical relations. XFOIL has different closure relations for laminar, transition and turbulent flows as described in [11]. The XFOIL version of 5.4 is being used to develop RFOIL. The laminar closure relations are unchanged in RFOIL as the radial flow influence is very little for the boundary layer of the attached laminar flow. For transition region, Eppler's semi-empirical bubble transition model ([14]) is a better simplication to the e^n model used by Drela [7]. However, the former is insensitive to pressure changes, unreliable near extreme conditions and is difficult to implement and so the same relations are used as in XFOIL. Some changes are done to the turbulent boundary layer closure sets in RFOIL. The lag equation for turbulent boundary layer is based on equilibrium flow which is far from the practical situations especially with turbulent separation and transition regions. The closure sets for the first three of the variables mentioned above are same for XFOIL and RFOIL. However, the closure set for $C_{\tau_{eq}}$, U_s, C_D are different and are derived from $G-\beta$ locus formulation given by,

$$G = A\sqrt{1 + B\beta}. \tag{2.7}$$

$G-\beta$ locus, in turn, is based on two constants A and B which are changed from 6.75 and 0.75 in XFOIL to 6.75 and 0.83 in RFOIL. These closure sets are changed to yield best approximation at maximum lift [7].

In the wake region, flow is assumed to be turbulent as laminar flow is not feasible beyond trailing edge for wind turbines with high Reynolds number. Therefore, turbulent closure sets are used with zero skin friction. Further the wake is treated as one viscous layer and so only one value of δ^* and θ are defined at each point.

For thick trailing edge airfoils, corrections are implemented in $C_{\tau_{eq}}$as $4{\cdot}C_{\tau_{eq}}$ and C_D as $2{\cdot}C_D$. The $C_{\tau_{eq}}$ is quadrupled to account for the twice larger wake from each of suction and pressure side of the airfoil. The double the thickness of the wake from each side is the result of vigorous mixing in the wake compared to the turbulent boundary layer. However, these changes did not give the desired results due to the dead air region at the immediate vicinity of the blunt trailing edge. A correction is added to the dissipation rate to account for the dead air region [12]. Recently, lift and drag coefficients prediction are improved for thick airfoils [9].

2.3 Viscous-inviscid coupling

The inviscid formulation need to be integrated with viscous part i.e. IBL equations described above for better drag and lift predictions. IBL equations with different closure sets for laminar and turbulent sets are used to solve the viscous segment of the solution. The coupling of IBL equations with inviscid formulation needs to be done properly in leading edge, trailing edge and in the separation region to avoid solution divergence. There are various ways to couple the viscous and inviscid equations. They are direct, inverse, semi-inverse, quasi-simulataneous and fully simultaneous methods [2, 4]. The inviscid and viscous flows are given in terms of velocity at the viscous layer edge U_e as a function of displacement thickness (δ^*).

Inviscid flow: $U_e = f(\delta^*)$
Viscous flow: $U_e = g(\delta^*)$

2.3.1 Direct method

The inviscid part is solved first with the initial guess of δ^* and then the calculated velocity is fed as input for the IBL equations. The δ^* obtained from the viscous equation is used to correct the initial guess for the mass deficiency m. However, this direct method can be used only for attached flows and for small δ^*. Direct method is of the form,

$$\begin{aligned} U_e^n &= f({\delta^*}^{n-1}), \\ {\delta^*}^n &= g^{-1}(U_e^n). \end{aligned} \tag{2.8}$$

where $\delta*^{n-1}$ is assumed initially for the 1^{st} iteration.

2.3.2 Inverse method

This is the inverse method to that discussed above and it is successful for internal flows like compressor with the usage of under relaxation. However, for the external flows the under relaxation need to be increased to obtain required convergence.

$$\begin{aligned} {\delta^*}^n &= f^{-1}(U_e^{n-1}), \\ U_e^n &= g({\delta^*}^n). \end{aligned} \tag{2.9}$$

2.3.3 Semi-inverse method

In order to keep up the stability and speed up the process, semi-inverse technique has been adopted which combines the best of the two methods. For inviscid part, it uses the direct method and for viscous part it uses the inverse formulation. This method has been found to be robust for airfoil flows.

$$
\begin{aligned}
U_{ei}^{n} &= f({\delta^*}^{n-1}), \\
U_{ev}^{n} &= g({\delta^*}^{n-1}), \\
{\delta^*}^{n} &= \lambda(U_{ei}^{n}, U_{ev}^{n}, {\delta^*}^{n-1}).
\end{aligned}
\tag{2.10}
$$

where U_{ei} and U_{ev} are the inviscid and viscous velocity respectively. λ is a relaxation function need to be chosen.

2.3.4 Fully simultaneous method

In this method, the inviscid and viscous formulation are solved together as a single system simultaneously. The viscous model is coupled with the inviscid solution incorporating the mass deficits, which are modelled using source singularity elements. The source singularity elements are distributed on the airfoil surface and the wake. The mass deficit is a function of inviscid velocity and displacement thickness from viscous calculation. The relation between the source singularity elements and the mass deficit is given by,

$$
\sigma = \frac{dm}{dx} = \frac{d(U_{ei}\delta^*)}{dx}, \tag{2.11}
$$

where σ is the source strength singularity element and m is the mass deficit. The fully simultaneous viscous-inviscid coupling is employed in XFOIL and RFOIL. With the vorticity strength (inviscid velocity) from inviscid flow and source strength from viscous formulation to account for the mass deficit, a non-linear coupling can be formulated which is solved by Newton-Raphson method iteratively with quadratic convergence. The formed Jacobian matrix is sparse, which is an advantage when the system is solved using block Gaussian elimination method. The Newton-Raphson solution procedure can be set-up for $F(X) = 0$ as follows.

$$
\begin{aligned}
\delta X^{\nu} &= -\frac{\partial F}{\partial X}^{\nu-1} F(X^{\nu}), \\
X^{\nu+1} &= X^{\nu} + \delta X^{\nu}.
\end{aligned}
\tag{2.12}
$$

where X is a vector of unknowns comprising $C_\tau/\ \bar{n}$, θ, m and a rotational term. $F(X)$ represents the system of equations (2.3), (2.4), (2.5), (2.6) and rotational effects equation ν is the iteration counter. The block representation of the above described system is as follows.

$$\begin{bmatrix} A_1 & C_1 & \dots & \dots & \dots & \dots \\ B_2 & A_2 & C_2 & \dots & \dots & \dots \\ Z_3 & B_3 & A_3 & C_3 & \dots & \dots \\ & \ddots & \ddots & \ddots & \ddots & \\ & & \ddots & \ddots & \ddots & \ddots \\ & & Z_{i-1} & B_{i-1} & A_{i-1} & C_{i-1} \\ & & & Z_i & B_i & A_i \end{bmatrix} \begin{bmatrix} \delta X_1 \\ \delta X_2 \\ \delta X_3 \\ \vdots \\ \vdots \\ \delta X_{i-1} \\ \delta X_i \end{bmatrix} = \begin{bmatrix} R_1 \\ R_2 \\ R_3 \\ \vdots \\ \vdots \\ R_{i-1} \\ R_i \end{bmatrix}, \tag{2.13}$$

Here, each entry in the matrix is a block. R_i represents the negated residual of the system of equations at present station. A_i is derivative of $F(X)$ described above with respect to the unknown vector X at the present station. B_i is derivative of $F(X)$ with respect to the unknown vector X at the previous station. C_i represents the mass block at the present station. It is calculated from the derivative of $F(X)$ combined with the influence matrix d_{ij} calculated from inviscid formulation. d_{ij} can be described by the following equations.

$$\sum_{j=1}^{N+Nw} d_{ij} = \sum_{j=1}^{N+Nw} (\frac{Z}{\gamma})_{ij}^{-1} (\frac{Z}{\sigma})_{ij}, \quad for\, i = 1\, to\, N, \tag{2.14}$$

$$\sum_{j=1}^{N+Nw} d_{ij} = \sum_{j=1}^{N+Nw} (\frac{Z}{\sigma})_{ij}, \quad for\, i = N+1\, to\, Nw. \tag{2.15}$$

where Z represents the influence coefficients, $\frac{Z}{\gamma}$ is the airfoil vorticity contribution and $\frac{Z}{\sigma}$ is the airfoil and wake source contribution. The mass block can be obtained as the derivative of $F(X)$ with respect to the edge velocity (U_e) and δ^* multiplied respectively with the d_{ij} matrix and $\frac{\frac{mass}{U_e}}{U_e} \cdot d_{ij}$. The above mentioned viscous-inviscid formulations can be used for attached and mildly separated flows. For highly separated flows, the wake is no longer thin and this model is no more valid. For conventional sharp trailing edge airfoils, a second wake need to be introduced at the separation point along with the wake from the trailing edge. This is based on the fact that vorticity is continuously released from the separation point. Based on [3] the point of separation need to be given externally. However, it can also be fed from the result of RFOIL/XFOIL simulations at position where the skin friction becomes zero. This highly separated flow is modelled using the vortex panel and integral boundary layer equation either with transition model or lag-entrainment equation, as described in section (2.2), from the stagnation point until the point of separation. At separation point, vorticity needs to be used in such a way to describe the jump in total pressure between the regular flow over airfoil and the reversed flow after separation. Beyond this separation point until trailing edge the flow is treated as purely inviscid. For the unsteady flow, the near wake has to be represented by surface vortices whereas the far wake includes vorticity from previous time step. This model has to be accompanied with integral boundary layer formulation in its unsteady form. However, the lag / transition equation have been used in its steady form [15].

2.4 Previous works on double wake

There are many previous works performed on double wake modelling and mostly involves unsteady implementation. Below some of the key works are summarized.

2.4.1 An inviscid model for unsteady airfoil by Vezza

In the model introduced by Vezza [1], the airfoil surface is divided into N panels with N+1 linear vortex singularity elements. The near wake at separation point and at trailing edge are described by a small panel of length Δ_1, Δ_2 and strength γ_{SEP} and γ_{TE} of constant strengths respectively. The location of the separation is a necessary external input. The far wake is described by discrete point vortices and the formulation is shown in the Figure (2.1).

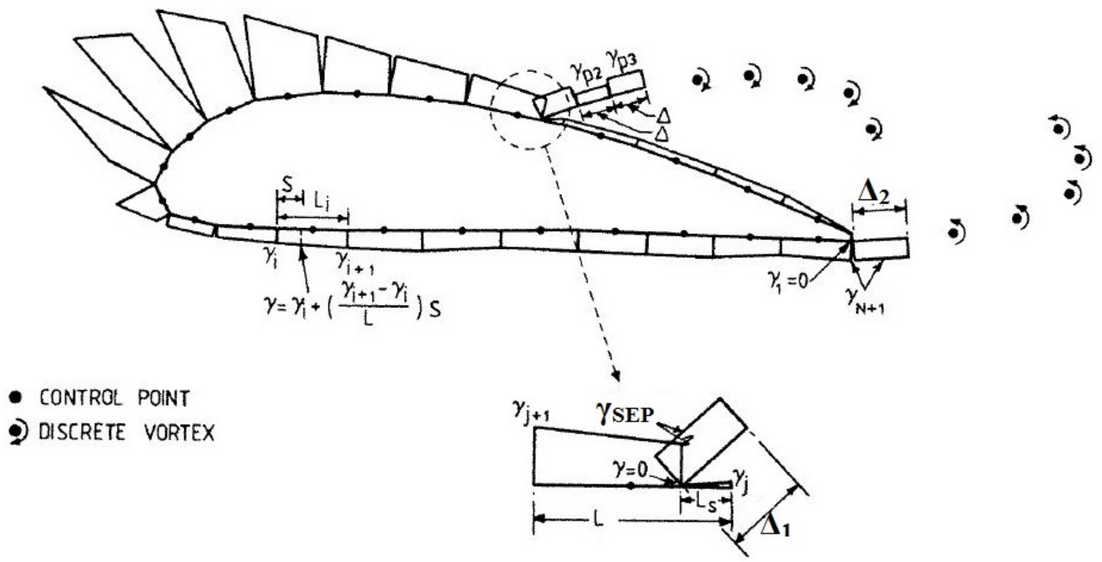

Figure 2.1: Unsteady inviscid formulation by Vezza [1].

The necessary boundary conditions to solve the unknowns are given by Neumann no penetration boundary conditions applied on the chosen collocation points. At the trailing edge, $\gamma_{TE} = \gamma_{N+1}$. As a result of Kutta condition, $\gamma_1 = 0$, γ_{SEP} is given by the equation,

$$\gamma_{SEP} = \gamma_j + (\frac{\gamma_{j+1} - \gamma_j}{L_j})S, \tag{2.16}$$

where, γ_j and γ_{j+1} are the vortex elements adjacent to the separation point, L_j is the length of the panel and S is the distance of the separation point from the position j.

Furthermore, Helmholtz theorem states that vortex strength is constant along a vortex line and Kelvin's theorem states that total circulation within the closed curve is zero. These leads to

$$\gamma_{TE}\ \Delta_2 + \gamma_{SEP}\ \Delta_1 = \Gamma^t - \Gamma^{t-1}. \tag{2.17}$$

From the unsteady Bernoulli's theorem,

$$\frac{{\gamma_{SEP}}^2}{2} - \frac{{\gamma_{TE}}^2}{2} = \frac{\Gamma^t - \Gamma^{t-1}}{\delta t}. \tag{2.18}$$

From the equations (2.17) and (2.18), the relation for the length of the panel at the trailing edge and at separation can be taken as,

$$\Delta_1 = \frac{\gamma_{SEP}}{2}\delta t, \tag{2.19}$$

$$\Delta_2 = \frac{\gamma_{TE}}{2}\delta t. \tag{2.20}$$

The pressure distribution calculation includes total pressure jump as a result of separation. The position of the separation point is considered away from the panel edges as this would avoid the redundancy of the system with one less unknown as described by Vezza [1]. Vezza stated that discrete vortex approximation very close to the panels leads to erroneous results. Therefore, various schemes were adopted to convect the vorticity downstream, namely:

1. $\gamma_{new} = \frac{(\gamma\Delta)_{old}}{\Delta_{new}}$
2. $\Delta_{new} = \frac{(\gamma\Delta)_{old}}{\gamma_{new}}$
3. $\Delta_{new} = \Delta_{old}$, $\gamma_{new} = \gamma_{old}$

The first two methods were found to be unstable by Vezza as large fluctuations influence the entire near wake region. The third method is stable as fluctuations travel only one panel distance at a time. The angle between the first panel and the local tangential velocity is fixed and this serves as an upper limit of inclination for the successive panels in the downstream. The direction of propagation of discrete vortex and total number of vorticity elements are also fixed.

2.4.2 Unsteady viscous inviscid interaction by Ramos-Garcia

The PhD thesis of Nestor Ramos Garcia [2, 16] focusses on the unsteady viscous inviscid interaction scheme with 3D rotational effects. The solution for the unsteady flow problem is modelled by describing singularity element on the surface of the body. The body surface is divided into many panels and a collocation point is defined on each panel. The boundary condition is applied on each panel in the collocation point. For inviscid flows, no penetration boundary condition is used either as a Dirichlet or Neumann boundary condition. For unsteady flows the total circulation is now dependent on time. Based on Helmholtz theorem, the vortex needs to shed from airfoil surface and becomes a part of the wake. Both single wake and double wake model has been implemented.

1. **Single wake:** The airfoil surface is formed using constant source singularity elements and each panel edge are made of linear vortices. The wake is modelled by the point vortices. The vortex is shed from the trailing edge for every time step. Single wake model does not perform well at highly stalled region and so double wake method has been formulated.

2. **Double wake:** In the double wake model only potential flow is considered in the separated region. This is due to the fact that the vorticity is directly proportional to the amount of shear. In the separated region, there is minimum shear and so vorticity and associated losses are minimum. Therefore, the total pressure remains constant in the separated region and so the above assumption is valid. Predicting the pressure in the separated region and the exact position of separation is the major challenge. The double wake is modelled with vorticities in the form of one wake panel followed by discrete vortex blobs released from trailing edge and from the separation point. The vorticities are in opposite direction and so the region of flow reversal in the separated region can be modelled. The length of the wake is determined based on cut off level from the number of vortex blobs shed. The higher the frequency the larger the pressure difference between the collocation points and the solution convergence depends on the frequency of airfoil movement.

   In this model a pressure correction term is introduced to account for the total pressure jump between the separated region and the other region surrounding the airfoil. The separation position can be found using IBL equations however the problem is that the separation point does not move in time as in the experimental data. The formulation is shown in the Figure (2.2).

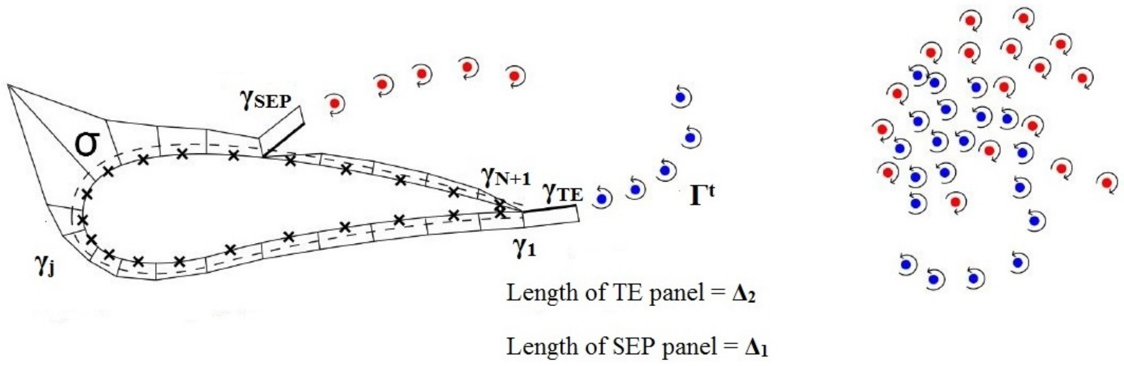

Figure 2.2: Unsteady viscous-inviscid formulation by Ramos-Garcia [2].

The airfoil is divided into N panels with constant source element of known strength over the airfoil surface and linear $N+1$ vortex elements. The vorticity is released at the trailing edge and separation point as γ_{TE} and γ_{SEP} respectively of one panel length. In order to solve the $N+4$ unknowns totally, $N+4$ boundary conditions are required. Neumann no penetration boundary condition is applied at N collocation points defined in N panels. Furthermore, $\gamma_{TE} = \gamma_1$ and $\gamma_{N+1} = 0$. As a result of Kutta condition (i.e. the total circulation must be constant), the γ_{SEP} = -γ_{TE}. The last boundary condition is by Kelvin's theorem and given by the equation (2.21).

$$\gamma_{TE}\ \Delta_2 + \gamma_{SEP}\ \Delta_1 = \Gamma^t - \Gamma^{t-1}. \tag{2.21}$$

The length and inclination of the near wake panels are an assumption to start the calculation. The viscous effects are modelled using IBL equations. Once the system is modelled, the length of the near wake and the inclination angles are updated. The formulations of the near wake panel and the inclination is given by the following equations.

$$\Delta_2 = \frac{\gamma_{TE}}{2}, \tag{2.22}$$

$$\Delta_1 = \frac{\gamma_{SEP}}{2}, \tag{2.23}$$

$$\begin{aligned} \theta_{TE} &= \alpha_1 \quad \gamma_{TE} < 0, \\ &= \alpha_{N+1} \quad \gamma_{TE} > 0, \end{aligned} \tag{2.24}$$

$$\theta_{SEP} = tan^{-1}(v_{SEP}/u_{SEP}), \tag{2.25}$$

where, α_1 is the angle of 1^{st} panel α_{N+1} is the angle of the last panel with respect to global coordinates. The convergence threshold is kept to be 10^{-4}.

2.4.3 Dynamic stall modelling on airfoils by Riziotis

This model [3] includes N constant source singularity element along the airfoil surface divided into N panels and two uniform vortex distribution γ_1 and γ_2, one from trailing edge until point of separation which is of length L_1 along the airfoil surface and the other from point of separation until trailing edge of length L_2 considered along the same direction. The Figure (2.3) shows the formulation with both single and double wake for attached and separated flow respectively.

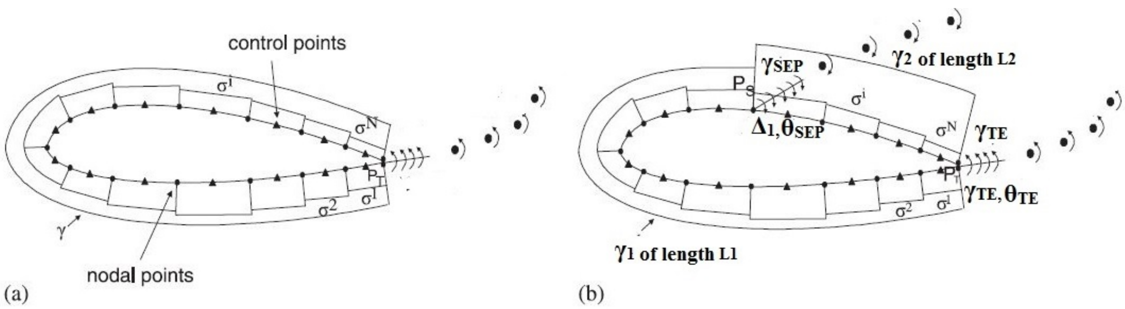

Figure 2.3: Unsteady formulation by Riziotis [3].

In order to solve the system of equations, Neumann no penetration boundary condition is applied at N collocation points. The two near wakes released are given by γ_{TE} and γ_{SEP} which are defined by the equation as follows:

$$\begin{aligned} \gamma_{TE} &= u_u - u_l, \\ \gamma_{SEP} &= u_u, \end{aligned} \tag{2.26}$$

where, u_u and u_l are the local tangential velocity before and after the wake panel respectively. The final boundary condition is given by the total circulation as,

$$\Gamma = \gamma_1 L_1 + \gamma_2 L_2. \tag{2.27}$$

Initially the length of the near wake both at separation point and at trailing edge are based on assumption. The inclination of the wake panels at the trailing edge are aligned either parallel to the lower or upper surface of the airfoil depending on the sign of the circulation. At the separation point the inclination is taken to be the average of the velocity at the neighbouring panels. After the initial iteration the length of the near wake are calculated as described in the following equation,

$$\begin{aligned} \Delta_1 &= \frac{u_u}{2}\delta t, \\ \Delta_2 &= \frac{u_u + u_l}{2}\delta t. \end{aligned} \tag{2.28}$$

2.4.4 Vortex panel method for vertical axis wind turbine by Zanon

The model [4] has been described for both attached and separated flows and is an adoptation from Riziotis with some changes in it.

1. **Attached flow:** In the attached flow, the surface of airfoil is described by N panels each described by source singularity and a constant vorticity over the entire airfoil. As the wake is unsteady the far wake is described by point vortices. The near wake is described by a panel extended from trailing edge of the airfoil for a length of Δ_2 and strength of γ_{TE}. The inclination of the panel is not parallel to upper or lower surface as described by Basu and Riziotis [3]. The inclination is defined by the vector sum of the adjacent panels at the trailing edge.

2. **Separated flow:** The above formulation is followed for the separated flow also. In addition to these, a second wake is being released from the separation point with separation point fed externally. The near wake at separation panel is modelled by a single wake of length Δ_1 and strength γ_{SEP}. The strength of the near wake both at separation and trailing edge is the same as given by Riziotis in section (2.4.3). The far wake is given by a point vortices. The wake described for attached flows at the trailing edge is modified with its inclination parallel to the pressure side for separated flows (double wake) rather than along the vector sum of edge panels as in attached flow. This measure has been taken into account to mimic the real flow scenario.

   The near wake panel length at the trailing edge is given by the equation

   $$\Delta_2 = \frac{u_u + u_l}{2}\delta t. \tag{2.29}$$

   The general assumption in all the work is based on that of Riziotis, that the tangential velocity right after the separation point is taken to be zero. Hence, the length of the near wake at separation is given by the equation,

   $$\Delta_1 = \frac{u_u}{2}\delta t. \tag{2.30}$$

   This formulation is the same as used by Riziotis and is shown in the Figure (2.4).

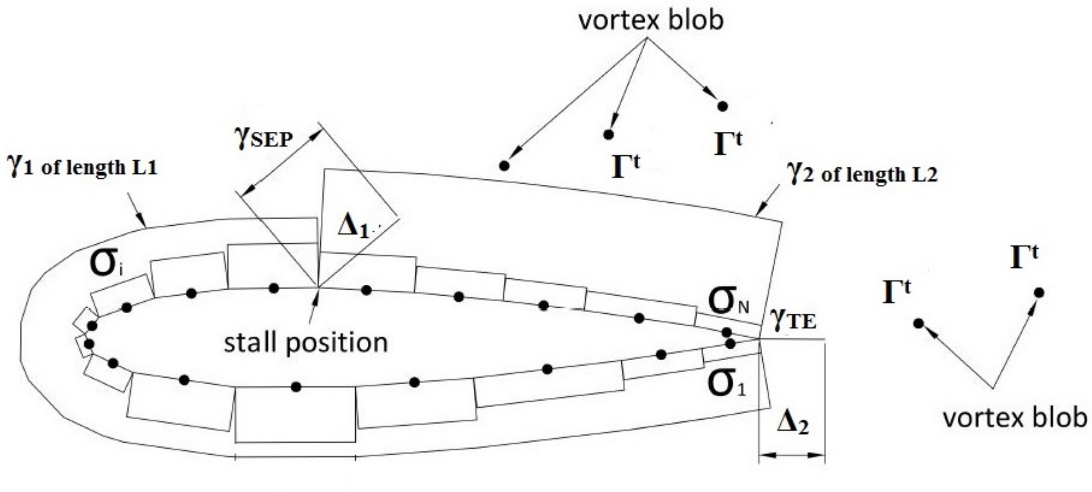

Figure 2.4: Unsteady formulation by Zanon [4].

For both attached and separated flows, Kutta condition for unsteady flow is not unique. For steady state there is no vortex shedding ($\Gamma = 0$) and pressure on both sides of the wake is equal. However, for unsteady flows, Kutta condition can be either equal velocities or equal pressure (i.e. zero loading). As zero loading is physically feasible solution, this has been taken into account [17]. Further in the C_p calculation, for the separated flows, there is a jump in total pressure between the region enclosed between the two wakes and the outer region which needs to be taken into account. Further as described in [2], the boundary layer is neglected in the region between the wakes. The viscous and inviscid flows are solved together by means of semi-inverse method.

Riziotis and Zanon both modelled unsteady separation with time updated point vortices. However, different approaches are used to model the orientation of first released near wake panel.

2.4.5 Inviscid steady double wake model by Marion

In this model [5] the external flow over the airfoil is separated as two regions of inviscid flow. The arifoil surface is divided into N panels numbered in clockwise direction, with $N+1$ linear vortex singularity elements. Further, two separation wake sheets of γ_{TE} and γ_{SEP} respectively at the trailing edge and at separation point are modelled. The model is described by the Figure (2.5). To solve the $N+3$ unknowns totally, $N+3$ boundary conditions are required. Neumann no penetration boundary condition is implemented at N collocation points defined in N panels.

Furthermore, $\gamma_{TE} = \gamma_1$ and $\gamma_{N+1} = 0$. As a result of Kutta condition (i.e. the total circulation must be constant), the γ_{SEP} = -γ_{TE}.

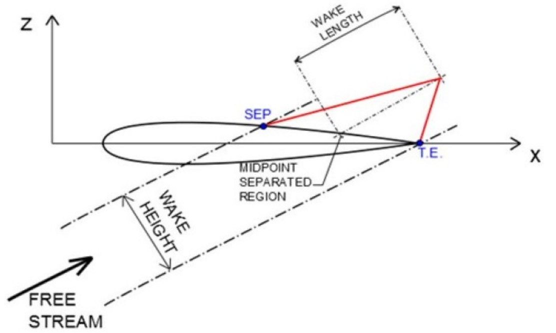

Airfoil and initial wake geometry.

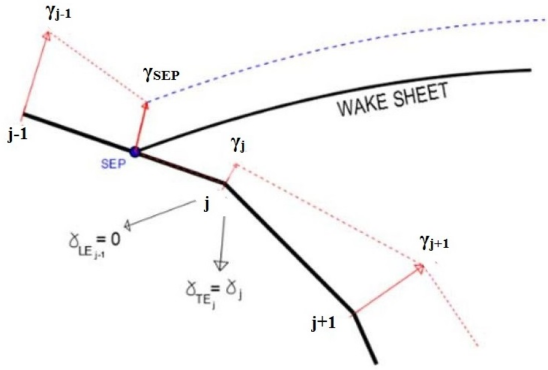

Figure 2.5: Inviscid steady double wake by Marion [5].

Furthermore, in the C_p calculation total pressure jump of Δh i.e. the difference between the head on both sides of the wake, needs to be taken into account in the separated region. This Δh is zero in other regions. From the steady Bernoulli's equation,

$$\Delta h = \frac{{u_u}^2 + {u_l}^2}{2}. \tag{2.31}$$

Also it is known that the

$$\gamma_{SEP} = u_u - u_l. \tag{2.32}$$

From the Riziotis assumption the tangential velocity just after separation is given by the equation (2.33),

$$u_l = 0. \tag{2.33}$$

The jump in total pressure between the separated and non-separated flow is given by,

$$\Delta h = h^-_{SEP} - h^+_{SEP}. \tag{2.34}$$

From the equations (2.31) to (2.34) the jump is,

$$\Delta h = -\frac{\gamma^2_{SEP}}{2}. \tag{2.35}$$

The length of the wake sheets from the separation point and the trailing edge, as described in the Figure (2.5), is given by $W_l = W_h \cdot W_f$, where W_h and W_l are wake height and wake length respectively. The W_f is the wake factor given by cubic trend law found from experimental value using 6 airfoils and tested for 2 other airfoils. $W_f = 9.8 * 10^{-4}(\alpha) - 7.5 * 10^{-2}(\alpha) + 2.9$. The separation point for this model needs to be given externally.

2.5 Summary of previous works and present approach

Several authors in literature provided different approaches for the double wake modeling. Vezza et al. [1] modelled an unsteady, incompressible separated flow. $N+1$ linear vortices are considered on N airfoil panels; for the near wake, a panel at separation point and one at the trailing edge are included; for the far wake, discrete vortices model the asymptotically steady separated flow. The algorithm is developed with fixed separation point as an external input. For moving airfoils, Riziotis et al. [15, 3] modeled unsteady double wake, accounting for dynamic effects, with N sources and two distributed vortices representing attached and separated regions with strong interation of unsteady boundary layer. The model predicts accurately the separation location up to moderate stall. Zanon [4] adopted Riziotis model for vertical axis wind turbines with modifications in the orientation of near wake panel. Ramos Garcia [2] modeled unsteady 2D flow with linear vortices and a source. The separation point is calculated externally from the strong viscous-inviscid coupling procedure. The model yields a good agreement for the predicted aerodynamic lift against experiments at low AoA, while lift is over predicted at high AoA. Steady double wake for separated flows are modeled by Dvorak et al. [18] and Marion et al. [5] with the length of the wake sheets determined by wake factor and wake height. Dvorak determines the initial wake shape with a parabolic curve whereas Marion considers an experimental wake factor. These models show good agreement with experiment with some discrepancies in deep stall region. The present successful implementation shown in section (4.2) is steady double wake model which would be later integrated into existing steady aerodynamic design tool RFOIL. Unlike previous works, the initial wake shapes do not intersect downstream and are determined by the induced velocity from the vorticity distribution. This makes this approach independent of external parameter like wake factor.

Chapter 3

Inviscid flow modelling

The lift and moment coefficients of an airfoil mainly depends on the pressure distribution over the airfoil. The pressure coefficient from inviscid calculation is independent of the freestream velocity and dependent only on the shape geometry of the body and AoA under consideration. The inviscid flow over airfoils is a potential flow and can be described using Laplace equation. The continuous mathematical equation is given by,

$$\nabla^2 \phi = 0 \tag{3.1}$$

where ϕ represents the velocity potential. Laplace equation is a second order linear partial differential equation and so the principle of superposition can be applied. As a result, the total solution to the flow described by the equation (3.1) can be represented as sum of the solutions of the individual elementary flows. This property of the Laplace equation helps in modelling the potential flow using various singularity element over airfoil surface. Using the singularity elements like *source*(σ), *doublet* (μ) or *vorticity* (γ) on the body surface of the airfoil, elementary flow solutions can be modelled. The source singularity elements are associated with zero circulation and vortex/doublet singularity elements has circulation associated with them and so contribute to the lift. The relation between vortex and doublet element is given as follows.

$$\gamma(x) = -\frac{d\mu(x)}{dx}, \tag{3.2}$$

where γ is the vortex singularity element and μ represents the doublet singularity element. Hence in order to define the aerodynamic properties of the inviscid flow, usage of vortex element is a reasonable choice than doublet as the former has the same results for one order smaller equations than the latter. The fluid flow with circular streamlines is considered as vortex flow. For the point vortex singularity element in 2D, the velocity is constant along the streamlines and varies inversely with distance from one streamline to another. The name singularity element for the vortex flow is the result of the velocity being singular at the origin. The velocity potential and the velocity in the tangential and normal direction is given by the following equation,

$$\begin{aligned}\phi &= -\frac{\Gamma}{2\pi}\theta,\\ u &= \frac{\partial\phi}{\partial x},\\ v &= \frac{\partial\phi}{\partial y},\end{aligned} \tag{3.3}$$

where ϕ represents the velocity potential, u and v represent the velocity in $x-$ and $y-$ directions respectively.

The surface of the airfoil is modelled using flat panels, each with the strength of linear vortex singularity element. This usage of linear element is justified in section (2.1). The velocity potential and the velocity in the tangential and normal direction as a result of the linear vortex singularity element can be calculated from Biot-Savart law. Biot-Savart law is one of the fundamental laws of inviscid, incompressible flows. It is analogous to the electromagnetic theory and it states that any filament of source or vortex strength can induce a flow field surrounding it. The influences of the linear vortex element at a point (x,y) are obtained by integrating the influences of the point elements on a panel of length x_1 and x_2. The associated integrals as given by Katz and Plotkin [6] are,

$$\begin{aligned}\phi &= -\frac{\gamma_c}{2\pi}\int_{x_1}^{x_2}\tan^{-1}\frac{y}{x-x_0}dx_0 - \frac{\gamma_l}{2\pi}\int_{x_1}^{x_2}x_0\tan^{-1}\frac{y}{x-x_0}dx_0,\\ u &= \frac{\gamma_c}{2\pi}\int_{x_1}^{x_2}\frac{y}{(x-x_0)^2+y^2}dx_0 + \frac{\gamma_l}{2\pi}\int_{x_1}^{x_2}x_0\frac{y}{(x-x_0)^2+y^2}dx_0,\\ v &= -\frac{\gamma_c}{2\pi}\int_{x_1}^{x_2}\frac{x-x_0}{(x-x_0)^2+y^2}dx_0 - \frac{\gamma_l}{2\pi}\int_{x_1}^{x_2}x_0\frac{x-x_0}{(x-x_0)^2+y^2}dx_0.\end{aligned} \tag{3.4}$$

Vortex strengths in the above equations γ_c and γ_l are given by,

$$\begin{aligned}\gamma_j &= \gamma_c,\\ \gamma_{j+1} &= \gamma_c + \gamma_l\ a,\end{aligned} \tag{3.5}$$

where, γ_j and γ_{j+1} are the vortex strength at the panel end point and a is the length of the panel. The decomposition of the linear vortex element on a panel is shown in the Figure (3.1).

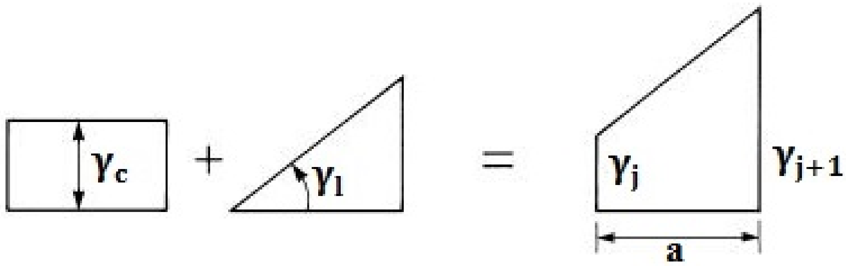

Figure 3.1: Decomposition of linear vortex element over a panel [6].

The above integrals are evaluated to compute the induced velocities as a result of the linear vortex distribution on each of the panels. The total velocity from linear vorticity in an inviscid, incompressible, irrotational flow (i.e. potential flow) field can be described as,

$$\vec{U} = \vec{U_0} + \vec{U_\gamma}, \tag{3.6}$$

where $\vec{U_\gamma}$ is the velocity induced as a result of linear vortex singularity elements. The airfoil is impermeable to the flow. This property is utilized to obtain the unknown singularity distribution over the airfoil by Neumann boundary condition as given by,

$$\vec{U_0}.n_i + \vec{U_\gamma}.n_i = 0, \tag{3.7}$$

where n_i is the unit normal to the i^{th} panel representing airfoil surface. Kutta-Joukowski theorem states that the aerodynamic lift in an incompressible, inviscid flow for the airfoil in an unbounded fluid i.e. without any additional boundary conditions from external influences, acts perpendicular to the freestream and is given as,

$$L = \rho\, U_0\, \Gamma. \tag{3.8}$$

The fluid flow around the airfoil is the superposition of translational and rotating flow. The rotational flow is generated as a result of airfoil camber, angle of attack and not due to rotation of airfoil. The inviscid solution as a result of linear vortices is not unique as this is mainly dependent on the chosen circulation. Therefore, Kutta framed a physical considerations to determine the amount of circulation around the airfoil surface. The condition states that for a steady potential flow, the velocity where the flow leaves the airfoil need to be equal from both suction and pressure side of the airfoil, for flow to leave the airfoil smoothly. Further, Helmholtz theorem states that vorticity cannot start or end in the fluid. It has to shed in the flow as wake. The implementation of inviscid flow requires all the above conditions to be satisfied.

3.1 Inviscid single wake model

The airfoil surface is divided into N panels. In order to account for the aerodynamics properties, each of the panels could be represented with a point, constant, linearly varying, quadratic varying strength singularity elements. The point elements are inefficient near stagnation point of thick airfoils. The constant elements calculate pressure distribution accurately but result in singularity in panel edges and so linearly varying strength vortex elements are a better choice to model the airfoil surface. Any higher order elements can be used to increase the accuracy but involve difficulty in implementation. The source elements will be later integrated while considering viscous flows.

To model inviscid flow with single wake, linear vortex elements are chosen for N panels. The strength of the linear elements are defined at the panel edges and so there are $N + 1$ unknowns. The panel orientation is made to be in anticlockwise direction as this is the convention followed in RFOIL and would be helpful to integrate the method at a later time. The vorticity distribution for single wake formulation is shown in the Figure (3.2).

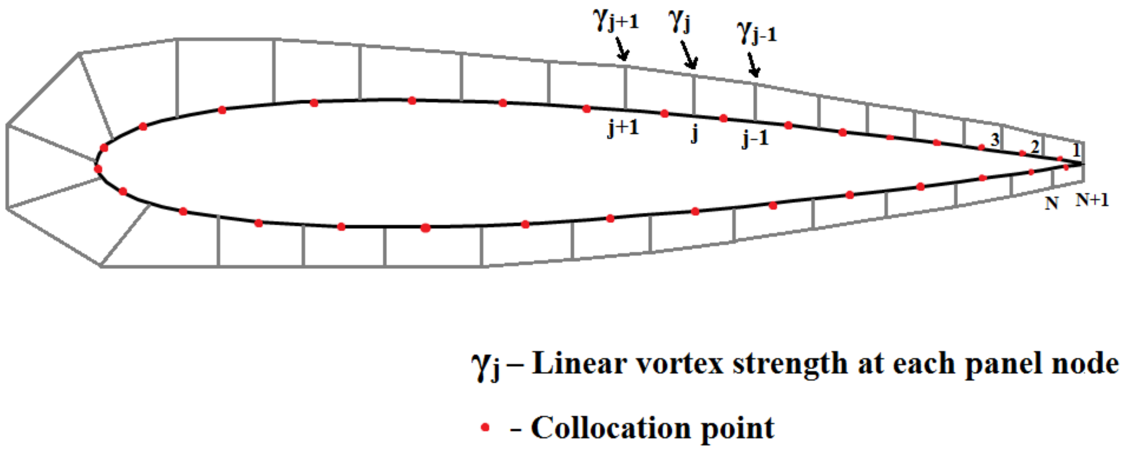

Figure 3.2: A sketch of linear vortex strength distribution on airfoil surface for single wake formulation.

The singularity elements are calculated by means of $N + 1$ boundary conditions. Neumann no penetration boundary conditions are imposed on N collocation points and Kutta condition is expressed as $N + 1^{th}$ boundary condition. The collocation points are chosen to be the midpoint of each panel. At each collocation point, the induced velocity is calculated from the influence of all the vortex singularity elements placed on all the panel on airfoil surface. Initially, the chosen collocation points and the end points of each panels are transformed from global coordinates to panel coordinates by,

$$\begin{bmatrix} x \\ y \end{bmatrix} = \begin{bmatrix} -cos\,\alpha_j & -\,sin\,\alpha_j \\ -sin\,\alpha_j & cos\,\alpha_j \end{bmatrix} \begin{bmatrix} X \\ Y \end{bmatrix}, \tag{3.9}$$

where, α_j represents the panel inclination with respect to the global coordinates.

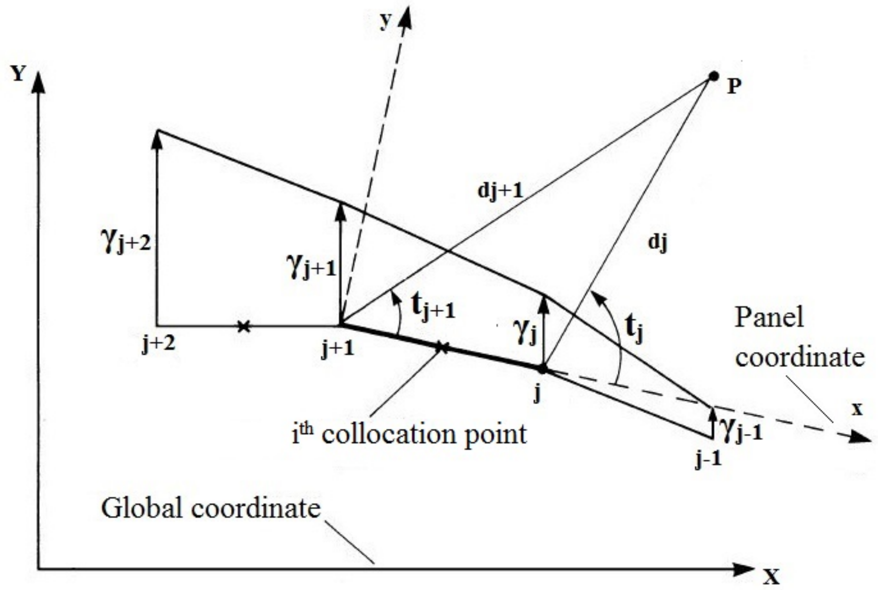

Figure 3.3: A sketch of linear vortex strength singularity element and the entities.

Figure (3.3) shows the linear vorticity distribution with the geometrical entities. The point P is used only for representation. For the calculation, the point P and the corresponding entities are considered as that of collocation point. The induced velocities as a result of linear vortex element is calculated in the panel coordinates as given by Katz and Plotkin [6] and is given by the following equation set.

$$\begin{aligned} U_1 &= -\frac{c_y\,log\frac{d_2}{d_1} + a_x(t_2 - t_1) - b_x(t_2 - t_1)}{2b_x\pi}, \\ U_2 &= \frac{c_y\,log\frac{d_2}{d_1} + a_x(t_2 - t_1)}{2b_x\pi}, \\ W_1 &= -\frac{b_x - c_y\,(t_2 - t_1) - a_x\,log\frac{d_1}{d_2} + b_x\,log\frac{d_1}{d_2}}{2b_x\pi}, \\ W_2 &= \frac{b_x - c_y\,(t_2 - t_1) - a_x\,log\frac{d_1}{d_2}}{2b_x\pi}, \end{aligned} \tag{3.10}$$

where, a_x and b_x are the distances along x axis between the collocation point and the end points of each panel. c_y is the distance along y axis between the collocation point and the end points of each panel. d_1 and d_2 represent the distance between the collocation point and the end points of each panel. t_1 and t_2 are the angles corresponding to d_1 and d_2 respectively. All the variables described are in panel coordinates. Hence, the calculated induced velocities are transformed back to the global coordinates by,

$$\begin{bmatrix} X \\ Y \end{bmatrix} = \begin{bmatrix} -cos\,\alpha_j & -\,sin\,\alpha_j \\ -sin\,\alpha_j & cos\,\alpha_j \end{bmatrix} \begin{bmatrix} x \\ y \end{bmatrix}, \tag{3.11}$$

$$\begin{aligned} U_{al} &= -U_1\,cos(\alpha_j) - W_1\,sin(\alpha_j), \\ U_{bl} &= -U_2\,cos(\alpha_j) - W_2\,sin(\alpha_j), \\ W_{al} &= -U_1\,sin(\alpha_j) + W_1\,cos(\alpha_j), \\ W_{bl} &= -U_2\,sin(\alpha_j) + W_2\,cos(\alpha_j). \end{aligned} \tag{3.12}$$

The calculated induced velocities U_{al}, U_{bl}, W_{al} and W_{bl} in global coordinates as a result of all the linear vortex elements placed at the panel end points contribute to the aerodynamic influence coefficients. The total induced velocities at each intersection point of two panels, except for the first and last panel edge, are taken to be the sum of the velocities induced as a result of these neighbouring panels at the intersection. This is represented by,

$$u_{i,j}, w_{i,j} = (U_{al}, W_{al})_{i,j} + (U_{bl}, W_{bl})_{i,j-1}, \tag{3.13}$$

where, i is the collocation point and j represents panel end points. The total induced velocity in the first and the last panel edge is given by,

$$\begin{aligned} u_{i,1}, w_{i,1} &= (U_{al}, W_{al})_{i,1}, \\ u_{i,N+1}, w_{i,N+1} &= (U_{bl}, W_{bl})_{i,N}. \end{aligned} \tag{3.14}$$

The following equation shows the normal component of the induced velocities that is used to calculate the vorticity distribution over airfoil surface with the Neumann boundary condition:

$$A_{i,j} = u_{i,j}.n_i, \tag{3.15}$$

n_i corresponds to normal vector at each collocation point. The Neumann no penetration boundary condition leads to,

$$A_{i,j}\,\gamma_j + (\vec{U}_0.n_i) = 0. \tag{3.16}$$

This leads to N boundary conditions as there are N collocation points. The $N+1^{th}$ boundary condition is the Kutta condition and is taken to be $\gamma_1 + \gamma_{N+1} = 0$. The Kutta condition is a neccessary boundary condition as this imposes that the pressure of the fluid leaving the suction and pressure side of the trailing edge are equal and thus making the fluid flow to be physical. Also, Kutta boundary condition leads to an unique solution of the flow conditions. With the $N+1$ boundary conditions, the influence coefficient matrix $A_{i,j}$ is given by,

$$A_{i,j} = \begin{bmatrix} u_{1,1} & u_{1,2} & u_{1,3} & \dots & u_{1,N+1} \\ u_{2,1} & u_{2,2} & u_{2,3} & \dots & u_{2,N+1} \\ \vdots & \vdots & \vdots & \ddots & \vdots \\ u_{N,1} & u_{N,2} & u_{N,3} & \dots & u_{N,N+1} \\ 1 & 0 & 0 & \dots & 1 \end{bmatrix}, \tag{3.17}$$

With the coefficient matrix $A_{i,j}$ and Kutta condition, the vortex singularity elements at each panel edge are calculated using the below equation:

$$\gamma_j = -A_{i,j}^{-1}\,(\vec{U}_0.n_i). \tag{3.18}$$

3.1.1 Pressure coefficient

Once the vorticity distribution over airfoil surface is calculated, the pressure coefficient (C_p) at each collocation point is obtained from the sum of the tangential component of the induced velocity at the collocation point along with the the tangential component of the freestream velocity. The induced tangential velocity component is calculated at each of the collocation points from the influence of all the vorticities on airfoil surface. The C_p is calculated as follows.

$$C_p = 1 - \frac{q^2}{U_0^2}, \tag{3.19}$$

where, q is the total tangential velocity as the result of freestream tangential component and the induced tangential component. Two airfoils namely Van de Vooren (VDV) and NACA0012 are tested with the single wake inviscid model. Figures (3.4) and (3.5) show C_p plot of symmetric airfoil VDV of 12% thickness at AoA of 6° and 21° respectively. Similarly, Figures (3.6) and (3.7) show C_p plot of another symmetric airfoil NACA0012 of 12% thickness at AoA of 6° and 20° respectively. The calculated C_p with single wake inviscid model are compared with respect to XFOIL and RFOIL inviscid cases. These inviscid cases are independent of the Reynolds number and depends only on AoA. The result is found to be accurate along the airfoil surface except along the peak suction pressure and trailing edge region. The 2D inviscid single wake model predicts less suction pressure in both the cases as compared with XFOIL and RFOIL. These mismatchings are addressed in section (3.2).

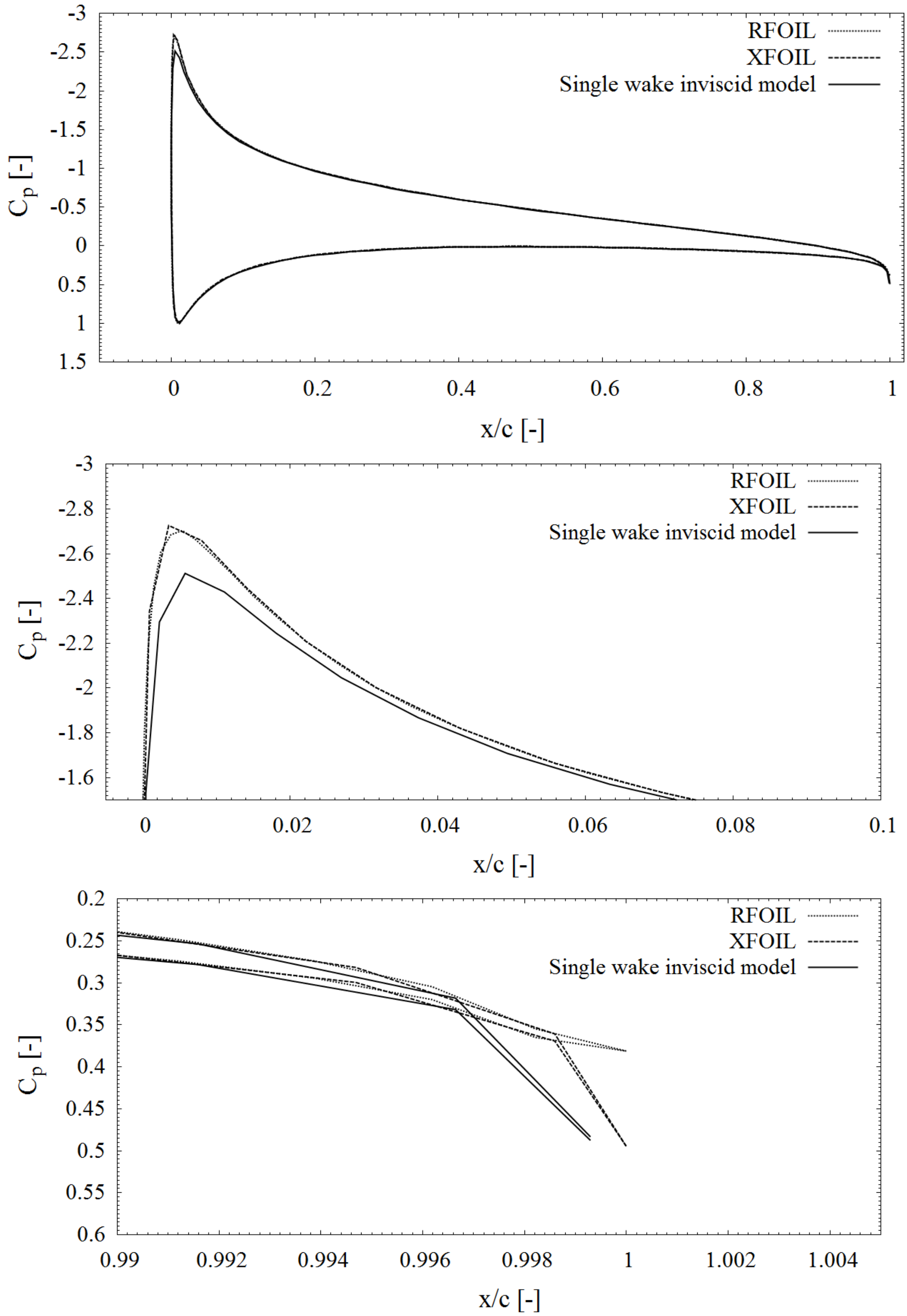

Figure 3.4: Comparison of pressure coefficients, at AoA of 6° for VDV airfoil using 200 panels (top), a zoom in to pressure peak at the leading edge suction side (middle) and to the trailing edge (bottom).

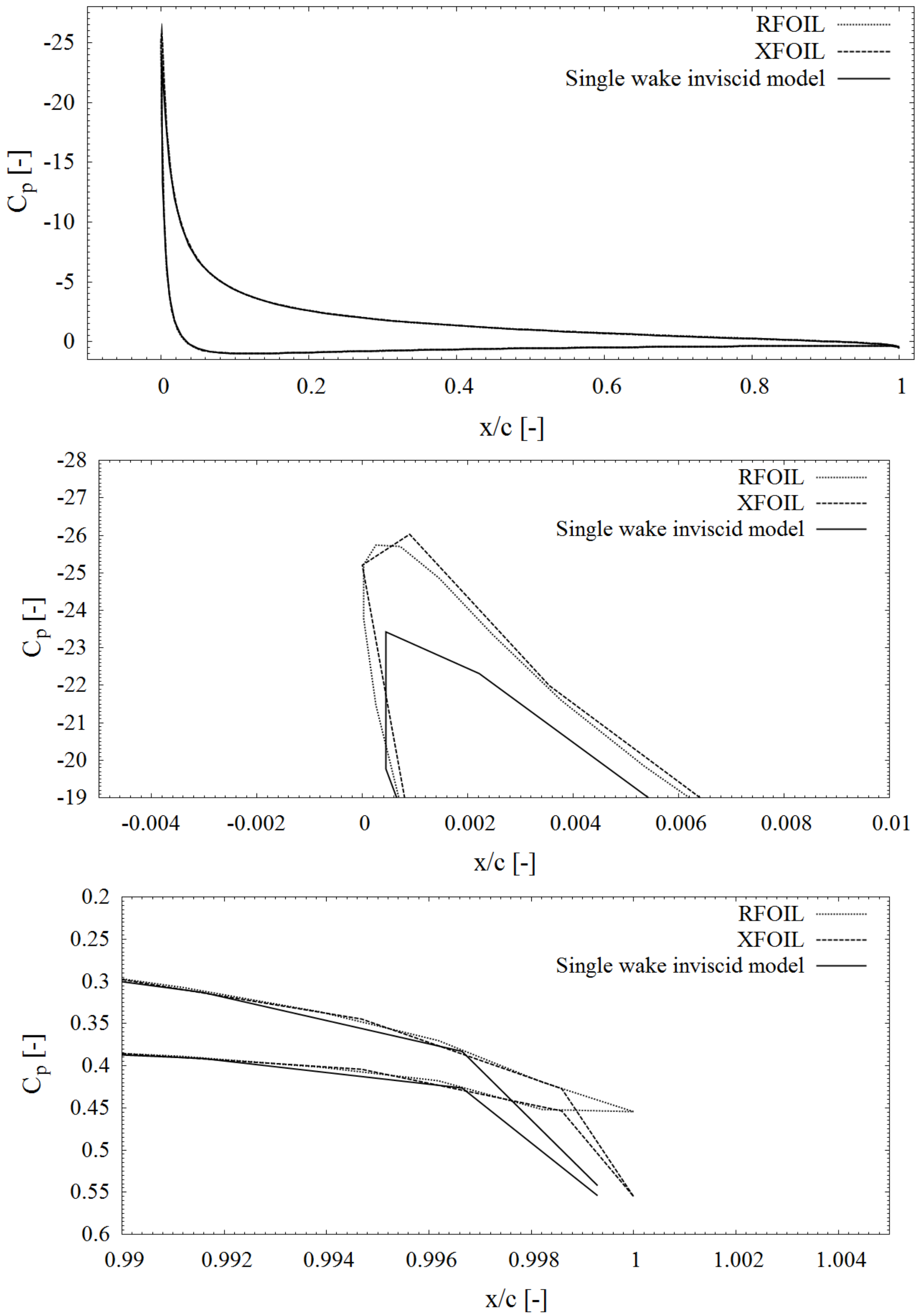

Figure 3.5: Comparison of pressure coefficients, at AoA of 21° for VDV airfoil using 200 panels (top), a zoom in to pressure peak at the leading edge suction side (middle) and to the trailing edge (bottom).

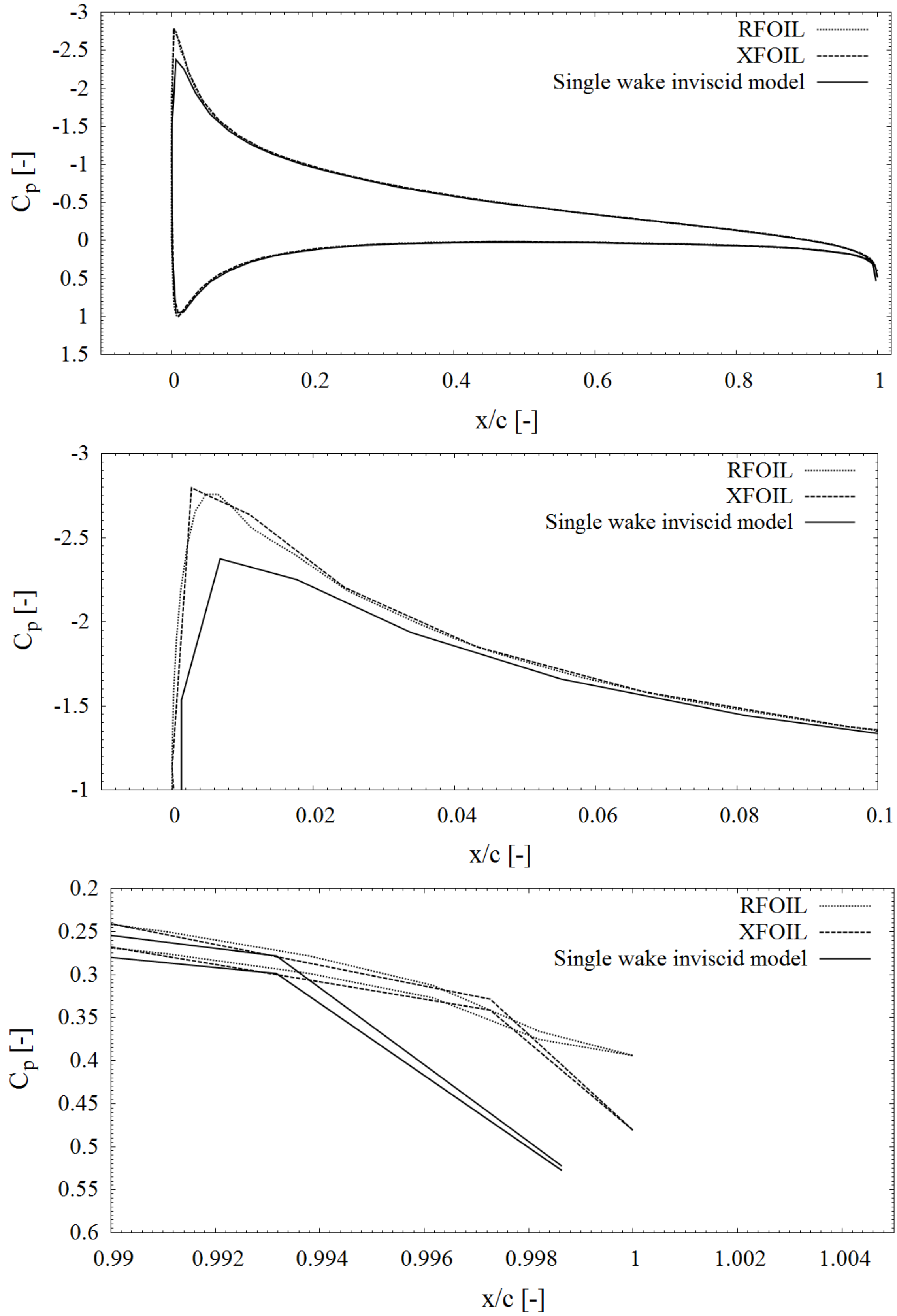

Figure 3.6: Comparison of pressure coefficients, at AoA of 6° for NACA0012 airfoil using 200 panels (top), a zoom in to pressure peak at the leading edge suction side (middle) and to the trailing edge (bottom).

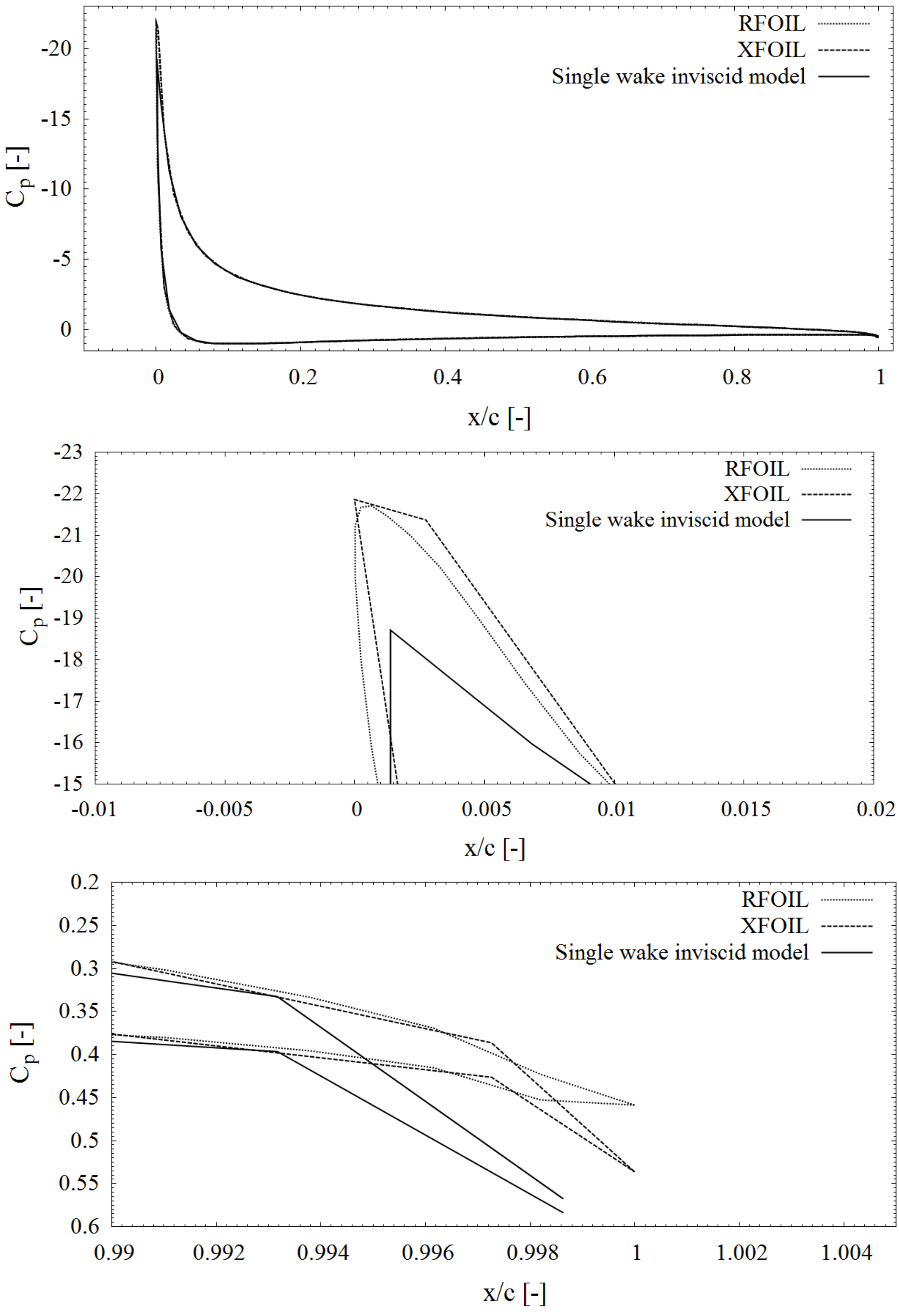

Figure 3.7: Comparison of pressure coefficients, at AoA of 20° for NACA0012 airfoil using 200 panels (top), a zoom in to pressure peak at the leading edge suction side (middle) and to the trailing edge (bottom).

3.2 Optimal number of airfoil panels

In the previous section, there were discrepencies in the obtained result in comparison to that of XFOIL at the peak suction region and at the trailing edge. In order to get an accurate result, the panels over the airfoil need to be optimized. This is done by curve fitting followed by clustering of points near the peak suction region and trailing edge. The clustering of points facilitates the accurate C_p calculation at the high curvature leading edge and sharp trailing edge.

3.2.1 Curve fitting

Curve fitting is the process of formulating a curve with a mathematical function in such a way that it fits all the given data points. This can be done by either polynomial or spline curve fitting.

Polynomial curve fitting or Lagrange interpolation uses higher degree polynomial and the curve is smoother compared to linear interpolation. However, it has the disadvantage of overfitting within the given points. It does not capture the needed shape or curvature. Any change in one of the data points influences the entire shapes of the curve. Hence this method is non-local.

Natural Spline interpolation which is local method, utilising many pieces of polynomial to interpolate and hence there is no disturbance to the curve shape due to change in any data points. Spline interpolation can be of linear or cubic. The most commonly used technique is cubic spline interpolation due to accurate mapping and the same is utilised here.

For $N+1$ set of given data points, N splines are defined with cubic polynomials and so 4 unknowns arises for each polynomial leading to $4 \cdot N$ coefficients in total. The cubic spline interpolation is also given the condition that the first and second derivatives exist and remain continuous between splines.
The y_{new} based on chosen x_{new} can be obtained from,

$$\begin{aligned} y_{i_{new}} &= (1-t)y_j + (t)y_{j+1} + t(1-t)[(aa_j)(1-t) - (bb_j)(t)], \\ t &= \frac{x_{i_{new}} - x_j}{x_{j+1} - x_j}, \end{aligned} \tag{3.20}$$

where j corresponds to the given data points and i to the newly calculated data points. aa_j and bb_j in the above equation (3.20) is the first derivative of y obtained as a result of continuous curve, i.e. $aa_j \quad or \quad bb_j = y'_j = y'_{j+1}$. From the above condition the system of equations to calculate aa and bb is given by,

$$\begin{aligned} aa_j &= k_{j-1}(x_j - x_{j-1}) - (y_j - y_{j-1}), \\ bb_j &= k_j(x_j - x_{j-1}) - (y_j - y_{j-1}). \end{aligned} \tag{3.21}$$

The unknown k_j is calculated from the so formed tri diagonal system as,

$$\begin{aligned} \frac{k_{j-1}}{x_k - x_{k-1}} + 2k_j(\frac{1}{x_k - x_{k-1}} + \frac{1}{x_{k+1} - x_k}) + \frac{k_{j+1}}{x_{k+1} - x_k} = \\ 3\frac{y_k - y_{k-1}}{(x_k - x_{k-1})^2} + 3\frac{y_{k+1} - y_k}{(x_{k+1} - x_k)^2}. \end{aligned} \tag{3.22}$$

The coressponding coefficient for the tri diagonal matrix is given by the following equation:

$$\begin{aligned} a_k &= \frac{1}{x_k - x_{k-1}}, \\ b_k &= 2(\frac{1}{x_k - x_{k-1}} + \frac{1}{x_{k+1} - x_k}), \\ c_k &= \frac{1}{x_{k+1} - x_k}, \\ d_k &= 3\frac{y_k - y_{k-1}}{(x_k - x_{k-1})^2} + 3\frac{y_{k+1} - y_k}{(x_{k+1} - x_k)^2)}, \end{aligned} \tag{3.23}$$

where, k ranges from 1 to N panels. The coefficients at the end panels 1 and N are adjusted to adopt the points after and before the chosen panels respectively.

The airfoil new coordinate as calculated from the above described cubic interpolation scheme is described for VDV airfoil and the plot is given in Figure (3.8). The plot shows the input points to be interpolated (VDV airfoil input) and the interpolated coordinates.

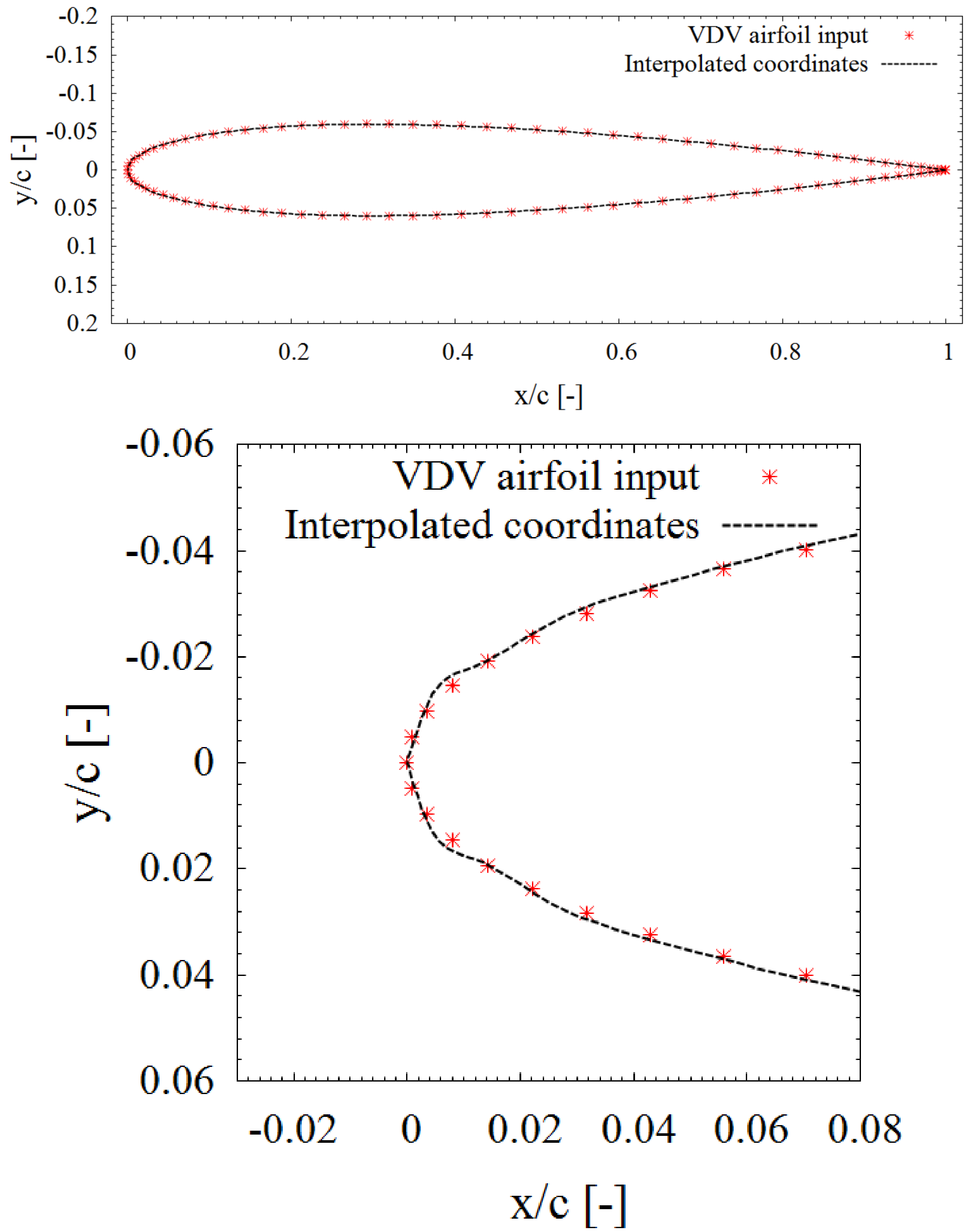

Figure 3.8: Original and interpolated coordinates of VDV airfoil.

As it is evident from the above figure, the interpolation fails when the change in y coordinates varies rapidly with respect to x, i.e. at the highly curvatured region of the airfoil. Hence an alternate formulation is made with usage of distance as a new coordinate system instead of x and y as used in the interpolation in the above equations. This will make the system monotonically increasing with respect to x rather than non-monotic function as with x and y system. This in turn reduces the oscillations near the leading edge. The following Figure (3.9) shows the new interpolation results (interpolation with distance) with the old interpolation (interpolated coordinates) and the original input airfoil coordinates.

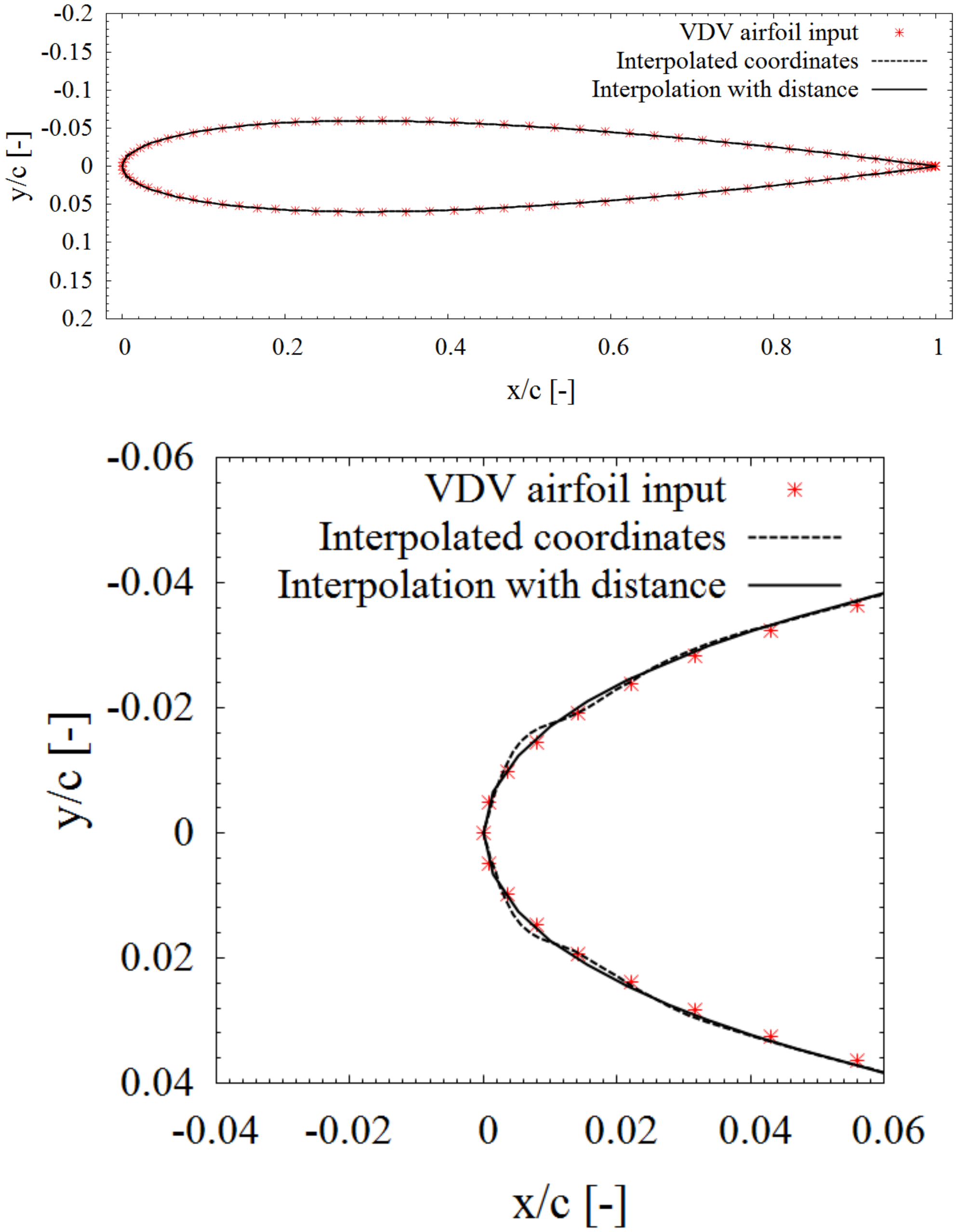

Figure 3.9: Original and two different types of interpolated coordinates of VDV airfoil.

It can be seen that the new interpolation maps accurately with the original coordinates. This interpolation is used for the rest of the implementation. The points need to be clustered at the trailing edge and at the position where the velocity becomes maximum at the airfoil surface. This would ensure overcoming the deficit from the previous section of predicting low peak suction pressure and trailing edge pressure.

3.2.2 Comparison of pressure coefficient (C_p) to choose optimal airfoil panels

Figures (3.10) and (3.11) show C_p distribution of NACA0012 for various number of panels with and without clustering of panels at the trailing edge and at position where the peak suction is present, along with XFOIL result. Both figures depict the same C_p but indicates different critical regions where the variations can be seen prominently. The clustering of the panels is done based on the calculated velocity from the first iteration with the interpolated airfoil coordinates. The position where the velocity is zero for the given AoA is taken to be the stagnation point. The clustering of airfoil panels around the peak suction pressure region and the trailing edge incorporates 10 times the points that are on the surface of the airfoil. It can be seen from the figures that clustered panels yield accurate results with respect to XFOIL compared to unclustered panelling. Further, 300 panels over airfoils with clustering yield results equivalent to any higher panelling on the surface and better results than using 200 panels. Hence the number of panels over airfoils is chosen to be 300 with clustering.

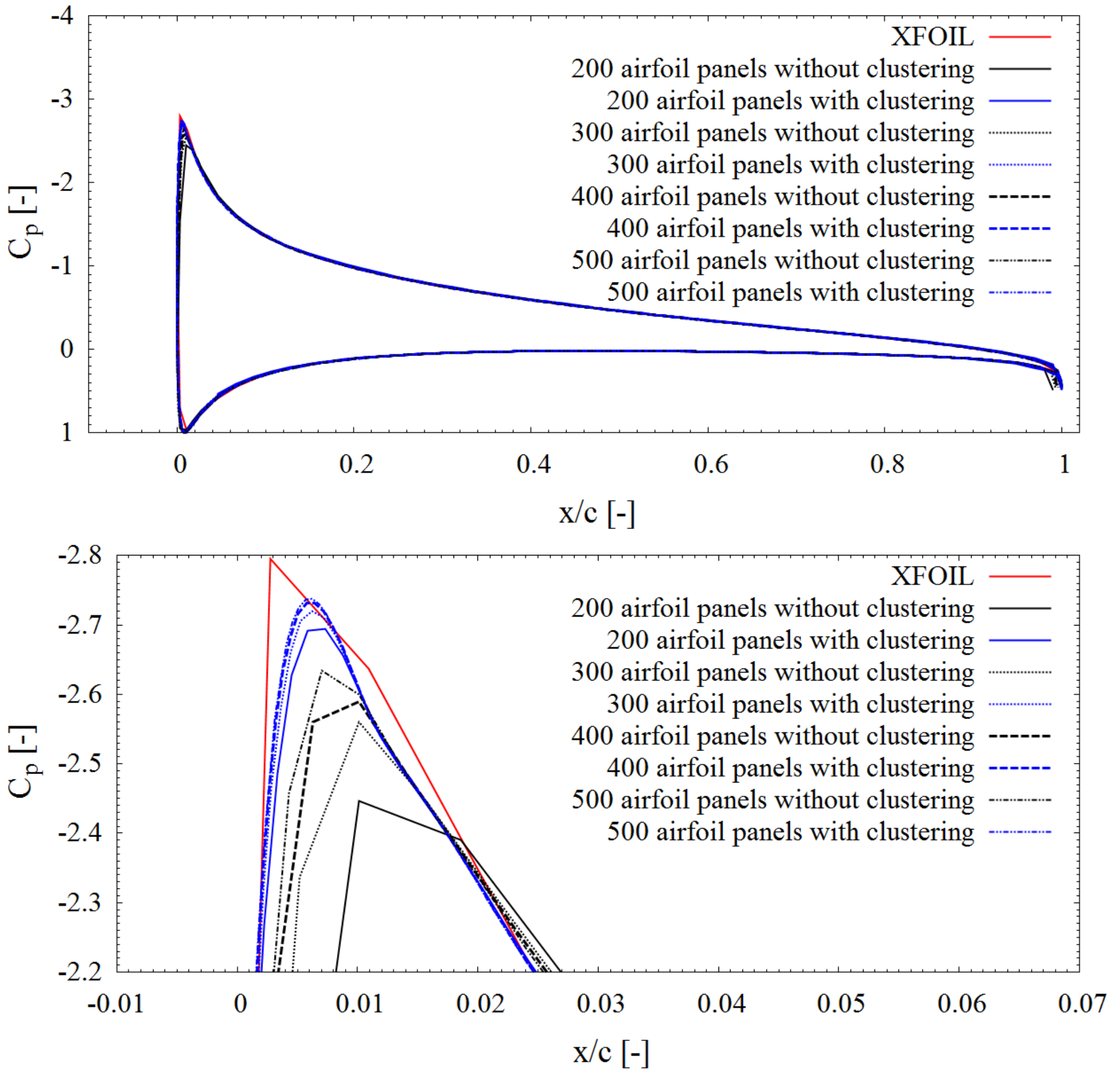

Figure 3.10: Cp distribution for NACA0012 at angle of attack of 6 degrees with and without clustering showing complete C_p distribution (top) and peak suction pressure (bottom).

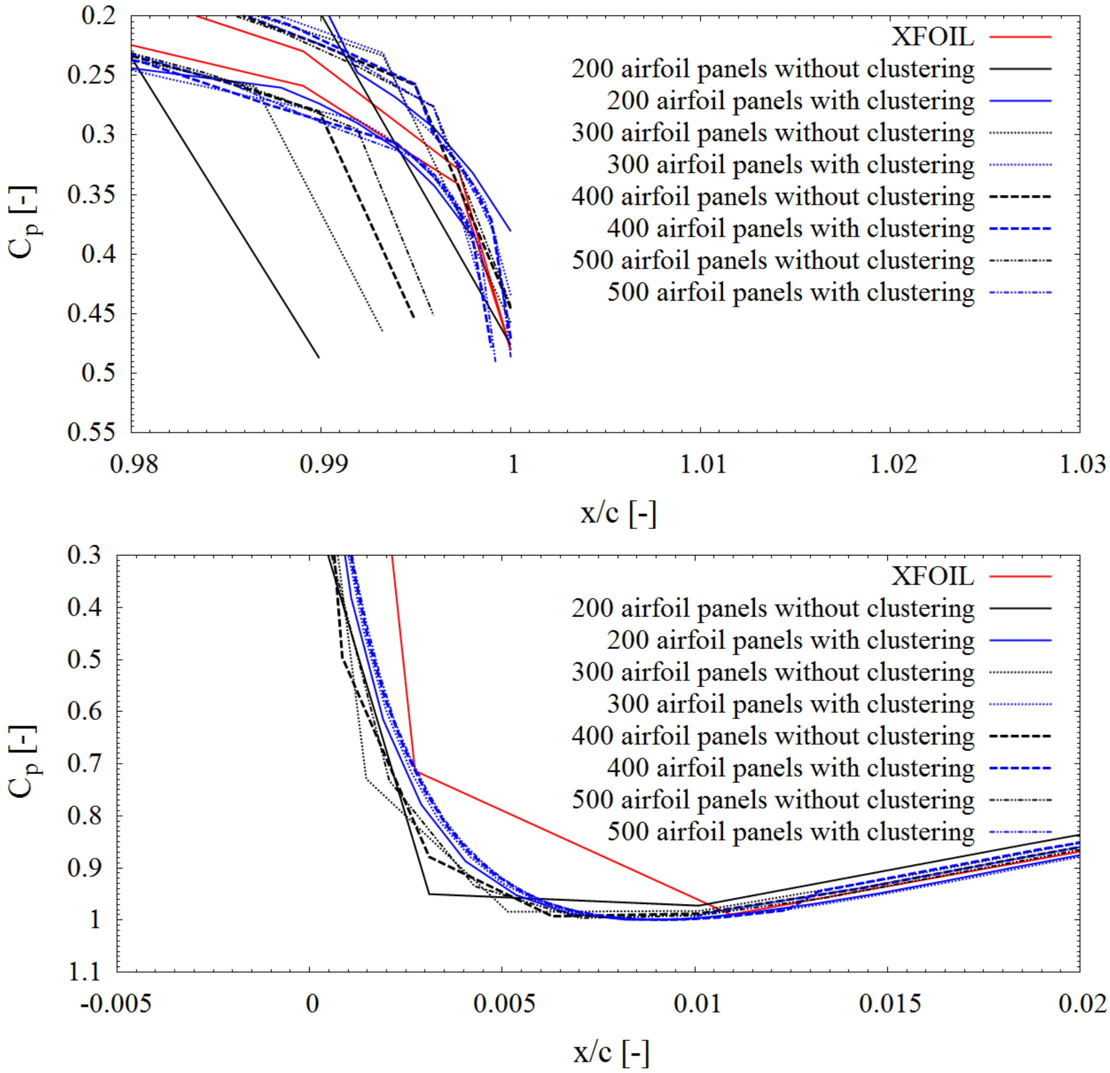

Figure 3.11: Cp distribution for NACA0012 at angle of attack of 6 degrees with and without clustering showing the trailing edge (top) and the beginning of the pressure side (bottom).

3.3 Wake at the trailing edge

From Helmholtz theory as stated in section (3), it is neccessary to consider the wake at the trailing edge for inviscid, incompressible flow modelled with vortex elements. The wake behaves differently from the bounded flow by not creating any loads, as it is not a solid surface like airfoil. The wake shape and inclination of the released wake along the trailing edge of the airfoil, as a result of linear vortex singularity elements over airfoil surface, is calculated based on Biot-Savart law. The vortex strength of the wake panels is zero. Here, the total wake length is taken to be one chord length similar to that of RFOIL. The wake is divided into many wake panels with collocation point at the midpoint of each wake panel. The velocity induced at each collocation point as a result of all the vortex singularity elements on the airfoil surface is determined. The first collocation point on the wake is varied between 10^{-1} and 10^{-5} in the x direction for the first iteration. The obtained result for the different positions of the first collocation point remains the same. Based on the normal and tangential local velocities, the first panel of the wake is calculated by iterative procedure, for its shape till the difference in the angle between subsequent iterations becomes the order of 10^{-4} tolerance. Then the second collocation point is chosen at the same angle as the previous converged panel. Again several iterations were carried out to reach the same level of convergence as the first panel. The same procedure is followed for all the remaining panels in the wake to get the resultant converged wake shape with all the chosen panels. The distance for each collocation point is chosen with constant and increasing size wake panels ranging from 10 to 500 for this single wake at the trailing edge. All the panels ranging from 10 and 500 are incorporated at the distance of one chord wake length. The optimum number of wake panels required for accurate result is studied for all the above condition. As an example case, the result is shown in the Figure (3.12) for VDV airfoil of 12% thickness for constant and increasing size wake panels.

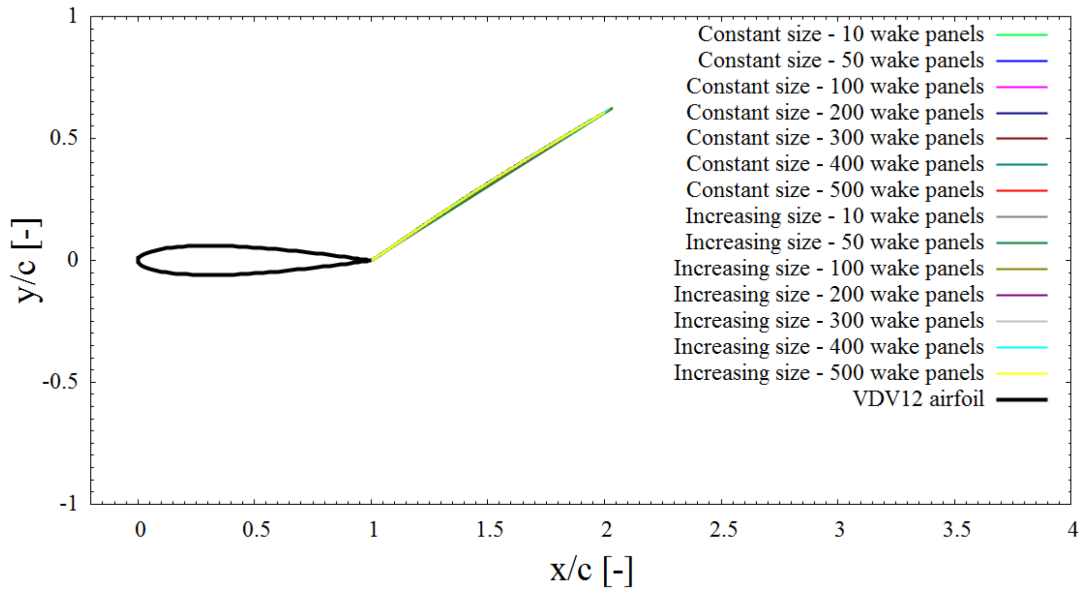

Figure 3.12: Wake panels of constant and increasing size.

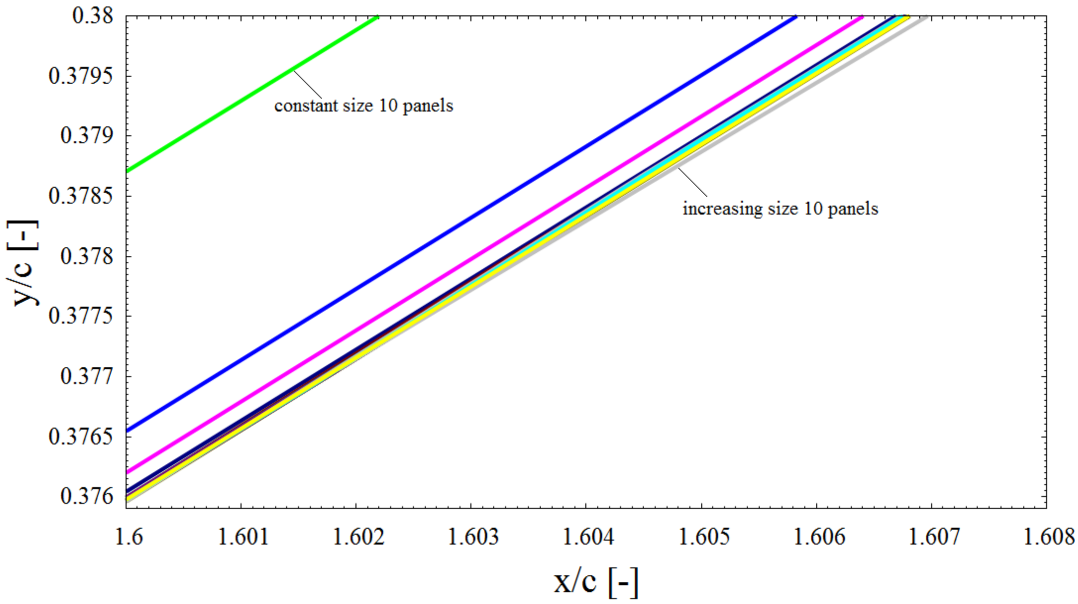

Figure 3.13: A zoom-in of constant and increasing size wake panels.

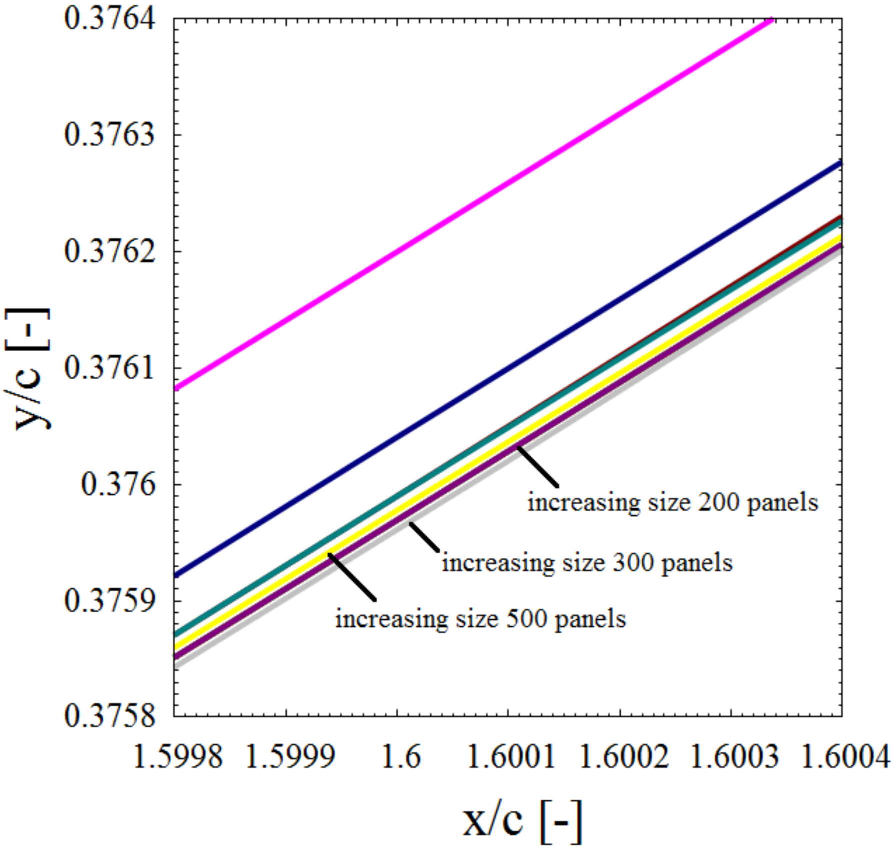

Figure 3.14: A zoom-in of increasing size wake panels.

As can be seen from the Figure (3.13), the increasing size wake panels show better results than constant size wake panels of equal numbers. Further from the Figure (3.14), among the increasing size panels not much difference can be observed for wake panels of 200 to 500 and so the wake panels is chosen to be increasing size 200 panels, beyond which increasing the number of panels does not affect the orientation of the panels with converged solution.

With the number of wake panels (200), the wake orientation for different angle of attacks from -21 to 21 degrees is studied for VDV airfoil of 12% thickness to check the correctness of single wake implementation. The plot is shown in the Figure (3.15).

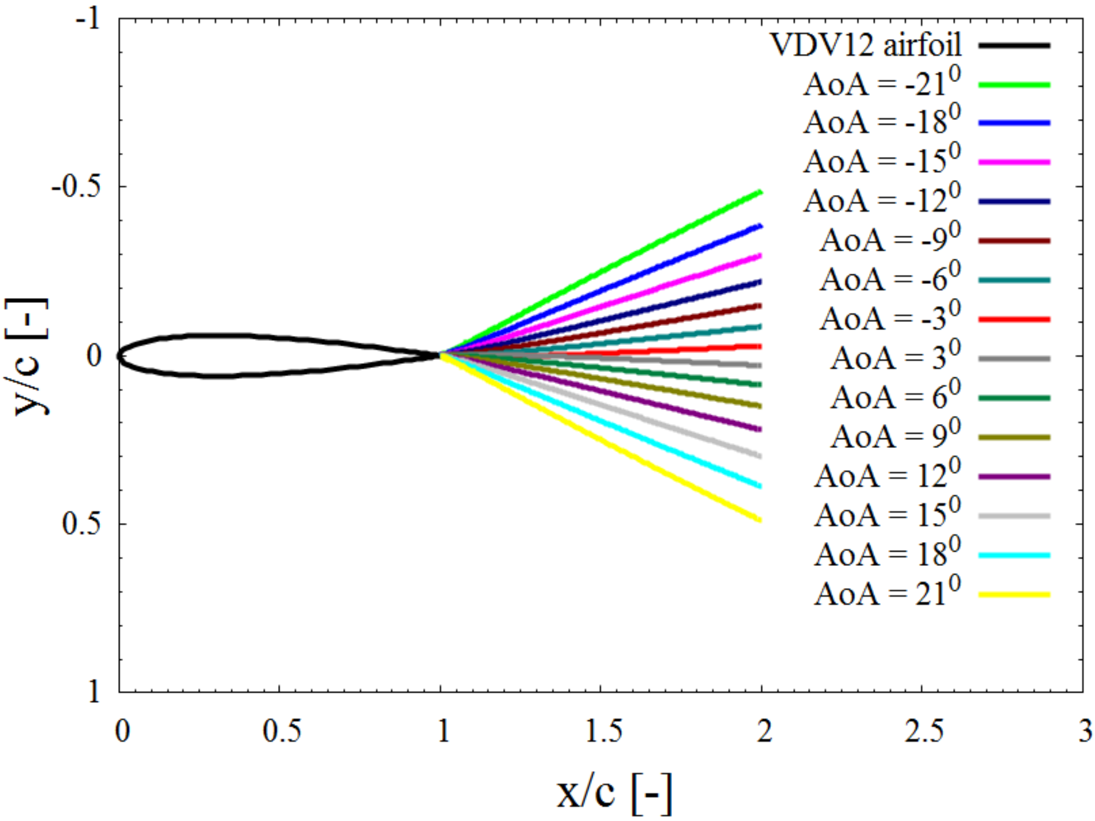

Figure 3.15: Plot of single wakes at the trailing edge for VDV airfoil at various angle of attacks.

As the airfoil is symmetric about x-axis the orientation of the wake is also symmetric for respective positive and negative angle of attack. This asserts the successful implementation of single wake inviscid solution.

Chapter 4

Inviscid double wake model

The single wake inviscid model describes the inviscid flow region. This could be combined with the integral boundary layer equations to model the viscous effects for the attached flow. Once the separation sets in, double wake inviscid model could be used to model the effects of the separated flow region. This is due to the nature of the separated flow. In the viscous region i.e. inside the boundary layer, there exists velocity gradient and so vorticity is formed. The formed vorticity can not be destroyed and so it is convected and diffused in the flow. In the outer flow regime, i.e. the inviscid region, there is no velocity gradient and so no vorticity is formed. When the flow separates, all the vorticity that is formed in the viscous region is convected downstream from the separation point and from the trailing edge. In this double wake inviscid model, one of the wakes is released from the point of separation and the other wake is released from trailing edge. In this region between the two wakes, the vorticity is negligible leading to negligible losses and so total pressure remains constant. This indicates that there is no shear layer in the region between the two wakes. Therefore, from the separation point until the trailing edge, the flow can be assumed to be purely inviscid. Hence, double wake inviscid model holds good to represent the separated flow region. However, the non-separated flow region over airfoil in separated flow requires the combination of panel method and the integral boundary layer equations to model the viscous effects. The double wake inviscid model can be done for both conventional sharp trailing edge and blunt trailing edge airfoils.

To model the secondary wake, the separation point needs to be known. It is given as an external input for the double wake inviscid model. The point of separation can be taken from experiment or found from viscous flow either from XFOIL or RFOIL. (When the double wake inviscid model is implemented in RFOIL, the separation point will be found at the first iteration of RFOIL simulation). The given external separation point is inspected for its location over the panels. This is done by calculating the cross-product of the given separation point with each of the panel's end points. The panels whose cross product with the input separation point is zero is found to be the appropriate panel as the point is collinear with the panel. Once the given separation point is found to be in any of the panels, the point is moved to the nearest panel end point. This method of fixing separation point at panel end is done to facilitate easier implementation. Further, as there are large number (300) of panels on the airfoil surface, the given separation point even if moved to the nearest end panel point does not vary significantly.

The double wake inviscid model is developed from single wake inviscid model. It is implemented with some changes on the calculated induced velocities, its influence over calculating the wake shape, the Kutta condition and with and without wake vortex strength. The formulation of the singularity elements and the method of calculating the induced velocities remains the same as that of the single wake inviscid model. In order to implement double wake model, several possibilities were tested. For the sake of clarity all the methods which were unsuccessful are listed in section (4.1) and the successful implementation is shown in the section (4.2).

4.1 Methods leading to non-physical solutions

4.1.1 Changing only the influence coefficient matrix

In this method, linear vorticity element distribution is used as that of single wake inviscid model. All the formulations of the single wake along with the Kutta condition is maintained the same. The induced velocity on the panel edge is given by,

$$u_{i,j}, w_{i,j} = (U_{al}, W_{al})_{i,j} + (U_{bl}, W_{bl})_{i,j-1}. \tag{4.1}$$

where, i is the collocation point and j represents panel end points. U_{al}, W_{al}, U_{bl} and W_{bl} are given by equation (3.12) in the inviscid single wake formulation. Only the induced velocity at the separation point as a result of the panel influence just after the separation point is made zero. Hence, the induced velocity at separation point is,

$$u_{i,SEP}, w_{i,SEP} = (U_{al}, W_{al})_{i,SEP}. \tag{4.2}$$

This makes the local vortex strength at the separation point located at the panel edge to be very small. This is done to facilitate the vorticity shedding to convect downstream. The vortex strength of both the wakes is zero. The corresponding changes in the influence coefficient matrix $A_{i,j}$, representing the normal component of the induced velocity for N collocation points along with one Kutta condition, is shown by the matrix below,

$$A_{i,j} = \begin{bmatrix} u_{1,1} & u_{1,2} & u_{1,3} & \dots & u_{1,SEP} & \dots & u_{1,N+1} \\ u_{2,1} & u_{2,2} & u_{2,3} & \dots & u_{2,SEP} & \dots & u_{2,N+1} \\ \vdots & \vdots & \vdots & \ddots & \vdots & \ddots & \vdots \\ u_{N,1} & u_{N,2} & u_{N,3} & \dots & u_{N,SEP} & \dots & u_{N,N+1} \\ 1 & 0 & 0 & \dots & 0 & \dots & 1 \end{bmatrix}. \tag{4.3}$$

The vortex distribution on airfoil surface with the change of influence coefficient at the separation point is shown in the Figure (4.1).

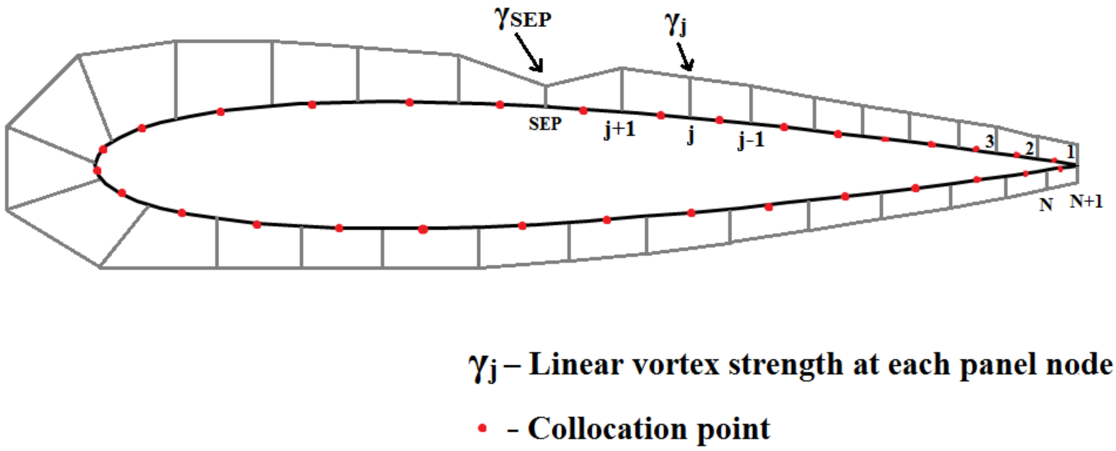

Figure 4.1: A sketch of linear vortex strength distribution on airfoil surface for double wake formulation

The changes in the influence coefficient give rise to changes in the peak suction pressure and changes in the trailing edge pressure coefficient as shown in Figure (4.2).

Pressure coefficient

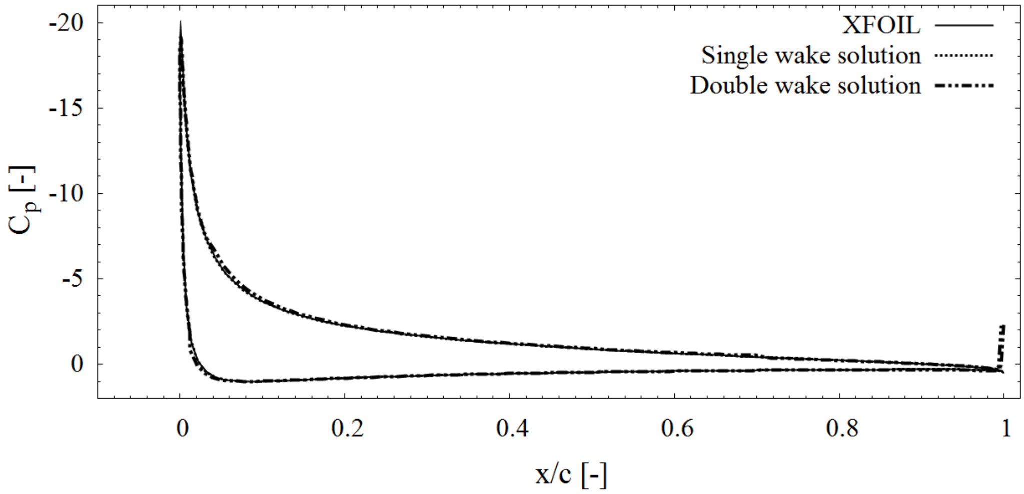

[a]

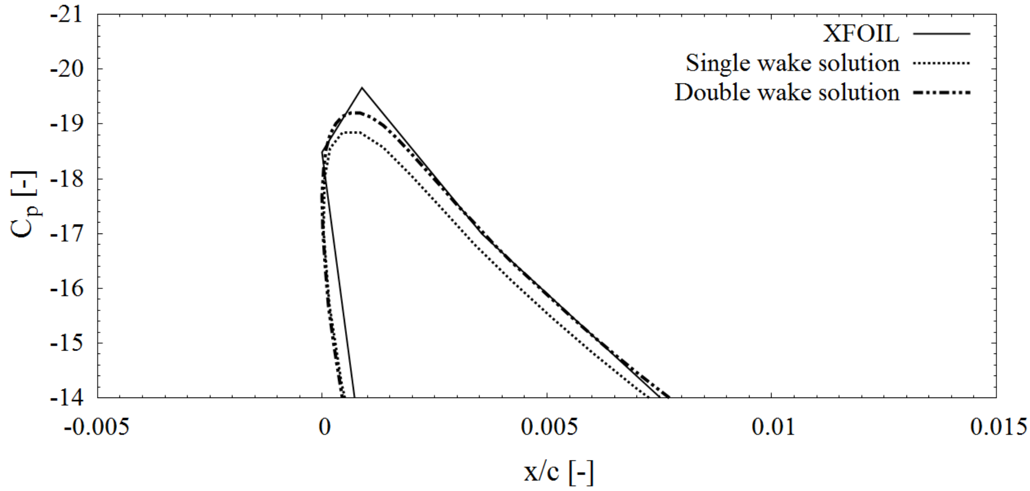

[b]

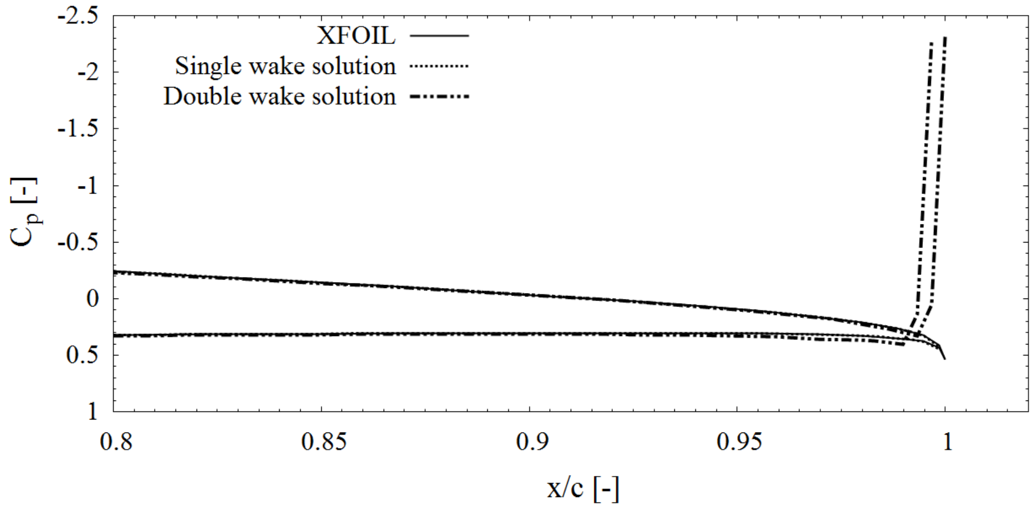

[c]

Figure 4.2: Comparison of pressure coefficients, at AoA of 18° for VDV airfoil obtained by double wake model, single wake model and XFOIL [a], a zoom in to pressure peak at the leading edge suction side [b] and to the trailing edge [c].

Figure (4.2) shows the double wake with the above mentioned condition with respect to the single wake and XFOIL results for VDV 12% thick airfoil at AoA of 18°. The separation point is located at $x/c = 0.71$ and is taken from the viscous simulation of XFOIL. Figure (4.2[a]) shows that the peak suction pressure of double wake result is more than that of single wake. Figure (4.2[b]) shows the pressure from the suction side becomes higher than that from the pressure side at certain point along the airfoil near the trailing edge. Further downstream at the trailing edge the pressures from both the suction and pressure side are equal but negative due to the implementation of Kutta condition at the trailing edge. This represents non-physical solution of the separated region and so this formulation is not suitable for the double wake implementation.

4.1.2 Changing both Kutta condition and the influence coefficient matrix

This method of double wake implementation is performed by changing the Kutta condition along with the changes described in subsection (4.1.1), in the influence coefficient matrix. This is a realistic way to describe the constant pressure coefficient along the airfoil surface in the flow reversal region. The Kutta condition describing the equal pressure at the trailing edge panels $\gamma_1 + \gamma_{N+1} = 0$ is changed to either of the two following cases based on positive or negative angle of attack respectively:

$$\begin{aligned} \gamma_{N+1} + \gamma_{SEP} &= 0, \\ \gamma_1 &= 0, \end{aligned} \tag{4.4}$$

$$\begin{aligned} \gamma_1 + \gamma_{SEP} &= 0, \\ \gamma_{N+1} &= 0. \end{aligned} \tag{4.5}$$

These conditions indicate equal pressure at the separation point and at the trailing edge. The new influence coefficient matrix $A_{i,j}$ with the above mentioned changes is described in the matrix below (shown for positive angle of attack):

$$A_{i,j} = \begin{bmatrix} 1 & 0 & 0 & \dots & 0 & \dots & 0 \\ u_{1,1} & u_{1,2} & u_{1,3} & \dots & u_{1,SEP} & \dots & u_{1,N+1} \\ u_{2,1} & u_{2,2} & u_{2,3} & \dots & u_{2,SEP} & \dots & u_{2,N+1} \\ \vdots & \vdots & \vdots & \ddots & \vdots & \ddots & \vdots \\ 0 & 0 & 0 & \dots & 1 & \dots & 1 \\ \vdots & \vdots & \vdots & \ddots & \vdots & \ddots & \vdots \\ u_{N,1} & u_{N,2} & u_{N,3} & \dots & u_{N,SEP} & \dots & u_{N,N+1} \end{bmatrix}. \tag{4.6}$$

The wake at both the trailing edge and from the separation point are calculated in the same way as described in the inviscid single wake model in the section (3.3). The vorticity strength of both the wakes is also kept zero as in the previous method. Here the influence coefficients are changed to convect the wake downstream with negligible local downstream vorticity at the separation point. Figure (4.3) shows the wake for the attached and Figure (4.4) for separated flow at angle of attack of $18°$ and $-18°$. The separation point are fed manually from the repective results for viscous flow simulation obtained by XFOIL.

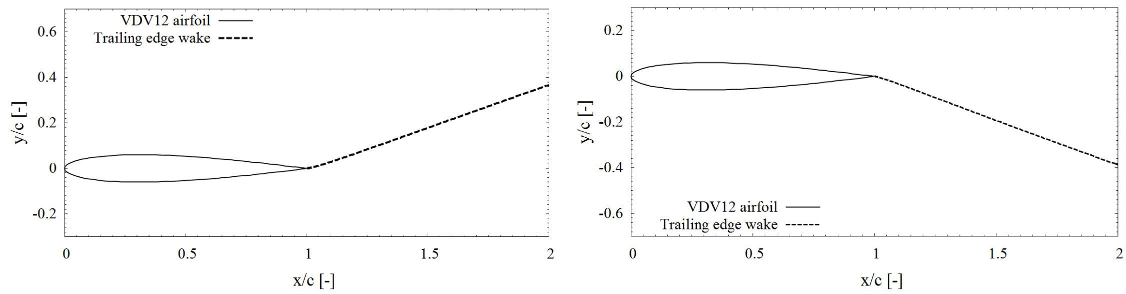

Figure 4.3: Wake shape from single wake model for VDV airfoil at AoA of $18°$ (left) and $-18°$ (right)

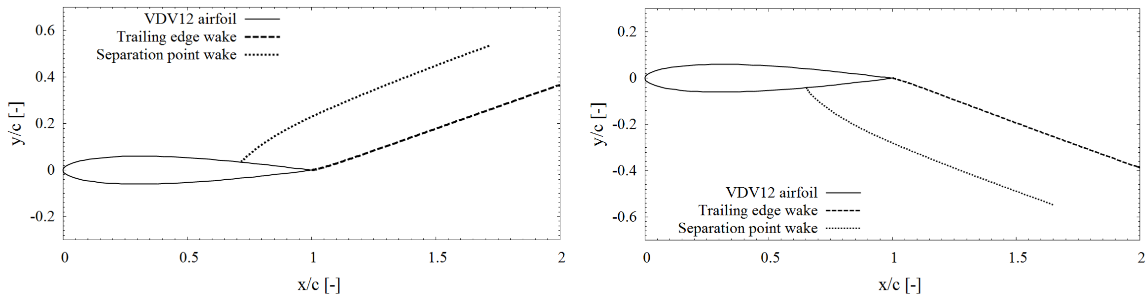

Figure 4.4: Wake shape from double wake model for VDV airfoil at AoA of $18°$ (left) and $-18°$ (right)

Pressure coefficient

Figure (4.5[a]) shows double wake inviscid pressure distribution with respect to the single wake and XFOIL results for VDV airfoil at AoA of 18°. The implementation has changes in the influence matrix with imposed Kutta condition between separation point and trailing edge. The separation point is located at $x/c = 0.71$ and is taken from viscous simulation of XFOIL. Figure (4.5[b]) shows that the peak suction pressure of the double wake is less than that of single wake. In the Figure (4.5[c]) it can be seen that the suction and pressure side of the trailing edge reaches positive and negative pressure respectively. Though the implementation is expected to give unique physical solution with the enforced Kutta condition, this method seems to produce non-physical solution as the pressure from suction and pressure side of the trailing edge are unequal and the method does not model the constant pressure in the separated region.

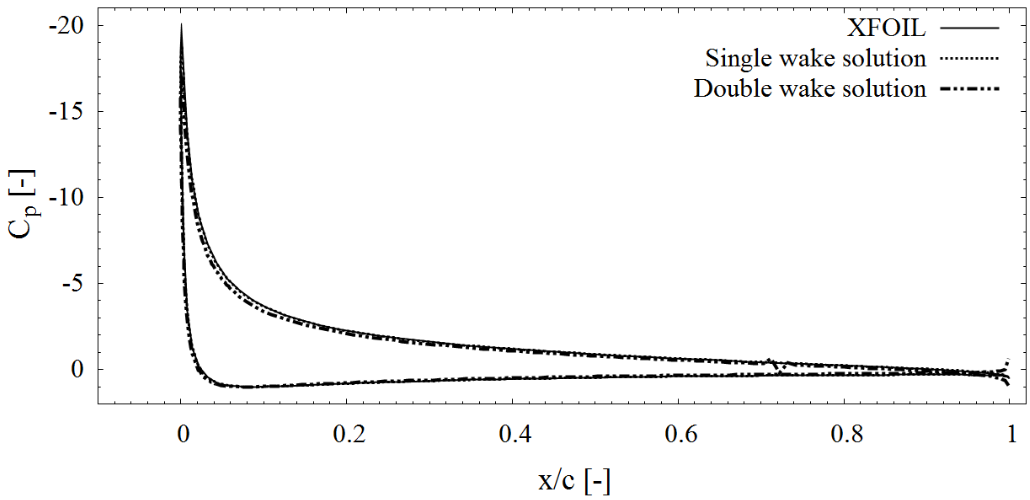

[a]

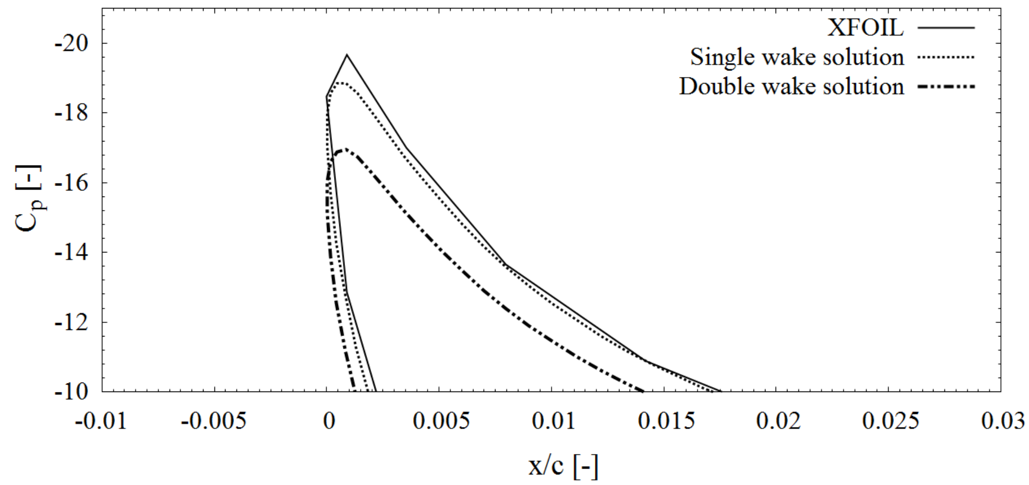

[b]

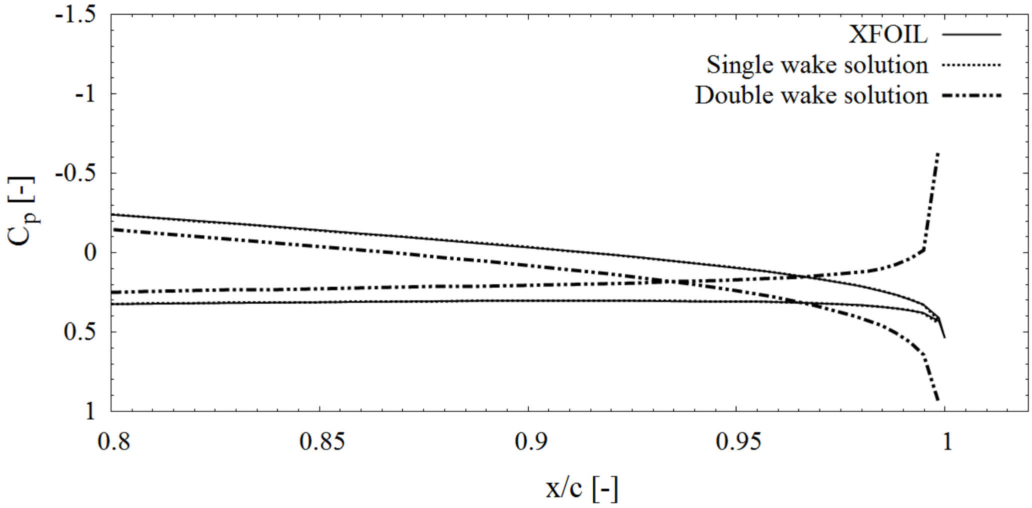

[c]

Figure 4.5: Comparison of pressure coefficients, at AoA of 18° for VDV airfoil obtained by double wake model, single wake model and XFOIL [a], a zoom in to pressure peak at the leading edge suction side [b] and to the trailing edge [c].

4.1.3 Changing pressure coefficient calculation on inviscid wake

In the steady state flow considerations, the effect of wake on the flow around the airfoil is usually ignored. However, the wake has significant effects on the estimation of aerodynamic forces. The double wake implementation in the previous section shows that in the suction side, the pressure coefficient increases along the airfoil towards the trailing edge. The trend and the rate of increase of pressure are not desirable. In all the separated flows, the pressure coefficient remains constant beyond the separation point to the trailing edge due to flow recirculation. The ability to mimick this effect is investigated by considering the pressure distribution on the secondary wake that is released from the separation point instead of corresponding airfoil surface only in the separated region. The influence coefficients and Kutta condition are same as that of the previous section (4.1.2). The vorticity strength of the wakes are also retained as zero. The separation and trailing edge wake shapes are calculated from the induced velocity of the linear vortex elements on airfoil surface as described in single wake inviscid model in section (3.3).

The pressure coefficient on the wake at separation point is calculated using Biot-Savart law. By using this theorem, the velocity induced on the inviscid wake as a result of the vortex filaments on the airfoil surface can be calculated. Once this is done, the pressure coefficient along the wake is calculated.

Mapping collocation points on the wake

In order to calculate pressure coefficient on the wake, equivalent points need to be defined on the wake as that of the collocation points on the airfoil, from separation point until the traling edge. This is done by finding the point of intersection of all the wake panels, say 200, and the vertical line from the collocation point on airfoil. The vertical line equation from the collocation point is given by,

$$x = x_{collocation}. \tag{4.7}$$

The wake panels are considered to be flat for simplicity and so straight line equation is used, as described by,

$$y_{intersection} = (y_2 - y_1)\frac{x - x_1}{x_2 - x_1} + y_1. \tag{4.8}$$

x_1, x_2 and y_1, y_2 are the x and y coordinate of wake panel end points respectively. From the equations (4.7) and (4.8), the points on the wake can be calculated and is described in the Figure (4.6).

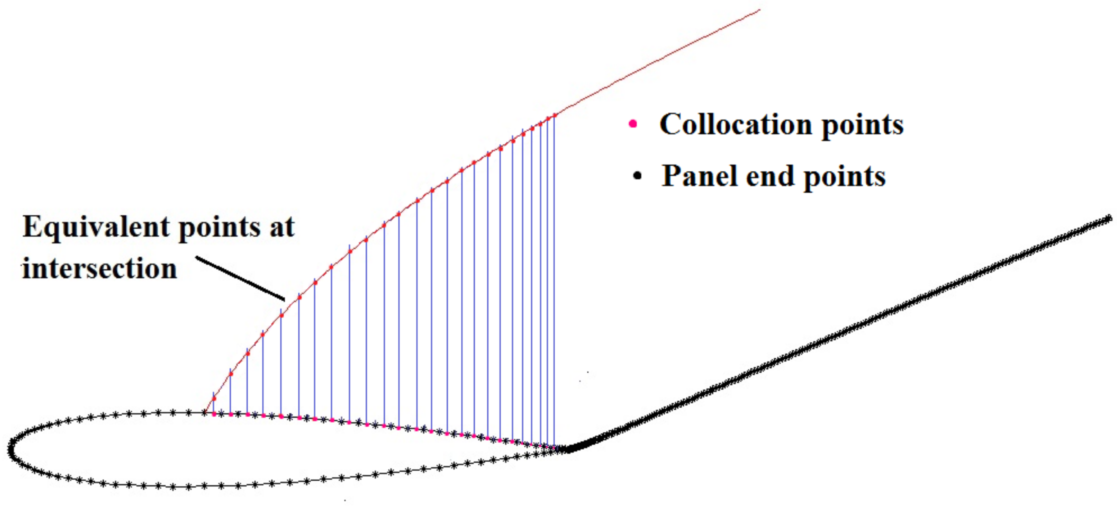

Figure 4.6: A sketch of mapping the collocation points on the separation wake.

Velocity and C_p on the wake

The total velocity at each point on the wake mapped corresponding to the collocation points on airfoil surface, is calculated as a sum of the induced velocity and the freestream velocity. The induced velocity at each of the equivalent points located just outside the separated flow region, is the result of all the vorticity influences located on the airfoil and is based on Biot-Savart law. From the calculated total velocity, the pressure coefficient is calculated from

$$C_p = 1 - \frac{q^2}{{U_0}^2}. \tag{4.9}$$

Figure (4.7) shows the C_p plot for VDV airfoil at AoA of 18°. The C_p is calculated on wake in the separation region instead of airfoil surface. The separation point is located at $x/c = 0.71$ and is obtained from viscous simulation of XFOIL. It can be seen that the suction side pressure coefficient has improved considerably compared to the previous results. However, the pressure distribution on the pressure side of the airfoil is still non-physical i.e. the flow does not leave the trailing edge smoothly. Also, the complete separation phenomena is not captured with this approach.

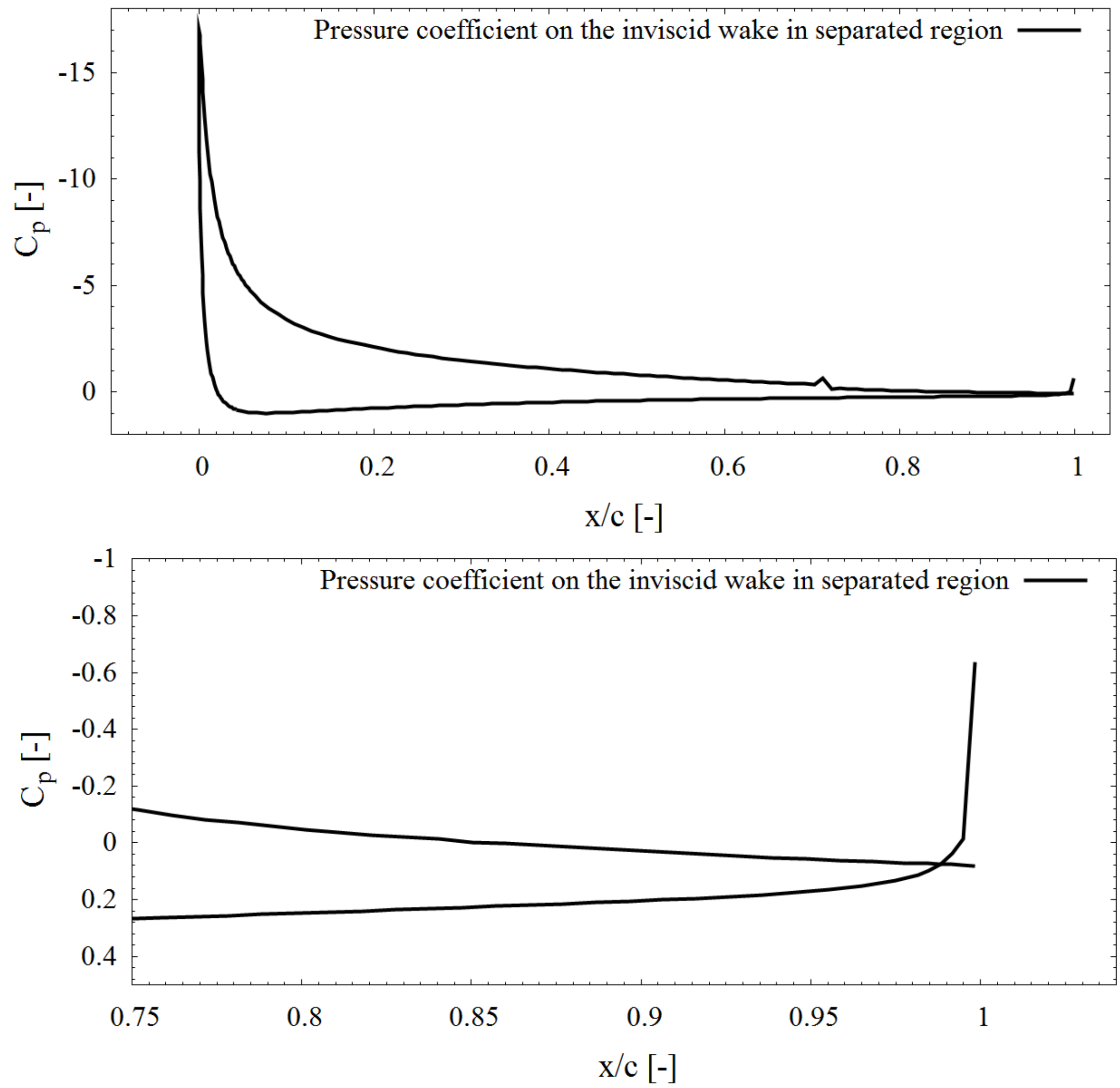

Figure 4.7: Pressure coefficient, at AoA of 18° for VDV airfoil obtained by double wake model, calculated on wake in the separation region (top), a zoom in to the trailing edge (bottom).

4.1.4 Separation wake influence over airfoil surface vortex singularity element distribution

Subsequent to the non-physical representation of inviscid flow in the previous section, the influence of wake on the vortex singularity elements over the airfoil surface mimicking the invicid flow is studied. As per the Kutta condition the flow needs to leave the airfoil smoothly. Here, the Kutta condition is applied between the point of separation and the trailing edge and so both the wakes are expected to leave smoothly from their respective positions from the airfoil surface. The wake released at the trailing edge of the airfoil is smooth compared to the wake released from the separation point. This is evident from orientation of the near wake panels of the trailing edge wake which bisects the angle between the airfoil trailing edge panels at the suction and pressure side. However, this is not the case with the second wake from the separation point. The near wake panels from the second wake is oriented at a very large angle with its neighbouring airfoil panels, making the flow from the airfoil surface to leave less smoothly at the separation point and thereby making it less physical. The wake orientation can be seen from the Figure (4.8).

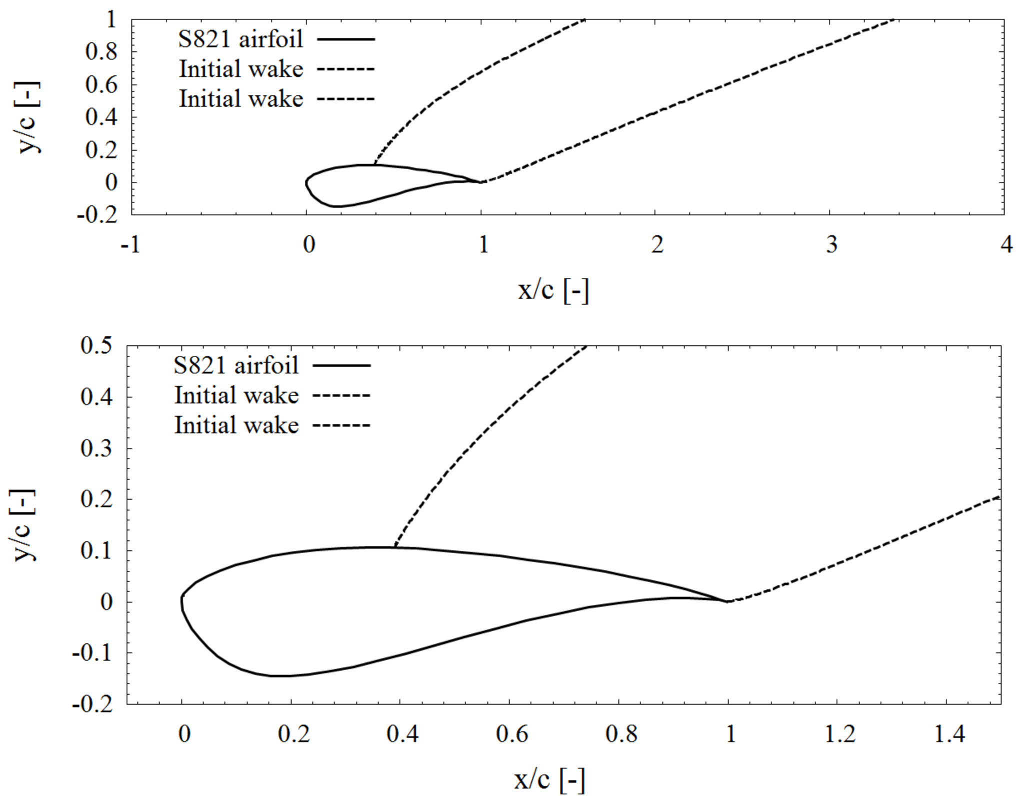

Figure 4.8: S821 airfoil with the initial wake shapes (top) and a zoom-in to the near wake region (bottom).

Therefore, constant vortex singularity elements are introduced in the converged wake panels of the initial second wake. A representation of the vorticity distribution is shown in Figure (4.9). Only the case with positive AoA is used for representation.

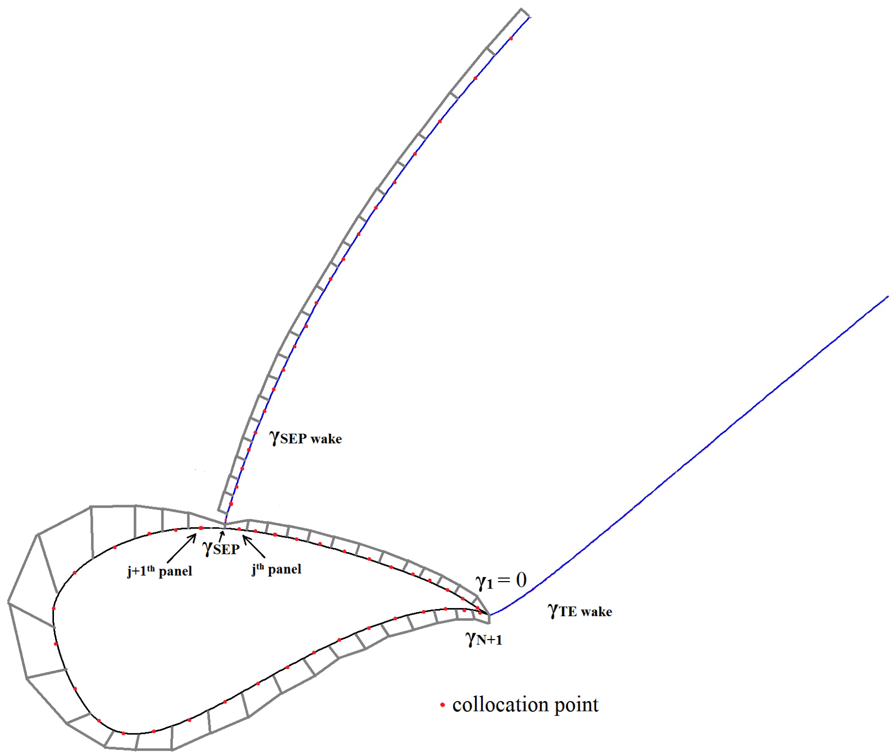

Figure 4.9: A sketch of the vorticity distribution on the airfoil surface and on the wake at the separation point.

The induced velocity of the linear vortex elements on airfoil surface is used for the above calculation without the influence of the immediate downstream panel at the separation point. The initial wake shape of the separation and trailing edge wakes are calculated similarly as described in section (3.3).

The vorticity strengths on the airfoil and wake panels can be iteratively calculated by considering the Neuman boundary condition including the vorticity strength of the second wake sheet. The strength of the vortices on the second wake is given by,

$$\gamma_{SEP} = \gamma_{SEP_{wake}}, \qquad (4.10)$$

where $\gamma_{SEP_{wake}}$ represents the vorticity distribution along the secondary wake. The boundary conditions are applied on the collocation points:

$$\sum_{j=1}^{N+1} A_{li,j}\,\gamma_j + \sum_{j=N+2}^{N+Nw+1} A_{ci,j}\,\gamma_j + (\vec{U}_0.n_i) = 0, \quad \text{for } i = 1 \text{ to } N, \qquad (4.11)$$

where Nw is the number of wake panels. The influence coefficient matrices $A_{l_{i,j}}$ and $A_{c_{i,j}}$ contain the induced velocities from linear vortex singularity elements on airfoil surface and constant vortex singularity elements on the separation wake respectively and is given by,

$$\begin{aligned} A_{l_{i,j}} &= u_{i,j}.n_i, \\ A_{c_{i,j}} &= u_{c_{i,j}}.n_i. \end{aligned} \tag{4.12}$$

The induced velocities in the influence coefficient matrix due to linear vortex strength element located on airfoil surface panels, is given by,

$$u_{i,j}, w_{i,j} = (U_{al}, W_{al})_{i,j} + (U_{bl}, W_{bl})_{i,j-1}. \tag{4.13}$$

where, i is the collocation point and j represents panel end points. Only the induced velocity at the separation point as a result of the panel influence just after the separation point is made zero. Hence, the induced velocity at separation point is,

$$u_{i,SEP}, w_{i,SEP} = (U_{al}, W_{al})_{i,SEP}. \tag{4.14}$$

As a result the vortex strength at separation point γ_{SEP} has reduced strength. This can be shown in the Figure (4.9) The induced velocities due to constant vortex strength element on the separation wake is by,

$$u_{c_{i,j}}, w_{c_{i,j}} = (U_{ac}, W_{ac})_{i,j}. \tag{4.15}$$

The induced velocities as a result of linear vortex singularity elements on the airfoil surface is described in section (3.1). The induced velocities as a result of constant vortex element in the wake panel is calculated in the panel coordinates as in Katz and Plotkin [6] and is given by

$$\begin{aligned} U_1 &= \frac{t_2 - t_1}{2\pi}, \\ W_1 &= -\frac{log\frac{d1}{d2}}{2\pi}. \end{aligned} \tag{4.16}$$

where, d_1 and d_2 represent the distance between the collocation point and the end points of each panel. t_1 and t_2 are the angles corresponding to d_1 and d_2 respectively. These variables are given in panel coordinates. Hence, the calculated induced velocities are transformed back to the global coordinates. They contribute to the aerodynamic influence coefficients and given by,

$$\begin{aligned} U_{ac} &= -U_1\, cos(\alpha_j) - W_1\, sin(\alpha_j), \\ W_{ac} &= -U_1\, sin(\alpha_j) + W_1\, cos(\alpha_j). \end{aligned} \tag{4.17}$$

and the influence coefficients matrix for positive angle of attack is given below,

$$A_{i,j} = \begin{bmatrix} 1 & 0 & 0 & \dots & 0 & \dots & 0 & 0 & \dots & 0 \\ u_{1,1} & u_{1,2} & u_{1,3} & \dots & u_{1,SEP} & \dots & u_{1,N+1} & u_{c_{1,1}} & \dots & u_{c_{1,j}} \\ u_{2,1} & u_{2,2} & u_{2,3} & \dots & u_{2,SEP} & \dots & u_{2,N+1} & u_{c_{2,1}} & \dots & u_{c_{2,j}} \\ \vdots & \vdots & \vdots & \ddots & \vdots & \ddots & \vdots & \vdots & \ddots & \vdots \\ 0 & 0 & 0 & \dots & 1 & \dots & 1 & 0 & \dots & 0 \\ \vdots & \vdots & \vdots & \ddots & \vdots & \ddots & \vdots & \vdots & \ddots & \vdots \\ u_{N,1} & u_{N,2} & u_{N,3} & \dots & u_{N,SEP} & \dots & u_{N,N+1} & u_{c_{N,1}} & \dots & u_{c_{N,j}} \\ 0 & 0 & 0 & \dots & 1 & \dots & 0 & 1 & \dots & 0 \\ 0 & 0 & 0 & \dots & 1 & \dots & 0 & 0 & \ddots & 0 \\ 0 & 0 & 0 & \dots & 1 & \dots & 0 & 0 & \dots & 1 \end{bmatrix}, \quad (4.18)$$

where, j corresponds to the position of the wake panels on the second wake.

Pressure coefficient

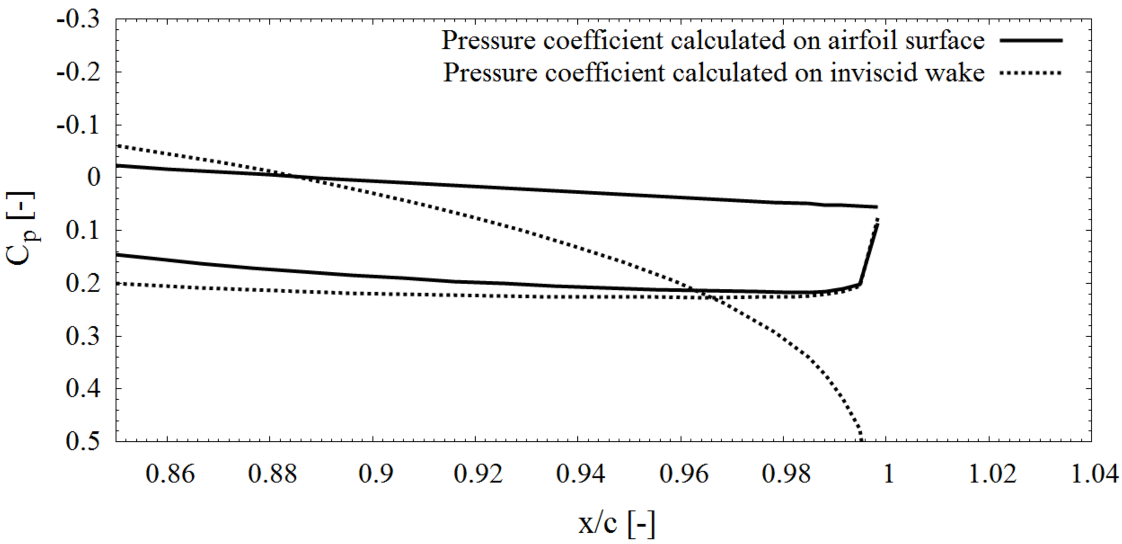

Figure 4.10: Pressure coefficient at AoA of 18° for VDV airfoil obtained by double wake model showing separated region.

The plot of pressure coefficient considering influence of the constant vorticity on the separation wake panels is shown in Figure (4.10). The separation point is located at $x/c = 0.71$ and is obtained as from viscous simulation of XFOIL. As an example, the C_p plot is shown with 50 wake panels. The dotted line in the plot indicates the C_p distribution taken over the airfoil surface in non-separated flow region and over the inviscid wake in the separated flow region. This pressure distribution seems non-physical as the pressure leaving the trailing edge of the airfoil are unequal. Also, the constant pressure in the separation region is not captured. The continuous line in the plot indicates the the C_p distribution taken completely over the airfoil surface. This plot shows that the pressure at the trailing edge from the suction and the pressure side is equal. The pressure coefficient variation in the suction side of the airfoil in the separated region is greatly reduced and thus the solution approaches physical representation. Hence the usage of the inviscid wake in the separation region is no more followed. Subsequent to this solution, the wake convergence and the requirement of number of wake panels in the second wake are studied. The study of number of wake panels is required, to understand the impact of the length of the wake on the obtained solution and to check if the length improves the result towards obtaining constant pressure in separated region.

Wake convergence at separation point

Following the newly calculated vorticity on the airfoil surface with constant wake singularity elements, the wake is recalculated until the entire wake orientation converges. The convergence criteria is taken to be the maximum difference in the calculated γ on the airfoil surface between successive iterations. The tolerance level of wake convergence have to be determined. The tolerance level for the convergence is varied from 10^{-1} to 10^{-5}.

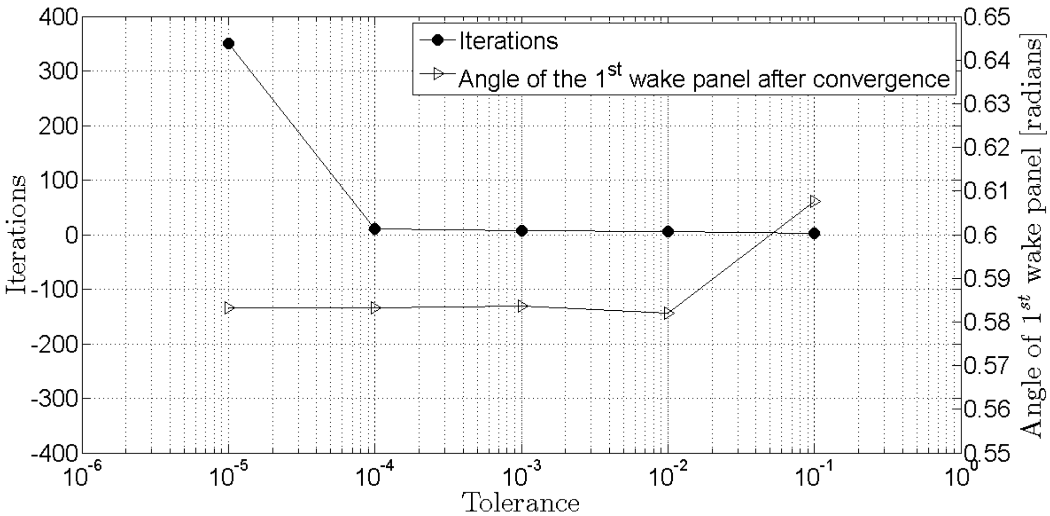

Figure 4.11: Plot of iterations and angle of first wake panel for various tolerance levels.

Figure (4.11) shows the plot of iterations required for the wake convergence for different tolerances along with the angle of first wake panel after convergence. The choice of first wake panel angle is due to the fact that the near wake orientation changes largely. It can be seen that the first wake panel angle remains constant beyond 10^{-1} level of convergence. Nevertheless, the iterations required for wake convergence increases rapidly beyond 10^{-4}. Further, the effect of tolerance level on the first wake panel angle of the converged wake is studied, for airfoils of various thickness ranging from 12% to 21% at various AoA. There is siginificantly less variation in the angle of first converged wake panel beyond the tolerance level of 10^{-2} as evident from the Figure (4.12). Therefore, the tolerance of 10^{-2} is chosen to be the required level to obtain converged wake.

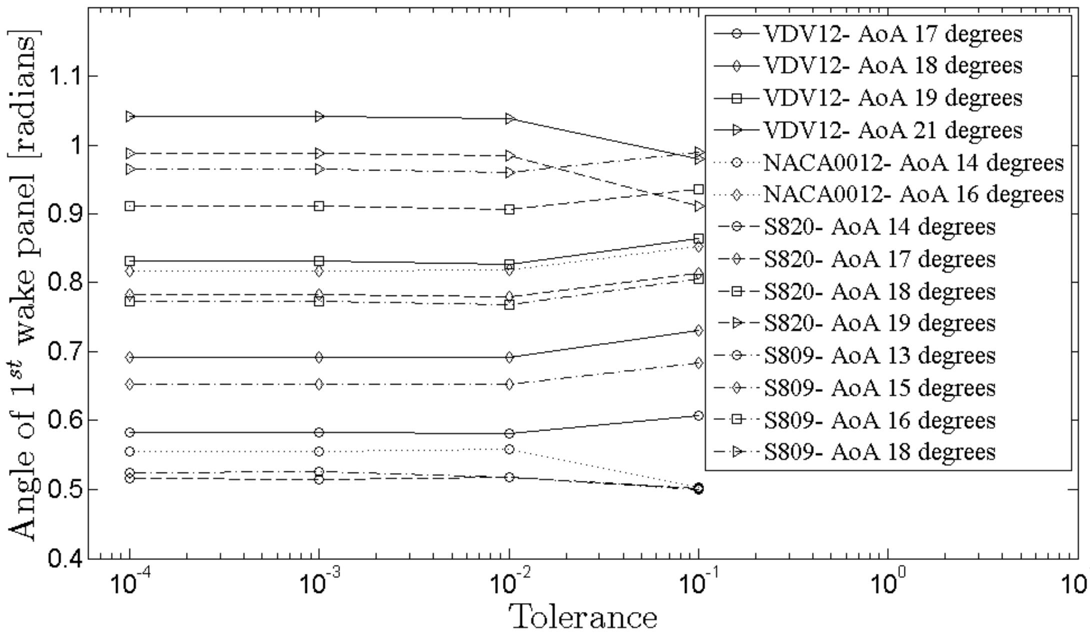

Figure 4.12: Plot of first wake panel angle with tolerance at various AoA for different airfoils VDV of 12% thickness, NACA0012 of 12% thickness, S820 of 16% thickness and S809 of 21% thickness.

Length and number of wake panels on second wake

As seen from the subsection (3.3), the increasing panel size is an optimal scenario for better results with less number of panels, the same increasing size panels are adopted for the second wake as well. The increasing size panels are obtained with the cosine distribution. *Here the length of the separation wake is not fixed to one chord length.* The number of wake panels and hence the length influences the pressure distribution.

The change in the number of wake panels varies the peak suction and trailing edge pressure distribution. An example of this dependency is shown in the Figure (4.13) using VDV airfoil at an angle of attack of 18°.

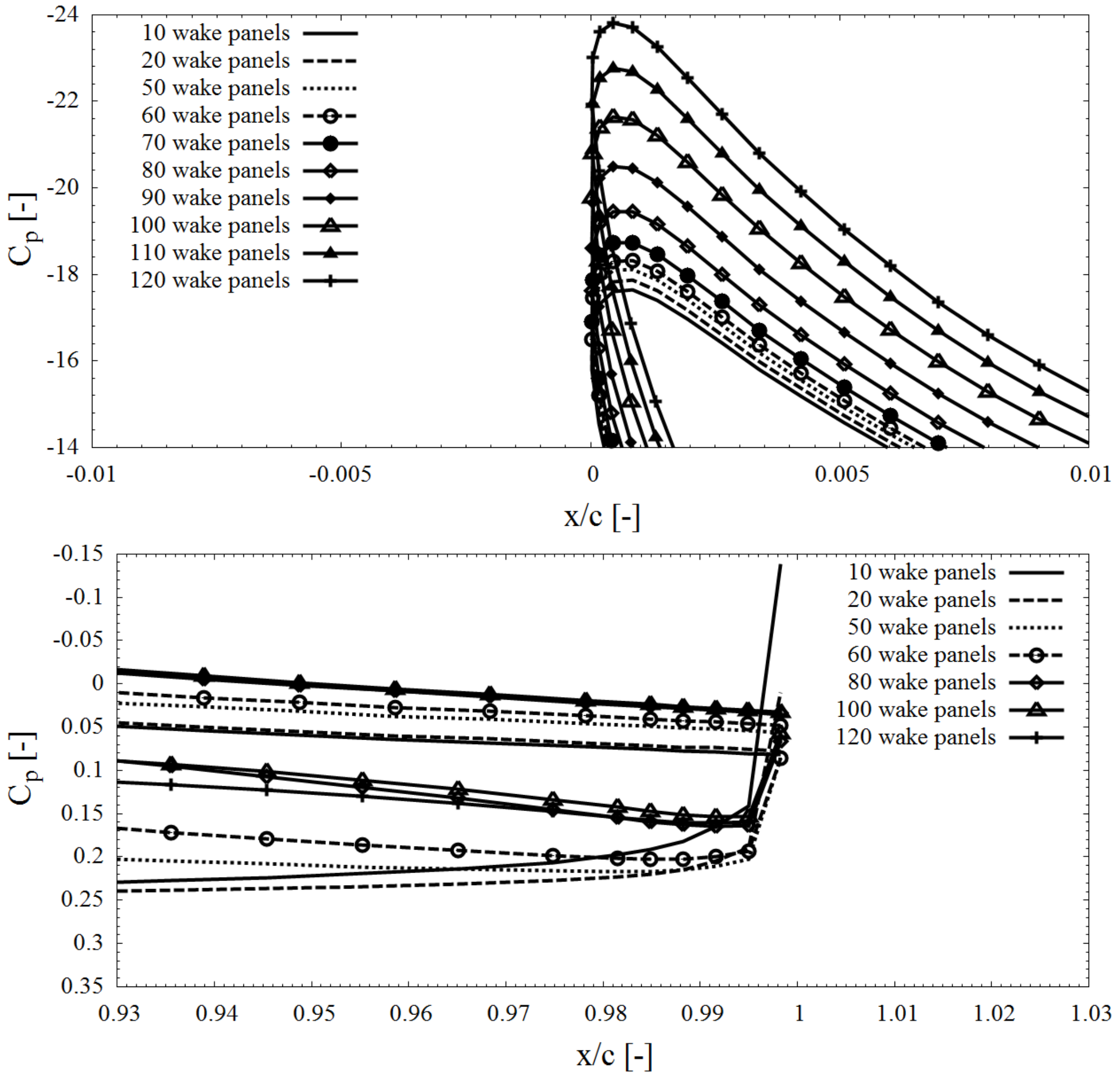

Figure 4.13: Pressure coefficients, at AoA of 18° for VDV airfoil, considering the influence of various wake panels, a zoom in to pressure peak at the leading edge suction side (top) and to the trailing edge (bottom).

It can be seen that the peak suction pressure increases with increasing number of panels. The C_p from both suction and pressure side leaving the trailing edge becomes equal as the number of panels increases. Nevertheless, the C_p changes with the number of panels in the suction and pressure side near the trailing edge. Sharp trailing edge airfoils with different thickness are analysed for various angle of attacks to get the optimal panel numbers required. As C_p gives the pressure distribution around the entire airfoil, it is difficult to conclude the number of wake panels required and so a single variable is required for each angle of attack and airfoil used. Therefore, the lift and the drag coefficients are used. The calculated C_l and C_d values are not correct as simulation is purely inviscid calculation. Nevertheless, the C_l and C_d are sensitive for small changes in the pressure distribution over the airfoil. This would help to check the C_p variation with the number of wake panels and to fix the length of the wakes. The C_l and C_d are calculated as given below:

$$\begin{aligned} C_l &= \frac{-F_1 \cdot sin(\alpha) + F_2 \cdot cos(\alpha)}{0.5 \cdot \rho {U_0}^2 c}, \\ C_d &= \frac{F_1 \cdot cos(\alpha) + F_2 \cdot sin(\alpha)}{0.5 \cdot \rho {U_0}^2 c}, \end{aligned} \tag{4.19}$$

where, F_1 and F_2 represents the forces in axial and normal direction to the airfoil respectively. The forces used for calculating C_l and C_d are estimated from the C_p distribution on each of the panels and the panel lengths along with the unit normals in x and y directions. Figures (4.14), (4.15) and (4.16) show the C_l for airfoils VDV of 12% thickness, S820 of 16% thickness and S809 of 21% thickness respectively. There is not much variation in C_l for wake panels of 10 to 80 for all AoAs and airfoils. However, the aerodynamic coefficient increases beyond 80 wake panels as the number of panels increases. This shows that the C_l values can be changed indefinitely by changing the number of panels.

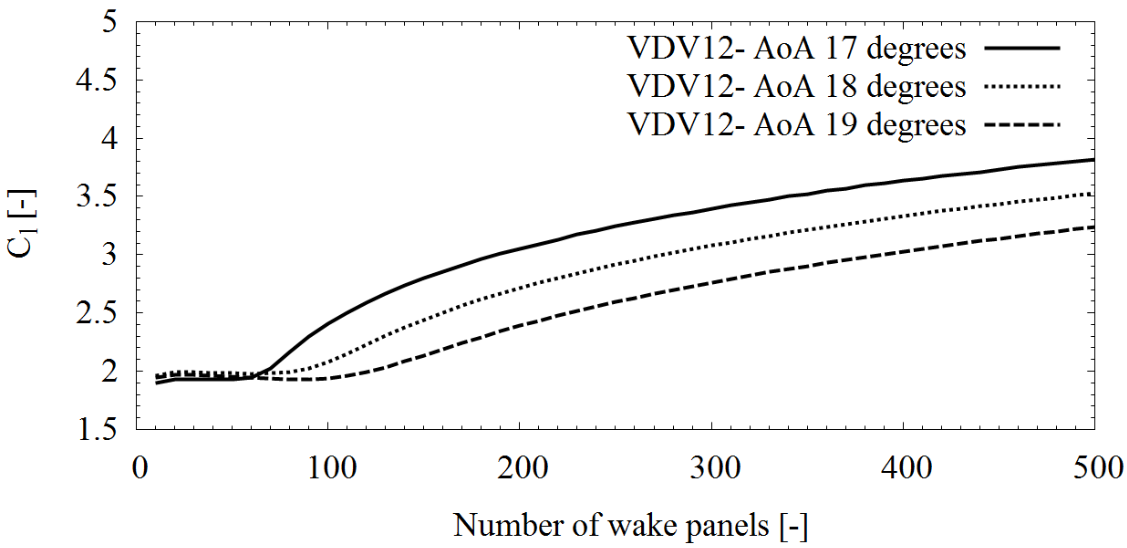

Figure 4.14: C_l obtained by inviscid double wake model at various AoA for VDV airfoil of 12% thickness.

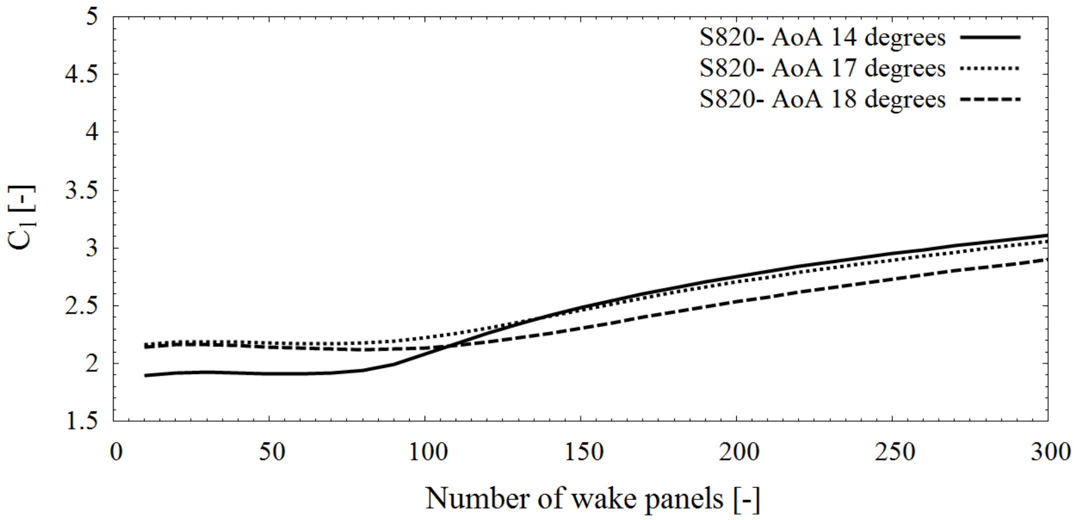

Figure 4.15: C_l obtained by inviscid double wake model at various AoA for S820 airfoil of 16% thickness.

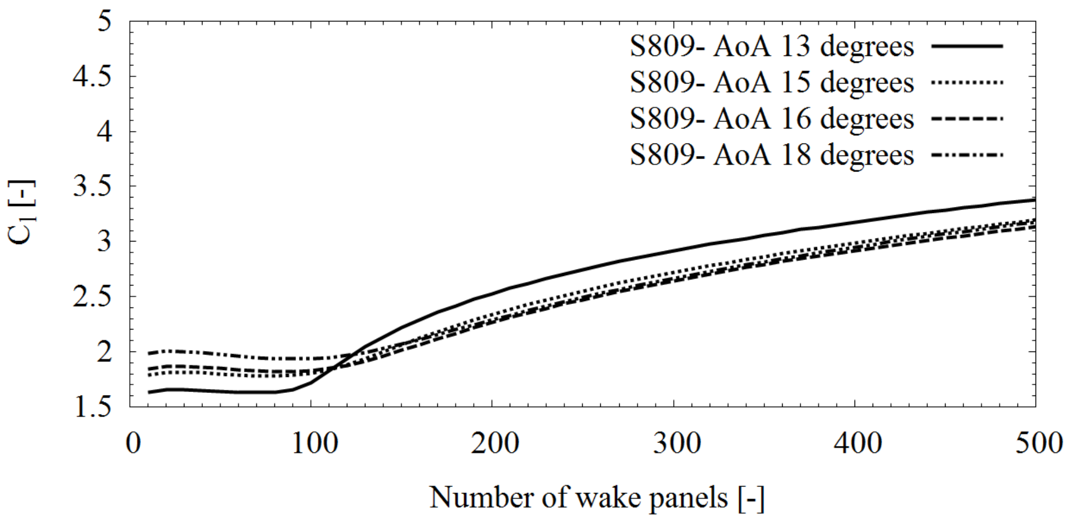

Figure 4.16: C_l obtained by inviscid double wake model at various AoA for S809 airfoil of 21% thickness.

Figures (4.17), (4.18) and (4.19) show the C_d for airfoils VDV of 12% thickness, S820 of 16% thickness and S809 of 21% thickness respectively. There is not much variation in C_d for wake panels of 10 to 80 for all AoA and airfoils. However, the aerodynamic coefficient decreases beyond 80 wake panels as the number of panels increases. This shows that the C_d values can be changed indefinitely by changing the number of panels.

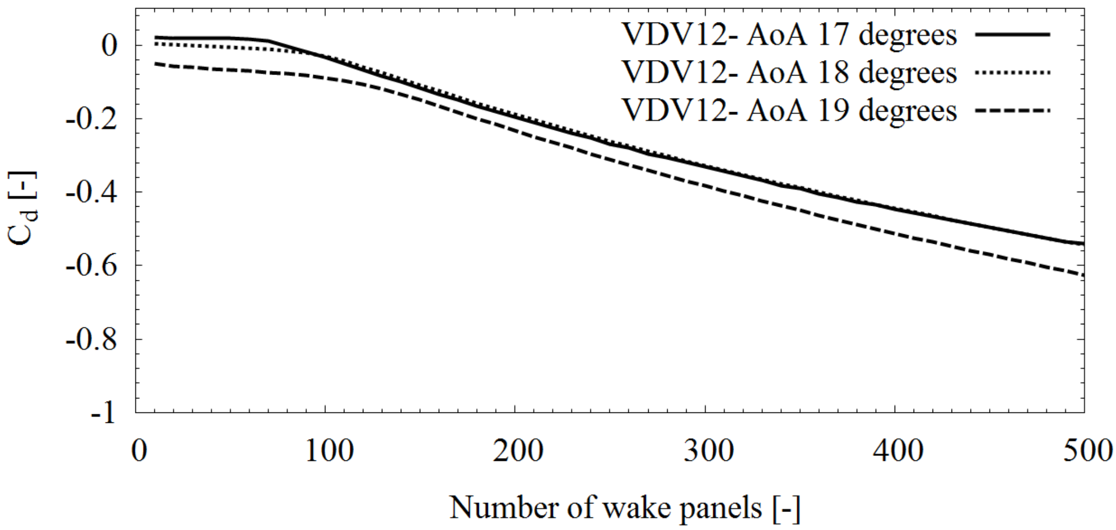

Figure 4.17: C_d obtained by inviscid double wake model at various AoA for VDV airfoil of 12% thickness.

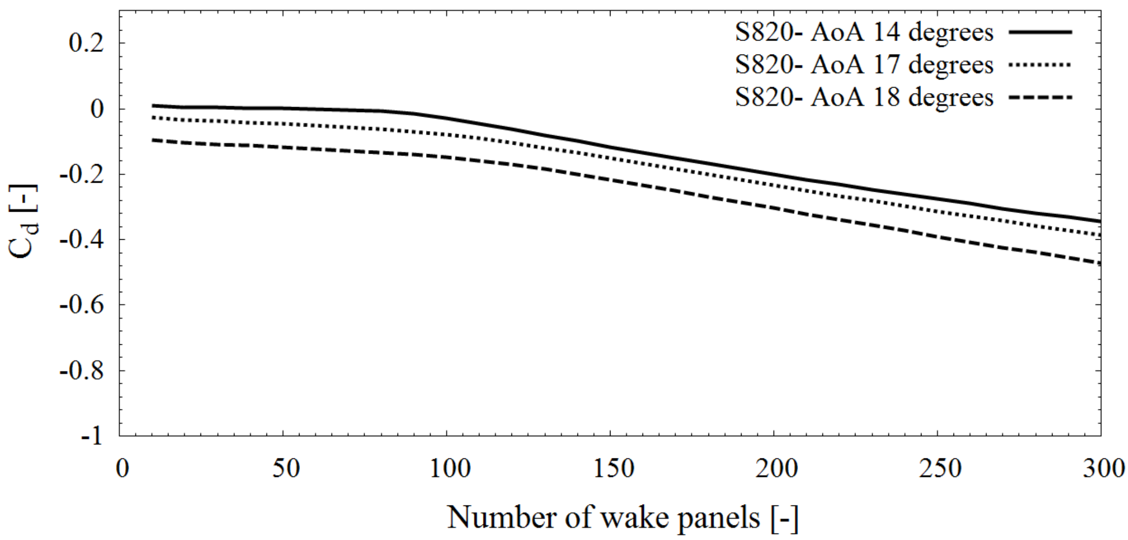

Figure 4.18: C_d obtained by inviscid double wake model at various AoA for S820 airfoil of 16% thickness.

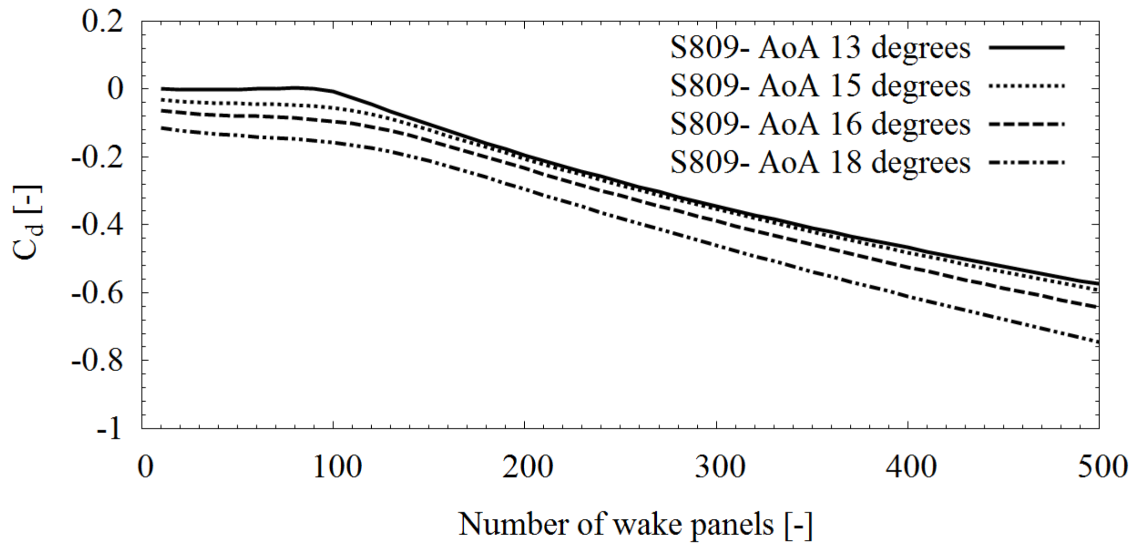

Figure 4.19: C_d obtained by inviscid double wake model at various AoA for S809 airfoil of 21% thickness.

From the above analysis, it is clear that the influence of the separation wake constant vorticity panels alone over airfoil singularity linear elements does not give an accurate representation of the separation region. Increasing the number of wake panels in the separation (second) wake only changes the C_p in turn C_l, C_d and does not actually improve the solution. Hence, different methodology is required to capture the separation phenomena accurately. Such a methodology is described in the next section.

4.2 Successful double wake implementation

The primary variable representing the flow field is velocity. However, the velocity flow field do not appear the same in all inertial frame of references. Hence, curl of the velocity i.e. vorticity, which is an invariant in any frame of reference is used to get information about the flow field around airfoil. Vorticity representation gives useful information especially when the flow separates. As described in the beginning of this chapter, vorticity is formed in the viscous region where there is a velocity gradient. Also, the vorticity is negligible in the separated flow region which can be considered as completely inviscid. The formed vorticity from the viscous layers can not be destroyed. All the formed vorticity is convected downstream in the suction side from the separation point and in the pressure side from the trailing edge of the airfoil. This convected vorticity can be modelled with the help of wake sheets emanating from the separation point and from the trailing edge with vorticity strength. Based on Kelvin's circulation theorem, in a potential flow, vortex sheet established at any instant remains the same at all instances of the time. This consequence of Kelvin's theorem is utilized to model both the wakes as constant vortex sheet and to find the solution iteratively.

To set up the vorticity strength on the wake, the initial wake shapes are required. The initial wake shapes are determined as streamlines from the induced velocities as a result of linear vortex singularity elements distribution over airfoil surface panels. Therefore, wake shapes based on predetermined shape as described by Dvorak et al. [18] and wake factor from the work of Marion et al. [5] are avoided. In the previous established methods, the initial wake shapes used for the iterative solution procedure, intersect at a point downstream. This is not the case in the present implementation as the wake shapes determine the outer edge of the separation region where the streamlines do not interesect and becomes parallel farther in the downstream region. This is illustrated in the Figure (4.20) by a computational fluid dynamics simulation performed by Stanford University Unstructured (an open source CFD solver) (SU2) [19], for FFA-W3-301 airfoil at 16° AoA and Reynolds number of $1.6 \cdot 10^6$.

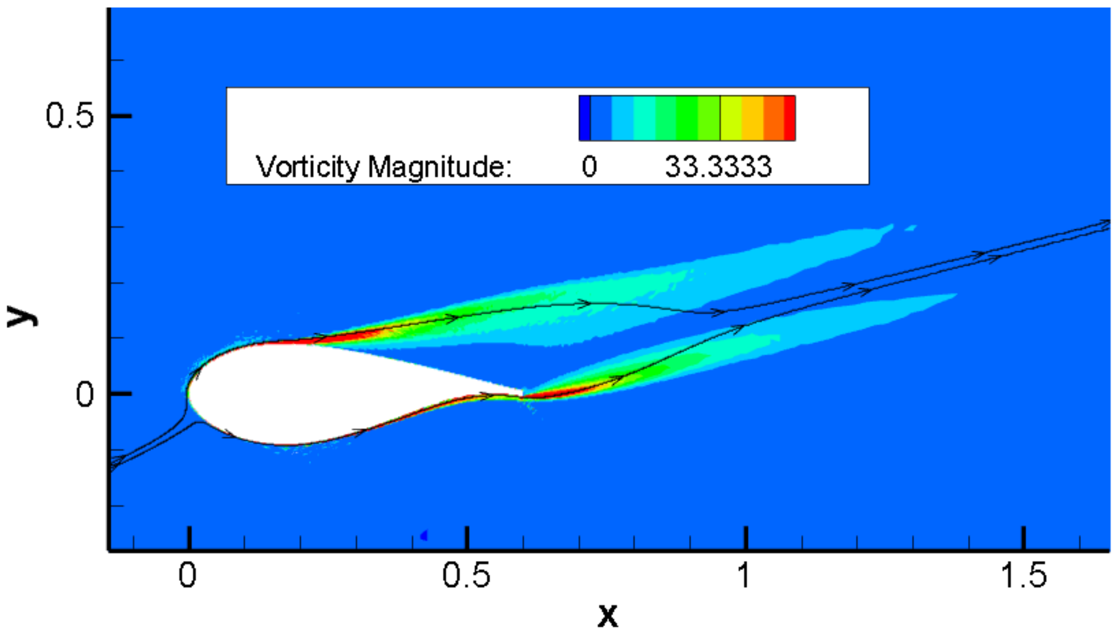

Figure 4.20: Vorticity distribution over FFAW3301 30% thick airfoil with streamlines enclosing the separated flow region (obtained from numerical simulation).

The given external separation point is moved to the closest panel end point for the initial wake shape calculation. This is due to the fact that there can be only $N + 1$ unknowns with N Neumann boundary conditions and one Kutta condition. Also the panel size is very small of the order of 10^{-2} and so the change in separation point is very small when moved to the panel edge. The linear vortex distribution over airfoil surface is the same as discussed for the single wake model in section (3.1) and is shown in Figure (3.2). This formulation is used for conventional sharp trailing edge airfoils. For thick trailing edge airfoils, the same formulation is used without any panel on the trailing edge. Figure (4.21) depicts the formulation for thick trailing edge airfoils, used to find the initial wake shapes.

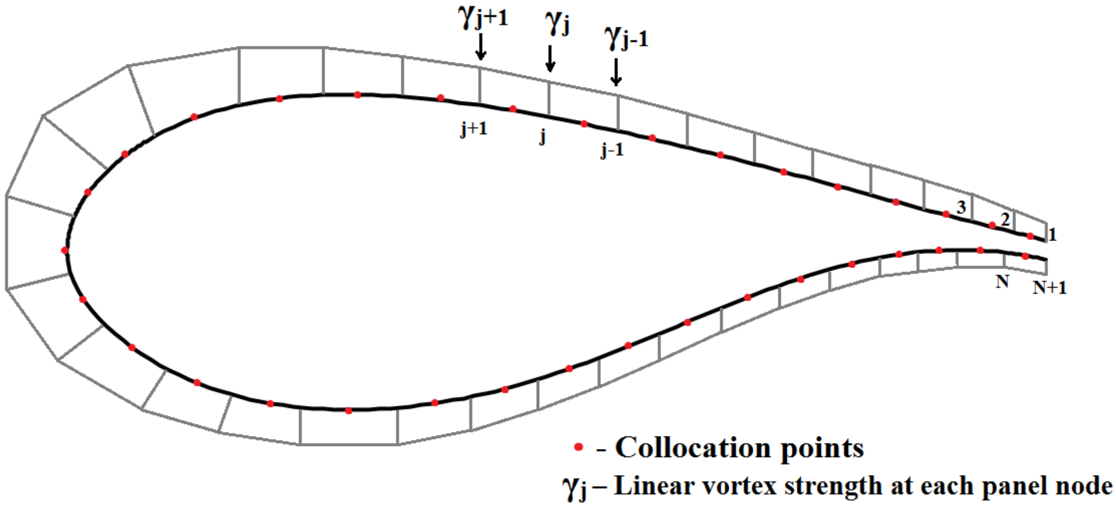

Figure 4.21: A sketch of linear vortex strength distribution on airfoil surface with blunt trailing edge used for initial wake shapes calculation.

The Kutta condition is changed from the single wake model, to adapt the constant pressure distribution in the separated region. It is given by the following equations based on positive or negative AoA respectively

$$\begin{aligned} \gamma_{N+1} + \gamma_{SEP} &= 0, \\ \gamma_1 &= 0, \end{aligned} \tag{4.20}$$

$$\begin{aligned} \gamma_1 + \gamma_{SEP} &= 0, \\ \gamma_{N+1} &= 0, \end{aligned} \tag{4.21}$$

where γ_1, γ_{N+1} are the vorticities at the trailing edge and γ_{SEP} is the vorticty at the separation point. This condition ensures that the vorticity at the separation point is opposite to that at the trailing edge. Both the wake shapes are calculated in a similar manner. The wakes at the trailing edge and the separation point are built with panels of increasing size using cosine distribution. This is because smaller number of increasing size panels is sufficient to obtain the correct shape, compared to constant size panels. The total velocity at any point is calculated as the sum of freestream velocity and induced velocity from all the vorticities on airfoil surfaces as,

$$\vec{U} = \vec{U}_0 + \vec{U}_{\gamma_{airfoil}}, \tag{4.22}$$

where $\vec{U}$ represents the total velocity. Similar to the airfoil surface panels, the collocation points on the wake panels ia also considered to be at the midpoint of the respective panels. The collocation point for the first panel of the wakes is taken just outside the respective airfoil surface panel edges in the x-direction. Based on the normal and tangential local velocities at the collocation point, the orientation of the first panel of the wake is calculated by iterative procedure, for its shape till the difference in the angle between subsequent iterations becomes the order of 10^{-4} tolerance. Then the second collocation point is chosen at the same angle as the previous converged panel. Again several iterations were carried out to reach the same level of convergence as the first panel. The same procedure is followed for all the remaining panels in the wake to get the resultant converged initial wakes shape with all the chosen panels. The length of the wake is determined based on the number of panels used.

For subsequent iterations after establishing the initial wake shape, the separation point is forced to be away from the panel edges and the collocation points. The separation point is moved to avoid removing an equation from the system (i.e. to avoid a system with one less unknown) and avoid singularities of solution scheme. The separation point is moved to one quarter of the panel length from the closest panel end point. The solution is also not affected as the separation point is moved only to a very small distance and the panel size is also very small. A representation of the vorticity distribution for subsequent iterations is shown in Figure (4.22). Sharp trailing edge airfoil with positive AoA is used for representation.

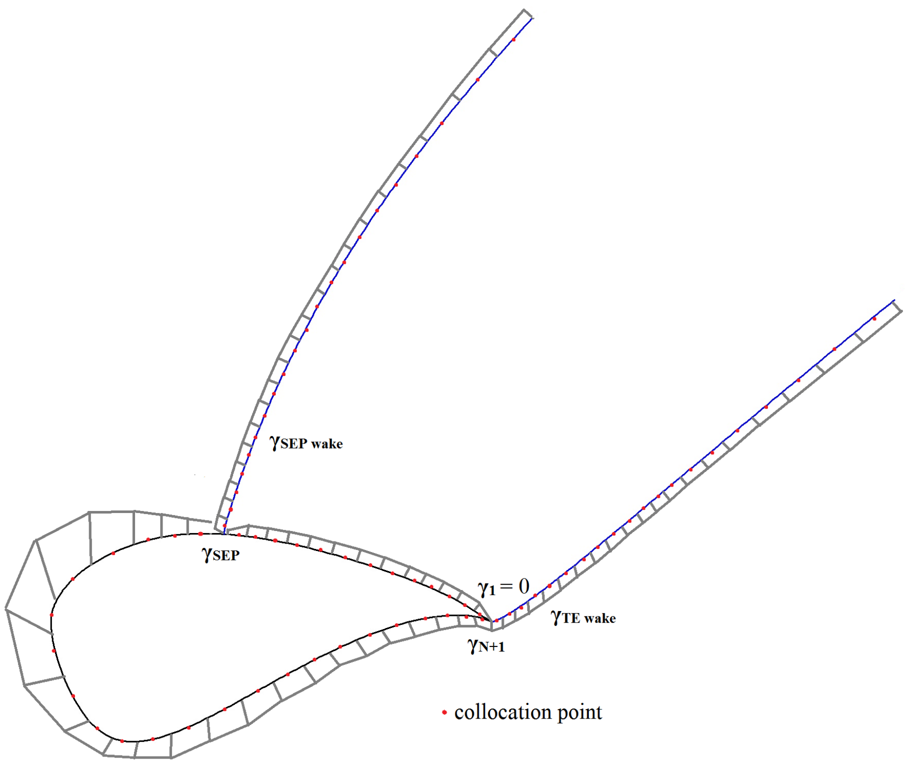

Figure 4.22: A sketch of the vorticity distribution on the airfoil surface and the wakes after establishing the initial wake shapes.

The local vorticity at the trailing edge along the side of separation point is made zero to accommodate the Kutta condition and to convect the wake towards the side of separation. Moreover, the induced velocity contribution of the panel with the separation point at the immediate downstream is made zero. This is done to make the local vorticity downstream the separation point negligible and to convect the wake from the separation point downstream, as shown in Figure (4.23).

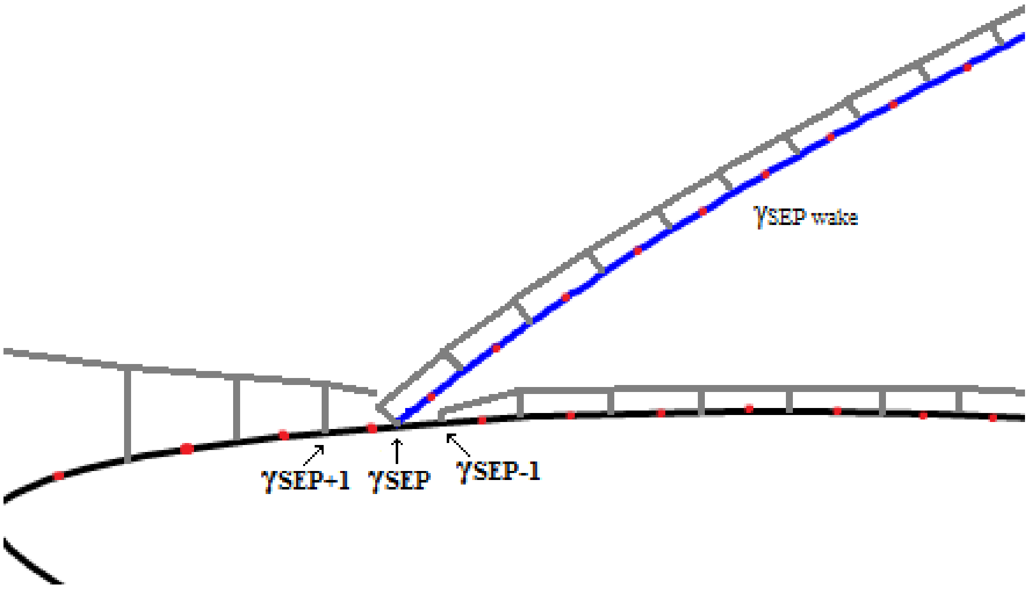

Figure 4.23: A sketch of the vorticity distribution at the separation point along with the separation point wake (blue line).

The solution is obtained by applying vorticity of constant strength on the wake panels. The strength of the vortices on the wake is given by,

$$\gamma_{SEP} = \gamma_{SEP_{wake}}, \tag{4.23}$$

$$\gamma_{N+1} = \gamma_{TE_{wake}}, \tag{4.24}$$

where, $\gamma_{SEP_{wake}}$ and $\gamma_{TE_{wake}}$ represent the vorticity distribution along the secondary and trailing edge wake respectively. The formed wake sheets are used in subsequent iterations to impact the vorticity distribution on the airfoil surface thereby control the vorticity production. The vorticity strengths on the airfoil and wake panels can be iteratively calculated with the Neuman boundary condition on the collocation points including the vorticity strength of the wake sheet:

$$\sum_{j=1}^{N+1} A_{li,j}\,\gamma_j + \sum_{j=N+2}^{N+Nw+1} A_{ci,j}\,\gamma_j + \sum_{j=N+Nw+2}^{N+2Nw+1} A_{ci,j}\,\gamma_j + (\vec{U}_0.n_i) = 0, \quad \text{for } i = 1 \text{ to } N, \tag{4.25}$$

where Nw is the number of wake panels. The influence coefficient matrices $A_{l_{i,j}}$ and $A_{c_{i,j}}$ contain the induced velocities from linear vortex singularity elements on airfoil surface and constant vortex singularity elements on both the wakes respectively and is given by,

$$\begin{aligned} A_{l_{i,j}} &= u_{i,j}.n_i, \\ A_{c_{i,j}} &= u_{c_{i,j}}.n_i. \end{aligned} \tag{4.26}$$

The induced velocities in the influence coefficient matrix due to linear vortex strength element located on airfoil surface panels, is given by,

$$u_{i,j}, w_{i,j} = (U_{al}, W_{al})_{i,j} + (U_{bl}, W_{bl})_{i,j-1}, \tag{4.27}$$

where, i is the collocation point and j represents panel end points. Only the induced velocity contribution of the panel with the separation point at the immediate downstream is made zero. Hence, the induced velocity at immediate downstream is,

$$u_{i,SEP-1}, w_{i,SEP-1} = (U_{bl}, W_{bl})_{i,SEP-2}. \tag{4.28}$$

As a result local vorticity downstream the separation point γ_{SEP-1} becomes negligible and this helps to convect the wake from the separation point downstream. This can be seen in the Figure (4.23). The induced velocities due to constant vortex strength element on the wakes is,

$$u_{c_{i,j}}, w_{c_{i,j}} = (U_{ac}, W_{ac})_{i,j}. \tag{4.29}$$

The calculation of induced velocities as a result of linear vortex singularity elements on the airfoil surface is described in section (3.1). The induced velocities as a result of constant vortex element in the wake panel is calculated in the panel coordinates as in Katz and Plotkin [6] and is given by,

$$\begin{aligned} U_1 &= \frac{t_2 - t_1}{2\pi}, \\ W_1 &= -\frac{log\frac{d1}{d2}}{2\pi}. \end{aligned} \tag{4.30}$$

where, d_1 and d_2 represent the distance between the collocation point and the end points of each panel. t_1 and t_2 are the angles corresponding to d_1 and d_2 respectively. These variables are given in panel coordinates. Hence, the calculated induced velocities are transformed back to the global coordinates. They contribute to the aerodynamic influence coefficients and given by,

$$\begin{aligned} U_{ac} &= -U_1\, cos(\alpha_j) - W_1\, sin(\alpha_j), \\ W_{ac} &= -U_1\, sin(\alpha_j) + W_1\, cos(\alpha_j). \end{aligned} \tag{4.31}$$

The convected vorticity along the wakes from the trailing edge and the separation point changes its direction and the value based on the airfoil surface vorticity which in turn influences the vorticity distribution on the airfoil. The total velocity at any point in the flow field is estimated considering the contribution of freestream velocity and those induced from vorticity located on the airfoil surface and on both the wakes:

$$\vec{U} = \vec{U}_0 + \vec{U}_{\gamma_{airfoil}} + \vec{U}_{\gamma_{SEP_{wake}}} + \vec{U}_{\gamma_{TE_{wake}}}. \tag{4.32}$$

The wake shape is recalculated for subsequent iterations based on freestream velocity and induced velocities from airfoil and wake vorticities as given by equation (4.32). The panels orientation is calculated similar to that of the initial wake shape. The near wake panel of the initially formed wake from separation point is at very high angle with respect to the airfoil. This means the flow does not leave the airfoil surface smoothly. The solution is iterated with the trailing edge wake and separation wake vorticity influence over airfoil vorticity distribution until the near wake panels from the separation point leaves the airfoil surface smoothly. The orientation of the near wake panels is determined based on the contribution of all the linear singularity elements on the airfoil surface. The influence of the airfoil panels closer to the wake panels have higher influence in deciding the orientation of the wake panel, next only to the freestream velocity component. For separation wake, the influence of the airfoil panels before and after separation is more than the remaining panels. Similarly, for the trailing edge wake, the influence of the airfoil panels at the trailing edge is more than the remaining panels. When the influence of the neighbouring airfoil panels on the respective wake panels decreases and reaches the influence as that of the remaining airfoil panels, it is considered as far wake. Further, the accuracy of the solution obtained depends on the chosen number of wake panels and in turn the wake length. The number of wake panels for the following analysis is fixed to be 500, higher than the number for which no influence of the wake panels on the final solution is registered. The choice of 500 panels is justified in the next section (4.2.1). The obtained initial wake and the final wake after convergence, from separation point and trailing edge is shown in Figure (4.24) for NACA63415 airfoil at an AoA of 16° and Reynolds number of 160 000. The same is shown in Figure (4.25) representing near wake region of the initial and the final wake.

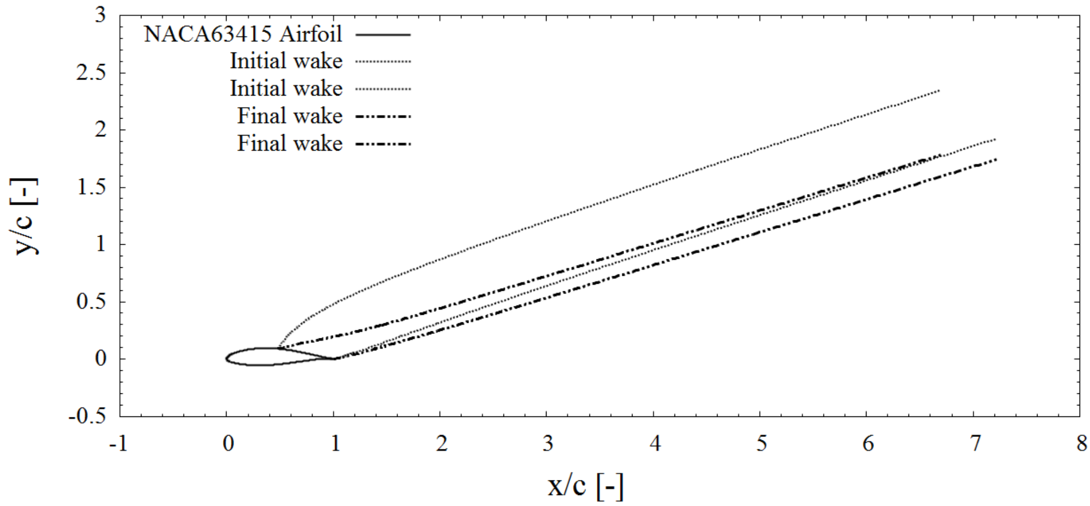

Figure 4.24: Initial and final wake shapes of NACA63415 airfoil.

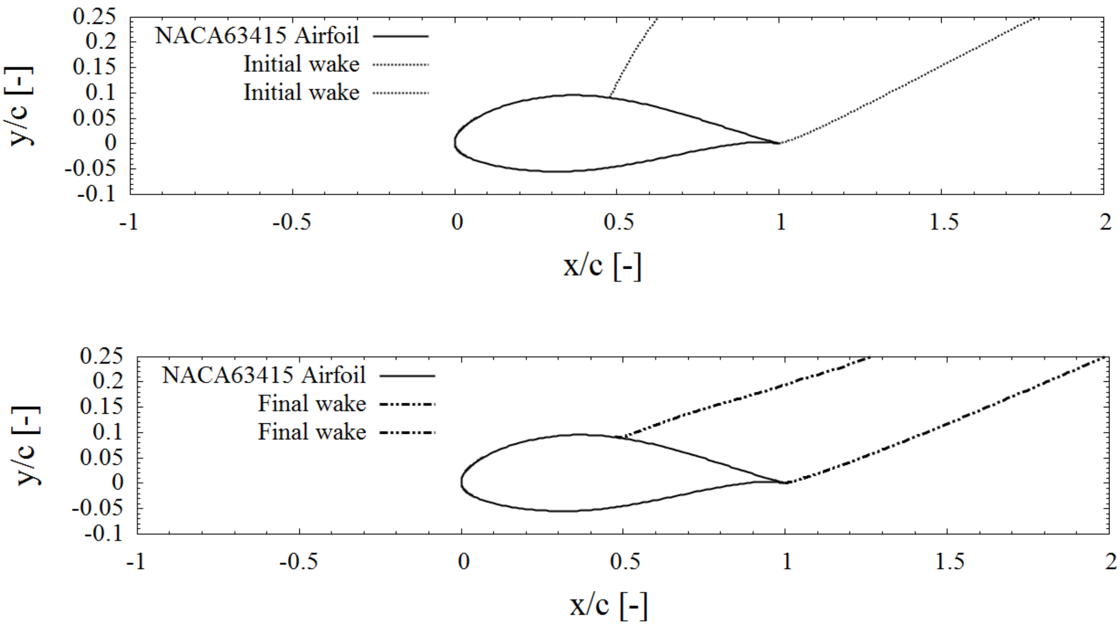

Figure 4.25: A zoom-in to the initial (top) and final wake shapes of NACA63415 airfoil.

4.2.1 Optimum wake length to obtain accurate results

As described previously, the wake lengths influence the accuracy of obtained double wake result. The wake from the separation point and the trailing edge are formed with several panels distributed using cosine function. The usage of increasing size panels can be justified from section (3.3) which compares the results of increasing sized and constant sized panels. The smaller size panels are used in the near wake region i.e. in the region closer to the separation point and the trailing edge, so that the near wake influence can be captured more effectively.

The C_p distrubtions for different number of panels at different AoAs for various airfoils need to be studied to determine the optimum length of the wake. However, the C_p gives the pressure distribution around the entire airfoil and so it is difficult to conclude the number of wake panels required. Therefore, a single valued entity namely C_l and C_d are used. Also, the C_l and C_d are very sensitive for changes in the pressure distribution over the airfoil. Figures (4.26), (4.27) and (4.28) show the plot of C_l for airfoils VDV of 12% thickness, S820 of 16% thickness and S821 of 24% thickness respectively at various AoAs. It can be seen that the C_l decreases with increasing number of panels and the variation becomes of the order of $1 \cdot 10^{-3}$ beyond 200 to 300 panels for all the airfoils studied.

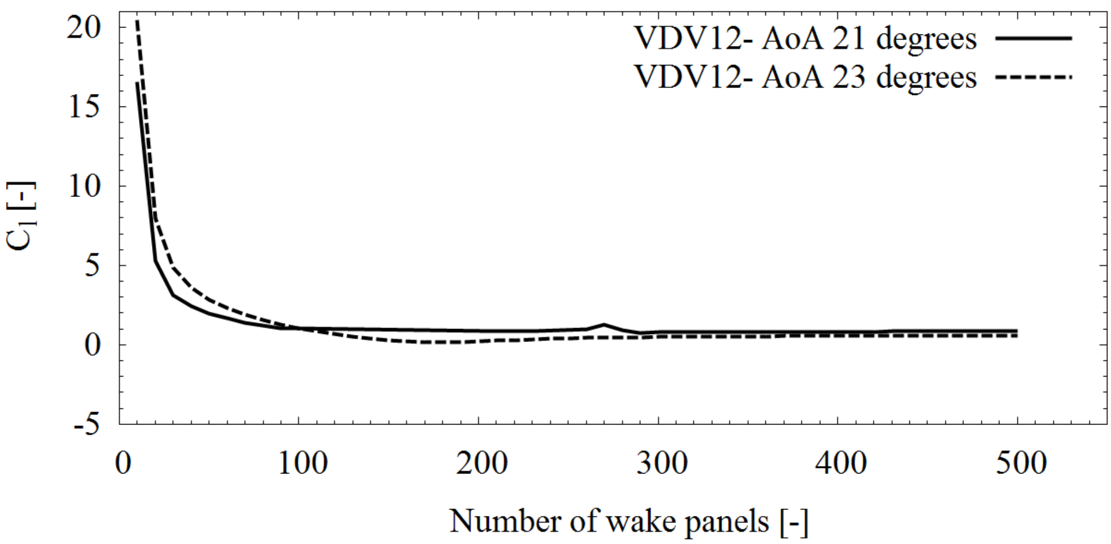

Figure 4.26: C_l obtained by inviscid double wake model at various AoA for VDV airfoil of 12% thickness.

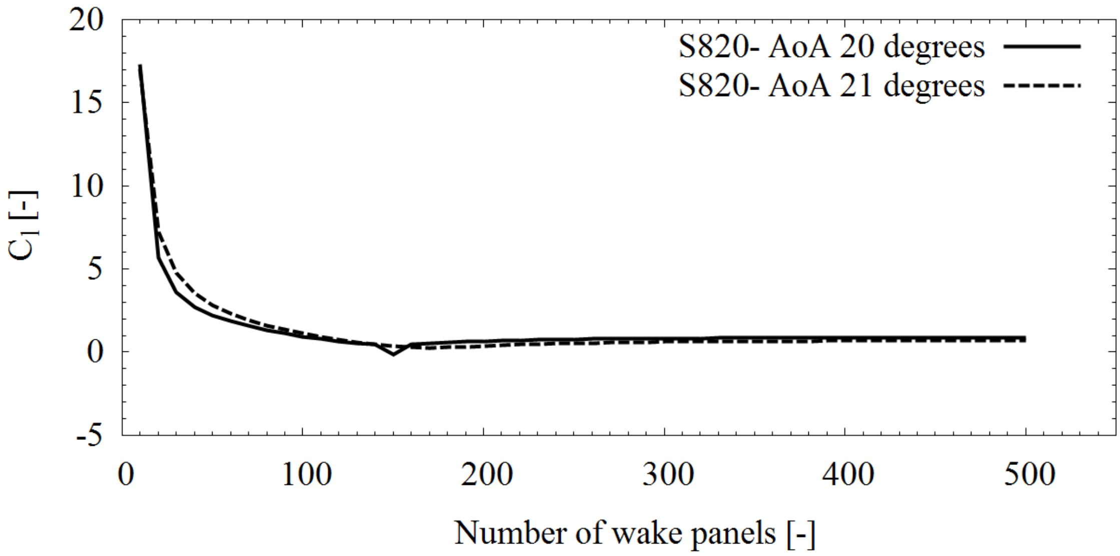

Figure 4.27: C_l obtained by inviscid double wake model at various AoA for S820 airfoil of 16% thickness.

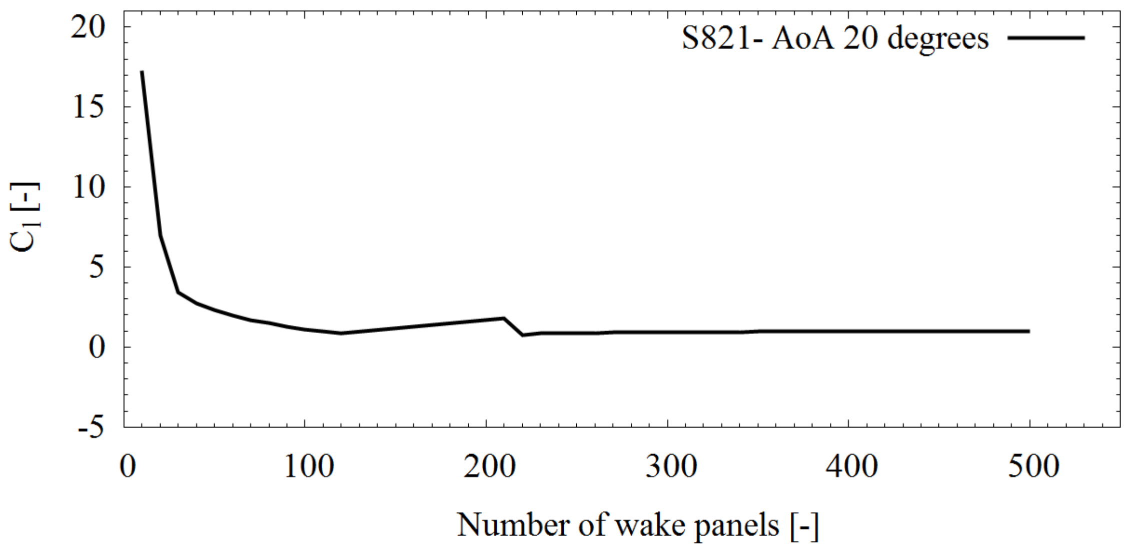

Figure 4.28: C_l obtained by inviscid double wake model at 20° AoA for S821 airfoil of 24% thickness.

Similarly, Figures (4.29), (4.30) and (4.31) shows the plot of C_d for VDV, S820 and S821 airfoils respectively of different thickness at various AoAs. It can be seen that the C_d also decreases with increasing number of panels and the variation becomes of the order of $1 \cdot 10^{-3}$ beyond 200 to 300 panels for all the airfoils studied.

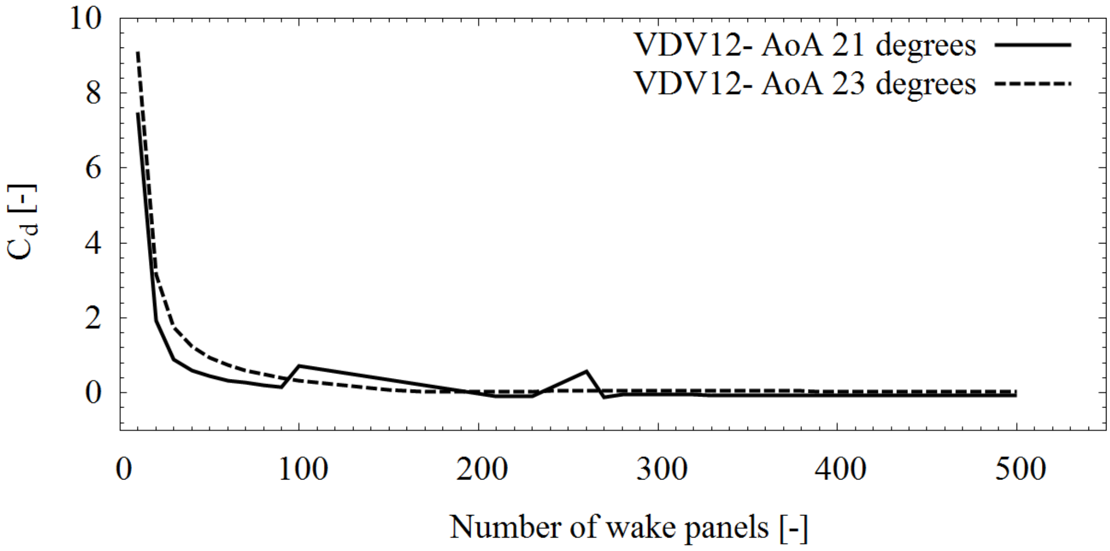

Figure 4.29: C_d obtained by inviscid double wake model at various AoA for VDV airfoil of 12% thickness.

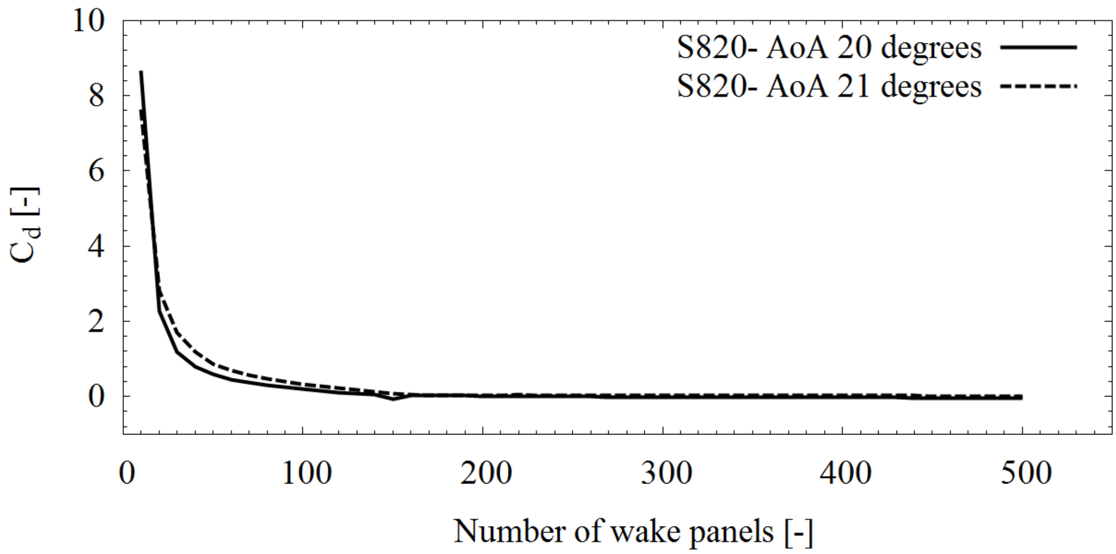

Figure 4.30: C_d obtained by inviscid double wake model at various AoA for S820 airfoil of 16% thickness.

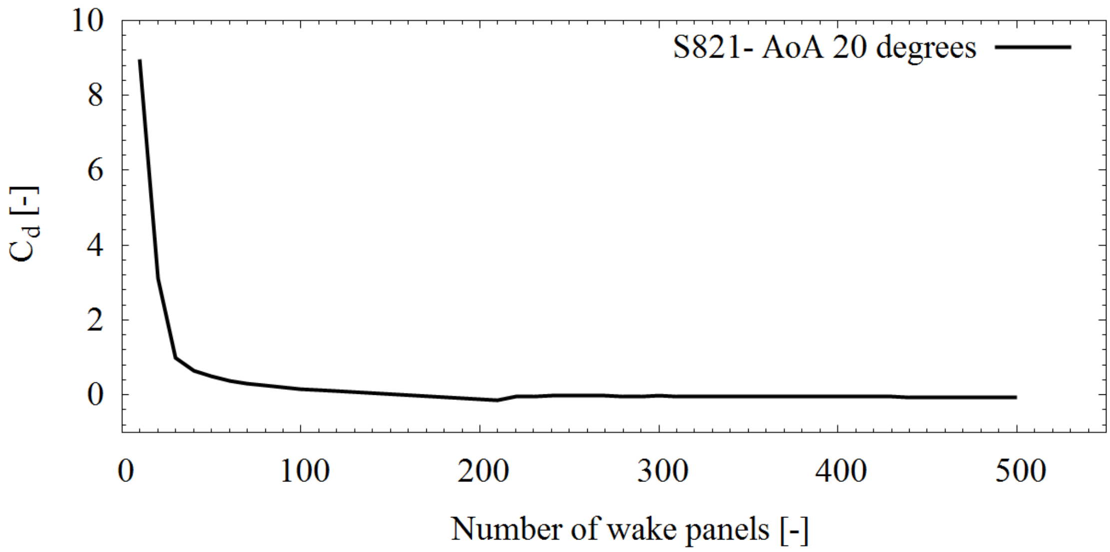

Figure 4.31: C_d obtained by inviscid double wake model at 20° AoA for S821 airfoil of 24% thickness.

Hence, after this analysis considering the influence of number of wake panels on to the C_l and C_d values, the number of panels is fixed to be 500 for the simulation of double wake inviscid model irrespective of the angle of attack and the airfoil used.

4.2.2 Pressure coefficient

The flow inside the airfoil is stagnant and so the tangential velocity is given by the airfoil surface vorticity, in the absence of source terms as described by Drela [8]. The inviscid pressure coefficient distribution can be calculated from the known vorticity distribution from the airfoil surface and is given by

$$C_p = 1 - \frac{\gamma_j^2}{{U_0}^2}. \tag{4.33}$$

Due to flow separation, there is a jump in total pressure accross the separation wake streamline from the non-separated flow region. The C_p in separated flow region is estimated by considering the modified pressure distribution as described by Dvorak et al. [18]:

$$C_p = 1 - \frac{\gamma_j^2}{{U_0}^2} + \frac{\Delta h}{0.5\,\rho\,{U_0}^2}. \tag{4.34}$$

Using Bernouilli's theorem, the total pressure jump in the separation region can be described as follows

$$\Delta h = P_{SEP^-} + \frac{\rho}{2}\,U_{SEP^-}^2 - P_{SEP^+} - \frac{\rho}{2}\,U_{SEP^+}^2, \tag{4.35}$$

where P_{SEP^+}, P_{SEP^-} are the local pressures before and after the separation point respectively. Similarly, U_{SEP^+}, U_{SEP^-} are the local velocities before and after the separation point respectively. The wake is a streamline so that there is no static pressure drop across the convected shear layer from the separation point. The total pressure jump across the secondary wake at separation point can be given by

$$\Delta h = \frac{\rho}{2}\,U_{SEP^-}^2 - \frac{\rho}{2}\,U_{SEP^+}^2. \tag{4.36}$$

Also, the local vorticity at the separation point is the difference in local velocities before and after the separation. According to Rioziotis [3] the local velocity after separation is zero which leads to

$$\gamma_{SEP} = U_{SEP^+}. \tag{4.37}$$

Hence, the total pressure jump in the separation region is given as follows

$$\Delta h = -\rho\,\frac{{\gamma_{SEP}}^2}{2}. \tag{4.38}$$

This total pressure jump is the correction added to the C_p calculated from the inviscid double wake model only in the separated flow region i.e. the region between the two wakes on the side of the separation. Outside the separated flow region, this correction is not applicable and hence its contribution is neglected.

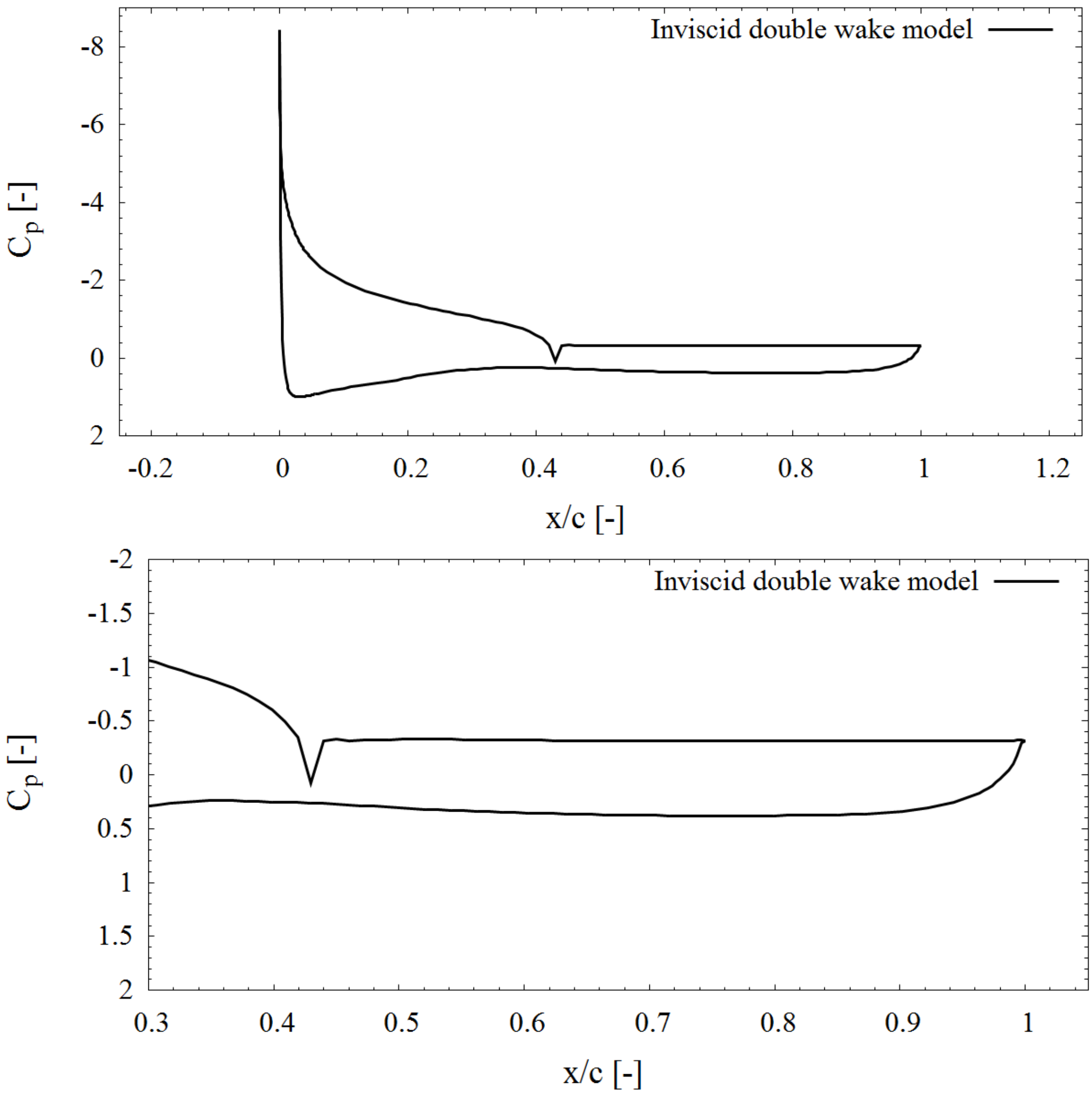

Figure 4.32: Pressure coefficient by inviscid double wake model for S826 airfoil at $Re = 100\,000$ and at AoA of 14.5° (top) and a zoom in to the separation region.

Figure (4.32) shows the plot of C_p by inviscid double wake method using 300 airfoil surface panels and 500 wake panels. The separation point is located at $x/c = 0.43$ and is obtained from the experimental data [20, 21]. A constant pressure distribution in the separation region on airfoil surface is registered. The accuracy of the inviscid double wake model's solution is validated using different airfoils with the experimental and numerical results and shown in the numerical results chapter (5).

Chapter 5

Numerical results

The results are shown using an inviscid double wake model developed to evaluate the robustness of the double wake approach. For the analysis, the separation point is taken externally from the experimental data whereever it is available otherwise the separation point is taken from the method to which the double wake model is compared. When the successful double wake model is implemented in RFOIL, the separation point would be taken from the first iteration solution of the tool.

Four airfoils namely S826, NACA63415, S825 and FFA-W3-301 are considered in the analysis. The airfoils are shown in the Figure (5.1).

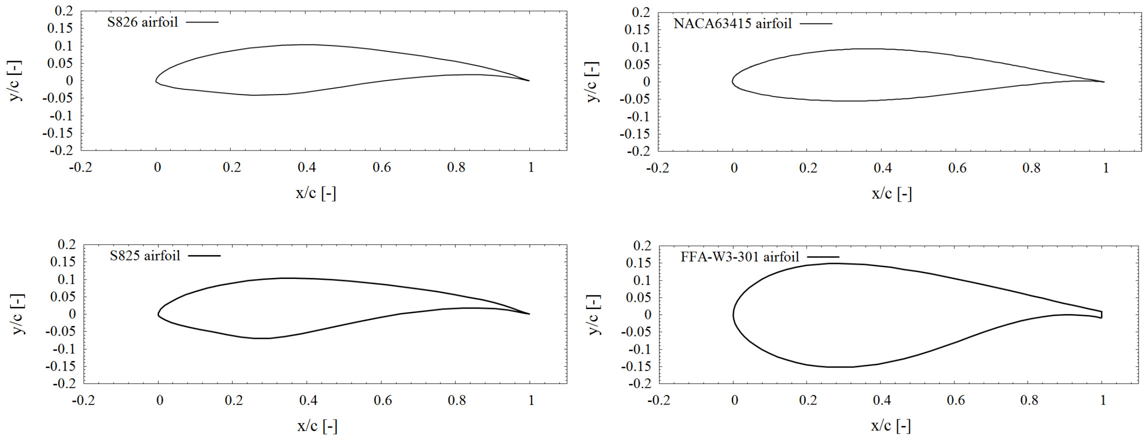

Figure 5.1: Airfoil sections used for the analysis.

In section (5.2), the pressure distribution obtained by the successful inviscid double wake method is compared with the experimental data [20, 21, 22] and the numerical results obtained by CFD (SU2) and XFOIL for S826 and NACA63415 airfoils.

FFA-W3-301 airfoil is used to show the result of blunt trailing edge airfoil from inviscid double wake model along with the experiment [23] and XFOIL results and presented in section (5.3). In section (5.4), S825 airfoil is used to show the result of inviscid double wake model in comparison to the experiment [24] at two different angles of attacks near post stall, for a chosen Reynolds number.

5.1 Test cases explained

The airfoils NACA63415 and S826 are used for numerical simulation by CFD (SU2). As experimental results are available for S826 airfoil at Reynolds number of 100 000 and AoA of 14.5° and for NACA63415 airfoil at Reynolds number of 160 000 and AoA of 16°, numerical simulation is also carried out at the same parameters. The neccessity of numerical simulation is to check the validity of the numerical result with the available experimental data. At very high AoAs where experimental data are not available, it would enable to compare the CFD numerical results with double wake inviscid results. The CFD numerical analysis is done using SU2 [19]. In SU2, the BC transition model along with Spalart Allmaras (SA) turbulence model is available and it is used for the validation purpose. It requires meshing of flow field around the airfoil followed by mesh convergence study to obtain mesh independent solution and to determine accurate numerical solution for comparison with double wake inviscid model results.

5.1.1 Mesh generation for CFD simulation

As both the airfoils used, have sharp trailing edges, 2D unstructured C-mesh is used for discretising the flow field around the airfoil. Here, the element choice is quadrilateral. The turbulent flow is associated with thin boundary layer in which the viscous effects can not be neglected. To capture the effect fully, the mesh needs to be refined near the wall of the airfoil. This can be done in two ways.

1. Wall function approach
   This empirical approach is mainly deviced to capture the flow pattern without having to generate very fine mesh near the wall. This method is economical and empirically based on high-Reynolds number flows. So it gives poor prediction of low-Reynolds number effects.

2. Two-layer zonal approach
   This approach uses mesh refinement in the near wall region. The flow variables

are calculated explicitly and there is no dependence on empirical wall funcions in this method. Hence, this method is used here for constructing the mesh for numerical analysis. The boundary layer is refined with $y+ = 1$. The wall spacing Δs is calculated based on the following relation, [25]

$$\Delta s = \frac{y^+ \nu}{\rho u^*}, \tag{5.1}$$

where ρ is the density of air, μ is the dynamic viscosity and u^* is the friction velocity. The density and dynamic viscosity are taken at the conditions of standard temperature and pressure. The friction velocity is given by

$$u^* = \sqrt{\frac{\tau_w}{\rho}}, \tag{5.2}$$

where,

$$\tau_w = 0.5\, C_f\, \rho\, U_0^2, \tag{5.3}$$

$$C_f = 0.0576\, Re_x^{-1/5} \quad \text{for } 5 \cdot 10^5 < Re_x < 10^7. \tag{5.4}$$

For the S826 and NACA63415 airfoils at the chosen Reynolds number, with $y+ = 1$ the wall spacing Δs is calculated to be $1.9 \cdot 10^{-4}$ and $1.3 \cdot 10^{-4}$ respectively. The wall spacing is taken to be the initial cell thickness from the airfoil surface at the boundary layer. The far field is fixed at 90 times the chord length to capture the complete effect of flow variables. The leading and trailing edge of the airfoils are discretised with very fine mesh refinement, shown in Figure (5.2), as the gradients of the flow variable are very high in these regions. This facilitates the accurate flow variables calculation at the high curvature leading edge and smooth gradient transformation at the trailing edge. The angular skewness of the mesh cells is kept under 0.5 and the area ratio between the cells around a maximum of 1.2. The aspect ratio which is the ratio of length to width is kept under 4000. The larger values of the skewness, area ratio and the aspect ratio than prescribed leads to convergence problem and bad interpretation of the result. Figure (5.3) shows the C-mesh generated for NACA63415 airfoil as per the above mentioned parameters.

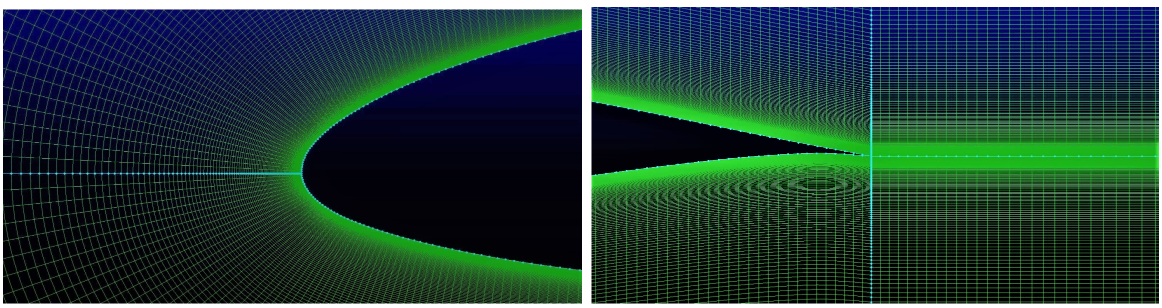

Figure 5.2: Mesh refinement at the leading and the trailing edge of NACA63415 airfoil.

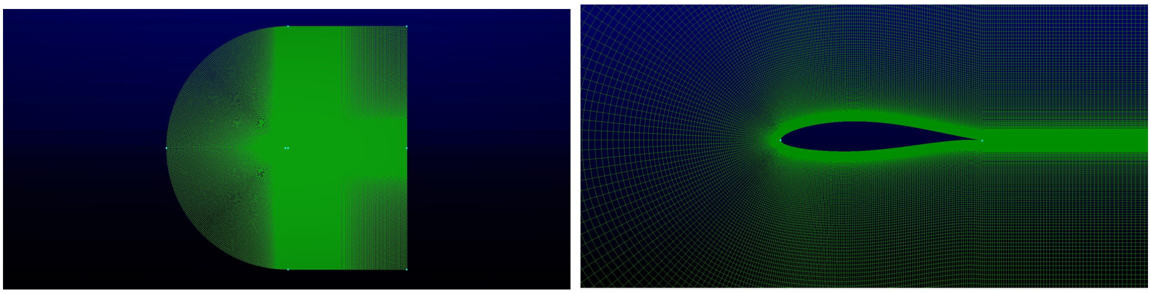

Figure 5.3: NACA63415 airfoil C-mesh.

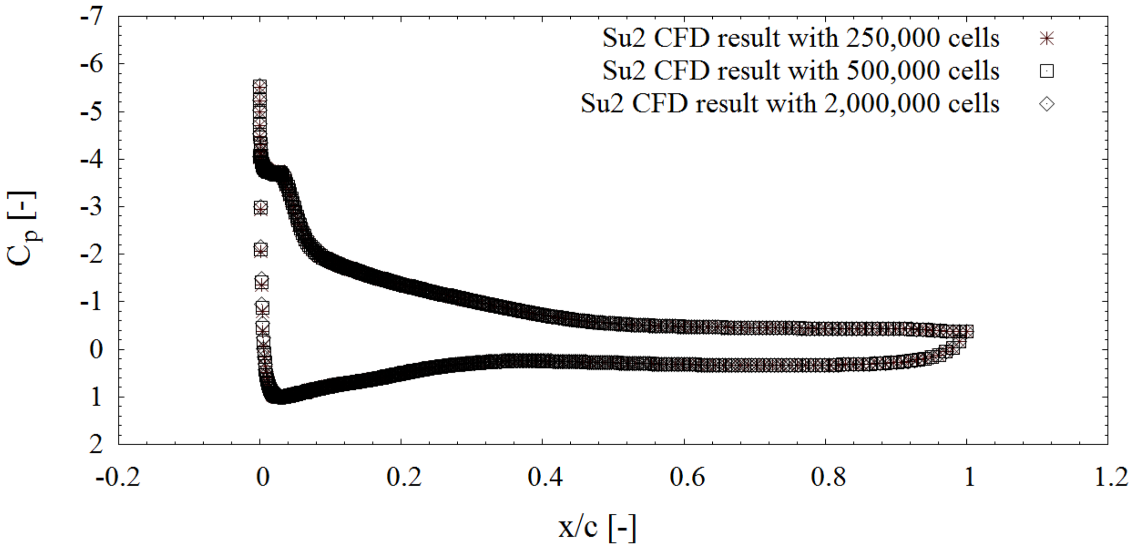

Figure 5.4: Numerical results using SU2 for S826 airfoil at $Re = 100\,000$ and at AoA of 14.5°.

For S826 airfoil, C-mesh is generated by using the above mentioned parameters. Three different meshes with 250 000, 500 000 and 2 000 000 cells are studied to determine the mesh independent solution. Figure (5.4) shows the C_p plot for S826 airfoil at Reynolds number of 100 000 and at angle of attack of 14.5° for the above mentioned meshes. As the solution (i.e. C_p distribution) remains the same for the chosen three different meshes, the obtained solution is mesh independent and the coarser of the meshes with 250 000 cells is chosen for comparison with the double wake inviscid model. Similarly, for NACA63415 airfoil, four different meshes with 250 000, 440 000, 700 000 and 1 500 000 cells are studied at Reynolds number of 160 000 and at angle of attack of 16°. All the meshes except the mesh with 250 000 cells gives mesh independent solutions. Based on this analysis, the mesh with 440 000 cells is chosen for comparison with double wake inviscid model.

5.2 Validation cases with sharp trailing edge airfoils

Figure (5.5) shows the comparison of pressure coefficients with the current inviscid double wake model, XFOIL, CFD and experimental data [20, 21] for S826 airfoil at Reynolds number of 100 000 and at angle of attack of 14.5°. The separation point for the inviscid double wake method is located at $x/c = 0.43$ and is obtained from experimental data. It can be seen that the inviscid double wake method can replicate result closer to that of experiment and better than the numerical viscous solution of XFOIL, in the separated flow region. However, it has to be considered that feeding the separation point from experiment gives added advantage to the inviscid double wake model. The peak suction pressure from the inviscid double wake method is largely over-predicted. It has to be noted that the inviscid double wake model has the disadvanatge of not having viscous effects. Further, the release of wake from separation point gives a small oscillation at the separation point. These can be seen from the Figure (5.6).

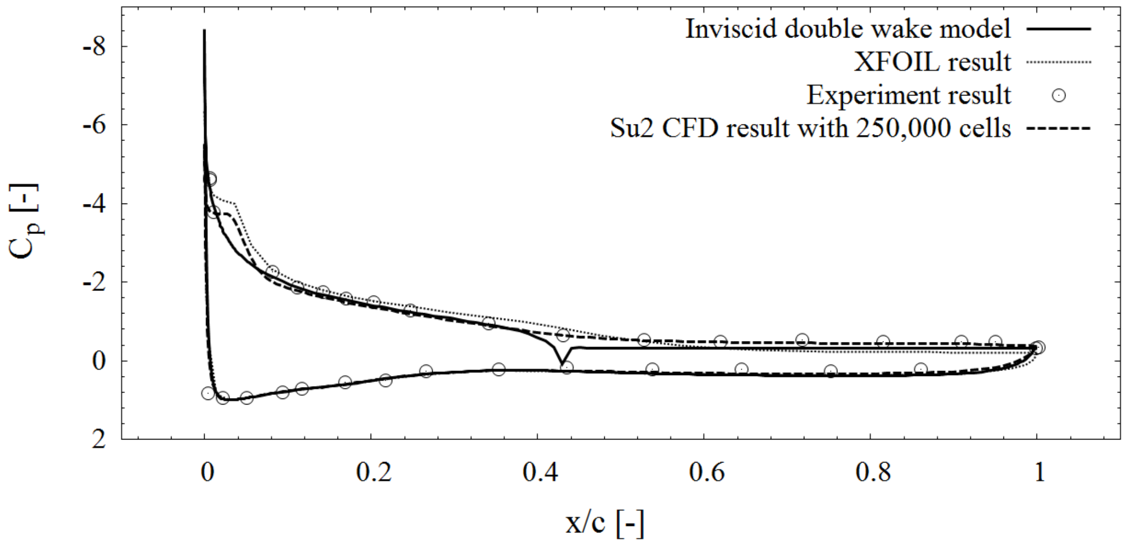

Figure 5.5: Pressure coefficients of inviscid double wake model for S826 airfoil with experiment, XFOIL and numerical result at $Re = 100\,000$ and at AoA of 14.5°.

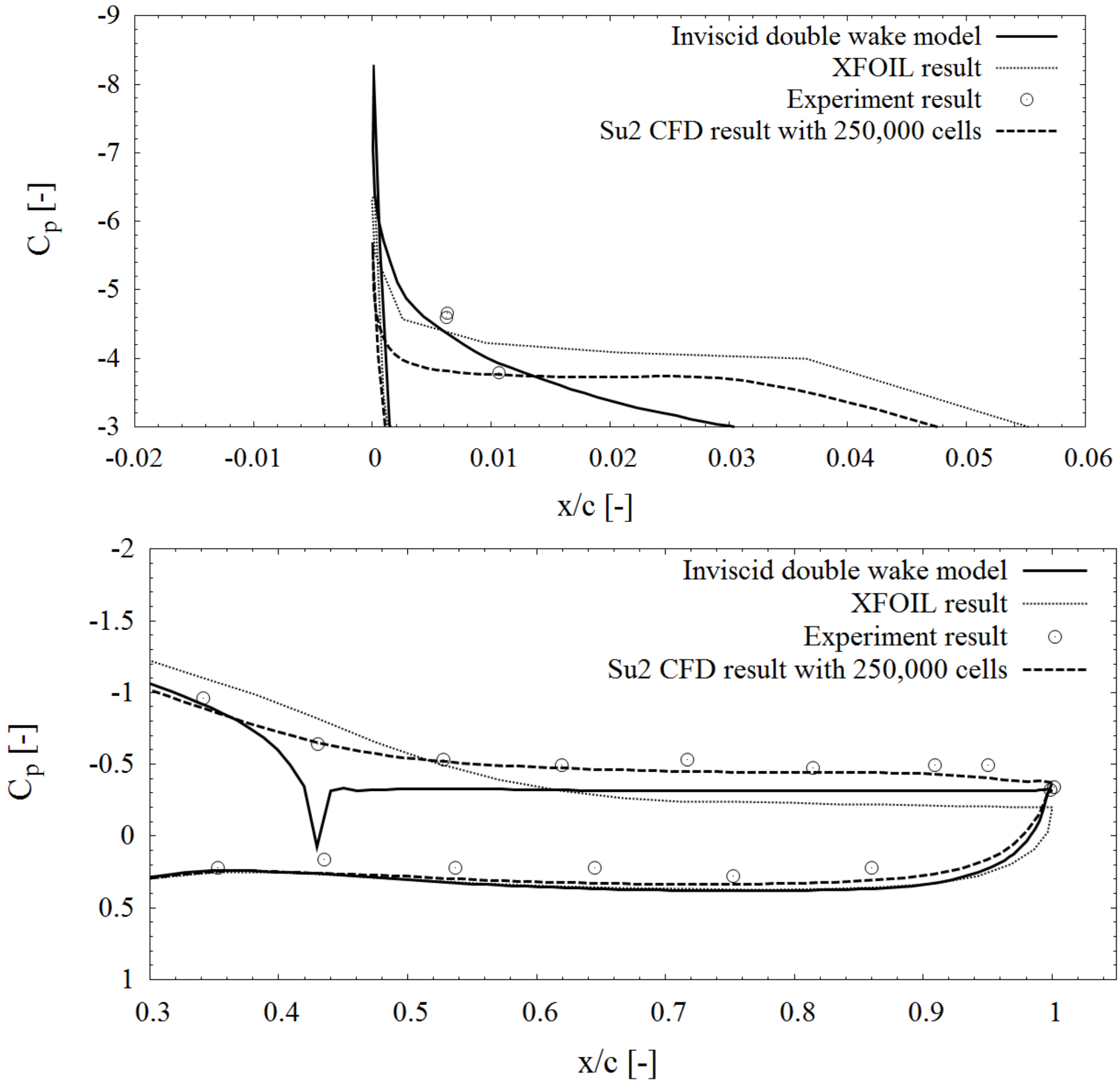

Figure 5.6: A zoom-in to pressure peak at the leading edge suction side (top) and to the separated region (bottom) for S826 airfoil of inviscid double wake model with experiment, XFOIL and numerical result at $Re = 100\,000$ and at AoA of 14.5°.

The initial wake shape used for constructing the constant strength singularity vortex element and final converged wake shape (when C_p over airfoil surface is interpreted), for S826 airfoil at the chosen AoA is shown in the Figure (5.7).

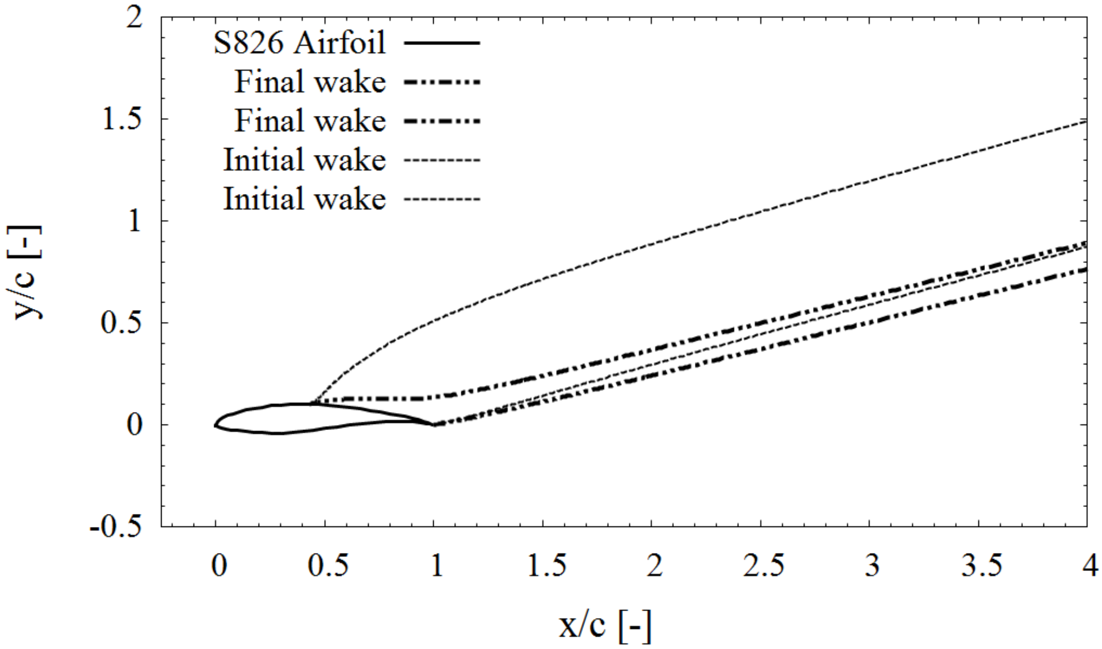

Figure 5.7: Initial and final wake shape of S826 airfoil at $Re = 100\,000$ and at AoA of 14.5°.

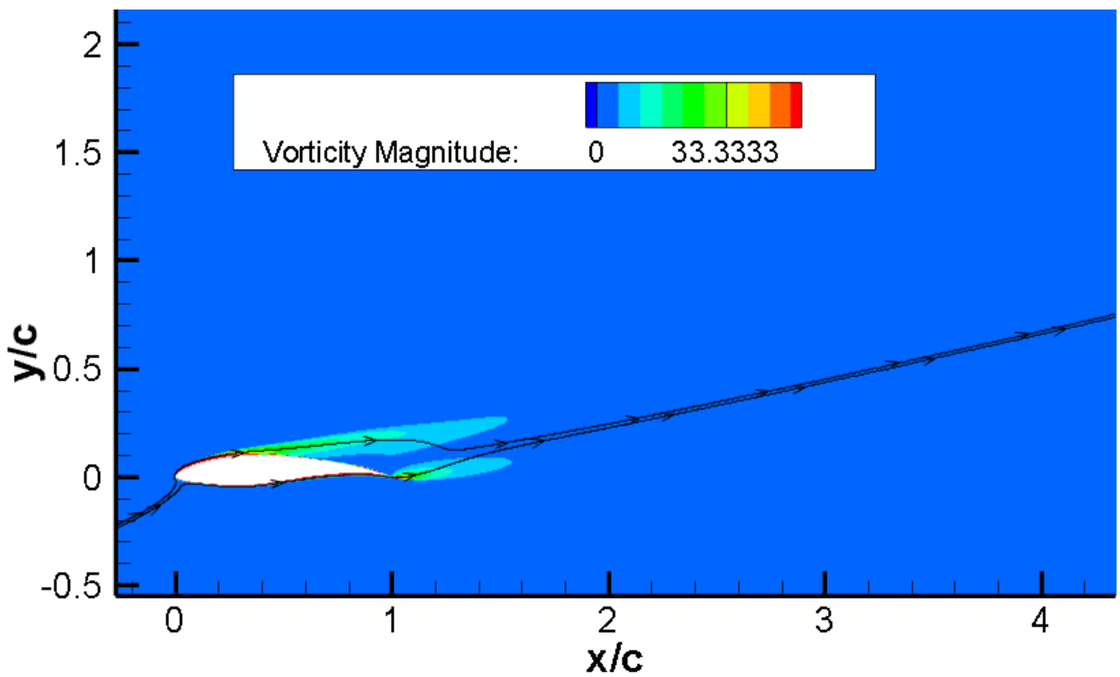

Figure 5.8: Vorticity plot from SU2-CFD simulation with streamlines enclosing the separated region, at $Re = 100\,000$ and at AoA of 14.5°.

Figure (5.8) shows the vorticity plot from CFD simulation with streamlines enclosing the separated flow region. From the figures (5.7) and (5.8), it is evident that the final wake shape representing the converged constant wake sheet from the double wake inviscid model and the streamlines enclosing the separated flow from CFD simulation are nearly similar in shape. This corroborates the reason for the inviscid double wake model predicting result closer to CFD and experimental results.

Figure (5.9) shows the comparison of pressure coefficient for NACA63415 airfoil obtained by the inviscid double wake method along with the simulation results from XFOIL and CFD along with experimental data [22] at Reynolds number of 160 000 and AoA of 16°. The experimental data is obtained for the smooth flow over the NACA63415 airfoil. The separation point for the inviscid double wake method is located at $x/c = 0.475$ and is obtained from experimental data. It can be seen that also for this airfoil the inviscid double wake method can replicate result closer to XFOIL, experimental and numerical viscous solution in the separated flow region. The predicted pressure in the separation region agrees well with the experimental and numerical results and better than that of XFOIL. However, it has to be considered that feeding the separation point from experiment gives added advantage to the inviscid double wake model. The peak suction pressure from the inviscid double wake method mismatches with the results used for comparison. This is due to the fact that the inviscid double wake model has no viscous effects. Further, the release of wake from separation point gives a small oscillation at the separation point as in the previous case. These can be seen from the Figure (5.10).

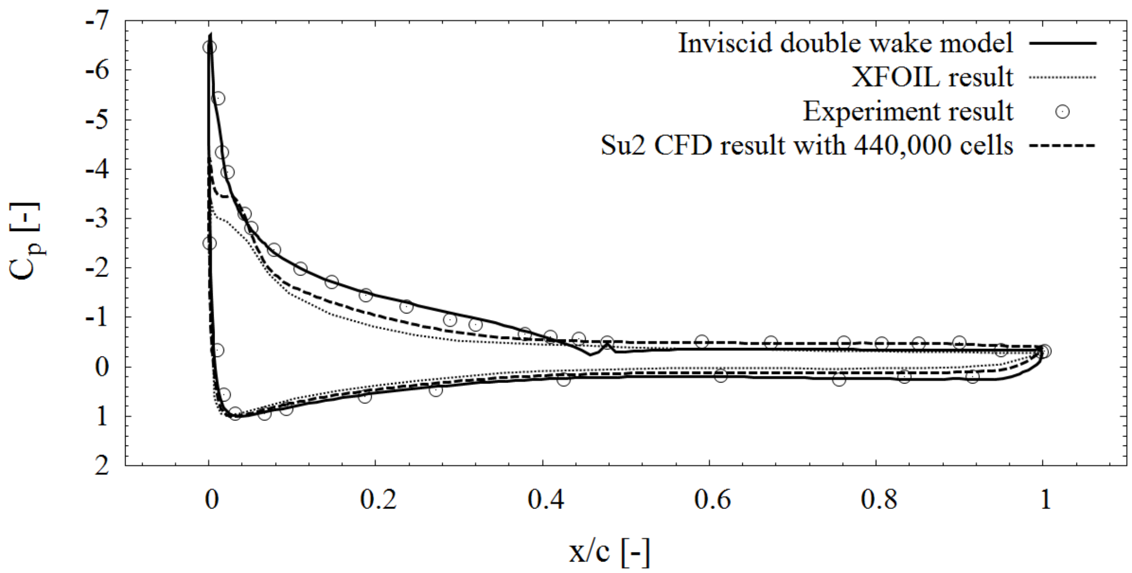

Figure 5.9: Pressure coefficients of inviscid double wake model for NACA63415 airfoil with experiment, XFOIL and numerical result at $Re = 160\,000$ and at AoA of 16°.

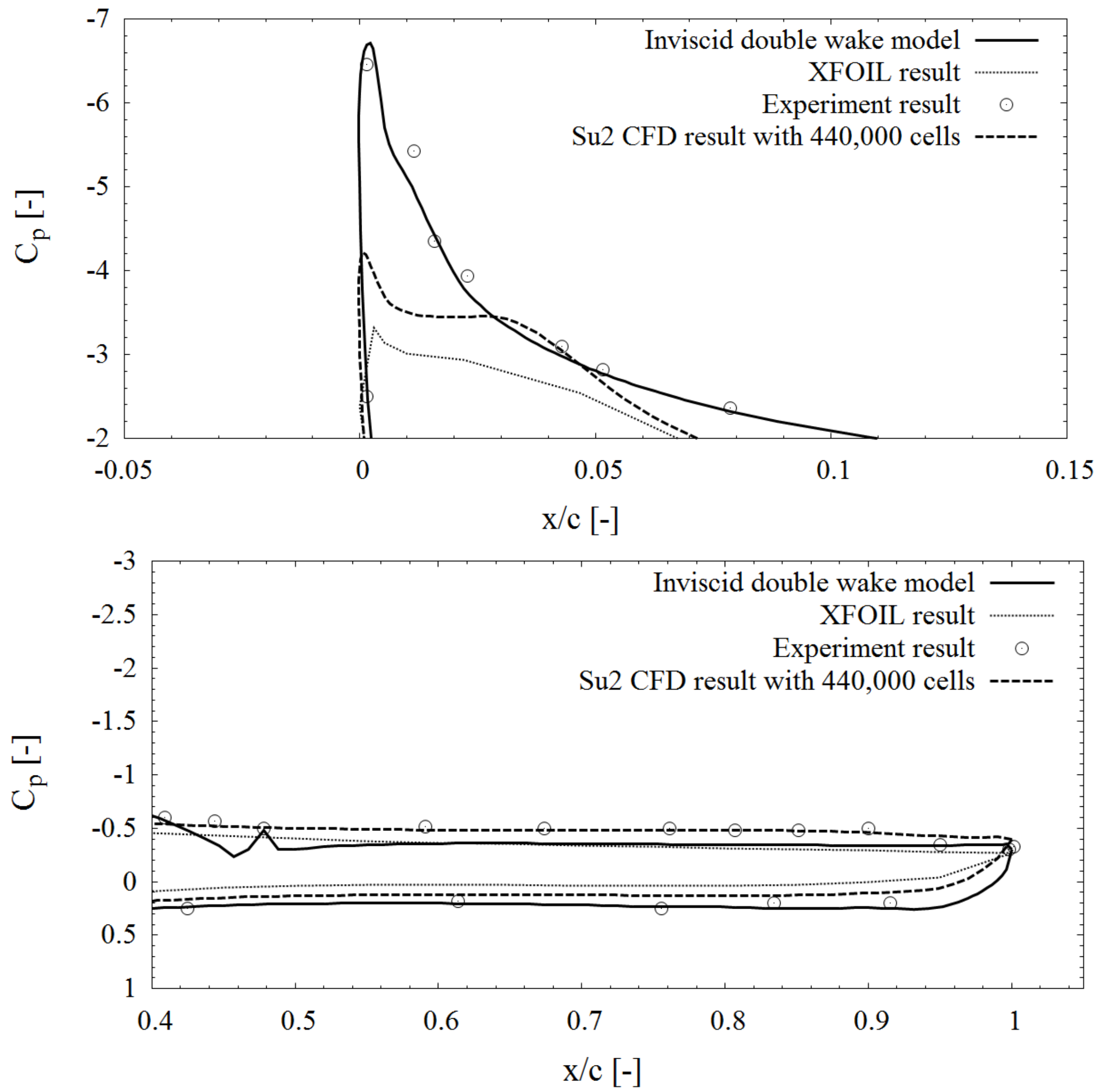

Figure 5.10: A zoom-in to pressure peak at the leading edge suction side (top) and to the separated region (bottom) for NACA63415 airfoil of inviscid double wake model with experiment, XFOIL and numerical result at $Re = 160\,000$ and at AoA of 16°.

The initial wake wake shape used for constructing the constant strength singularity vortex element and final converged wake shape (when C_p over airfoil surface is interpreted), for NACA63415 airfoil at the chosen AoA is shown in the Figure (5.11).

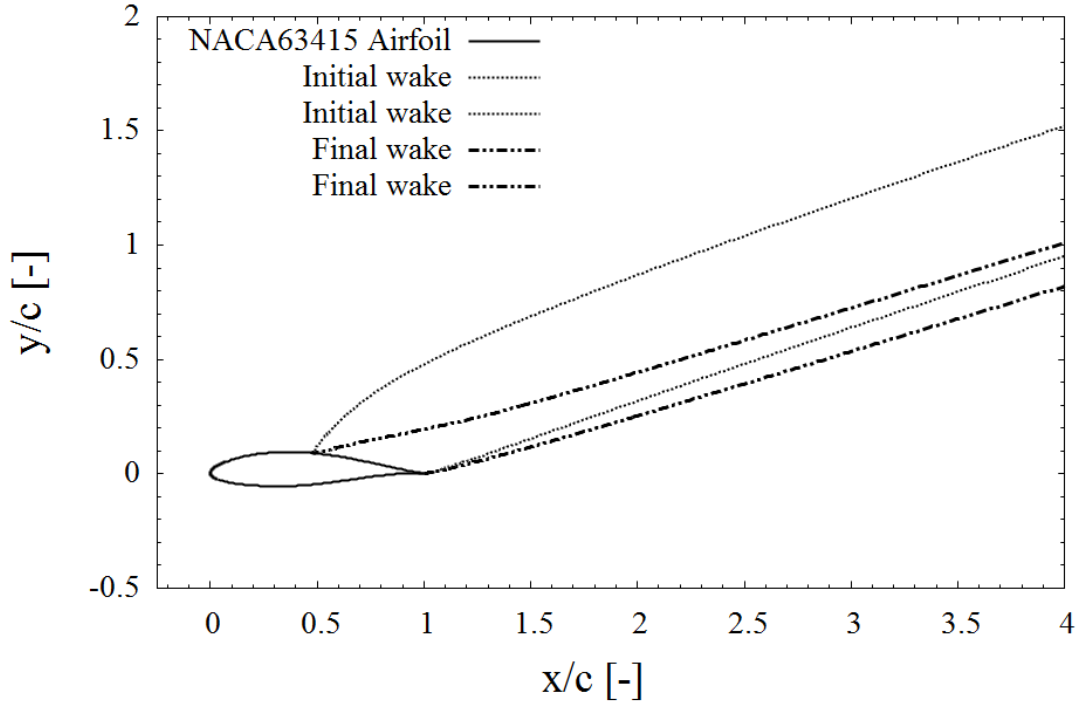

Figure 5.11: Initial and final wake shape of NACA63415 airfoil at $Re = 160\,000$ and at AoA of 16°.

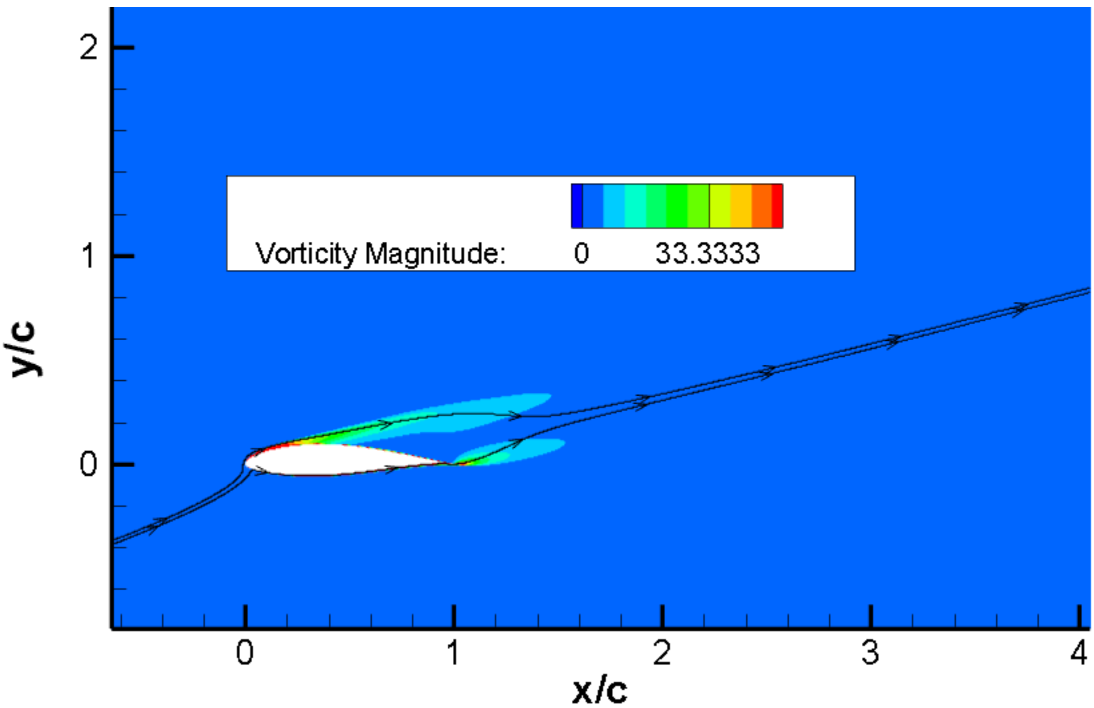

Figure 5.12: Vorticity plot from SU2-CFD simulation with streamlines enclosing the separated region, at $Re = 160\,000$ and at AoA of 16°.

Figure (5.12) shows the vorticity plot from CFD simulation with streamlines enclosing the separated flow region. From the figures (5.11) and (5.12), it can be seen that the final wake shape representing the converged constant wake sheet from the double wake inviscid model and the streamlines enclosing the separated flow from CFD simulation are nearly similar in shape. This corroborates the reason for the inviscid double wake model predicting result closer to CFD and experimetnal results.

The results from SU2 agrees well with the experiment for the cases shown above, with S826 and NACA63415 airfoils. In Figure (5.13) the SU2 results are compared with the double wake inviscid model for S826 airfoil at AoA of 20° and Reynolds number of $3 \cdot 10^6$ where RFOIL has convergence failure and no experimental results are available. The separation point for the double wake inviscid model is located at $x/c = 0.13$ and is obtained from the skin friction coefficient of numerical result (SU2) when it becomes negative. Prior to this, three different meshes namely 250 000, 500 000 and 2 000 000 cells are studied to determine the mesh independent solution and based on the study, the mesh with 250 000 cells is chosen for solution comparison.

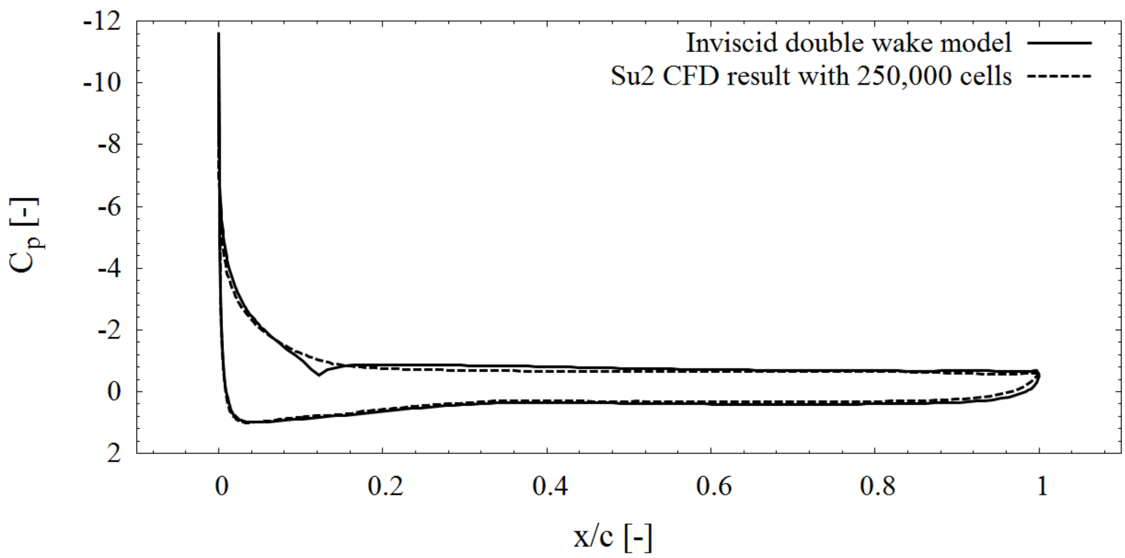

Figure 5.13: Pressure coefficients of inviscid double wake model for S826 airfoil with numerical result at $Re = 3 \cdot 10^6$ and AoA of 20°.

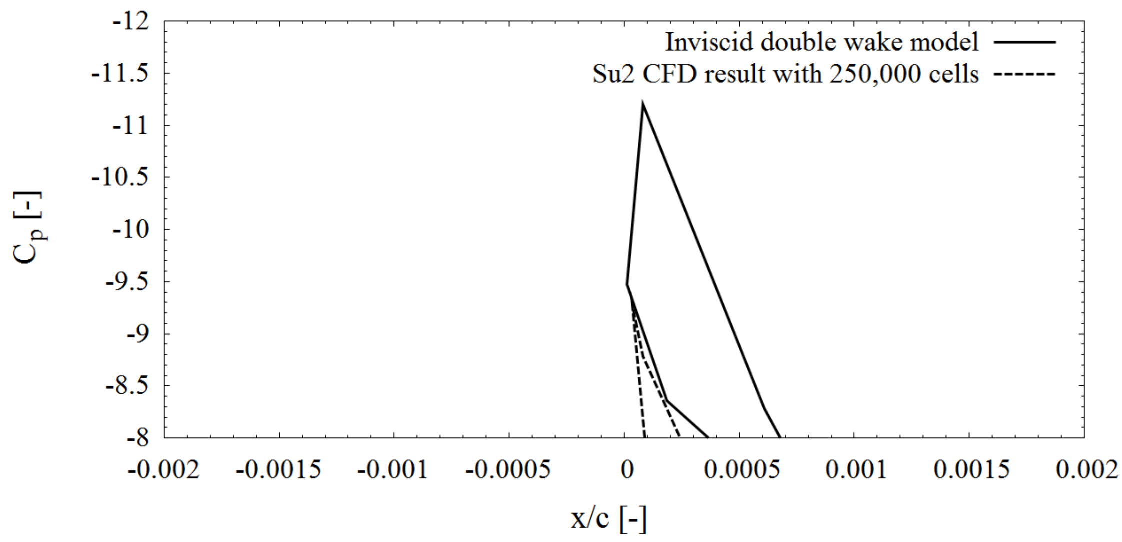

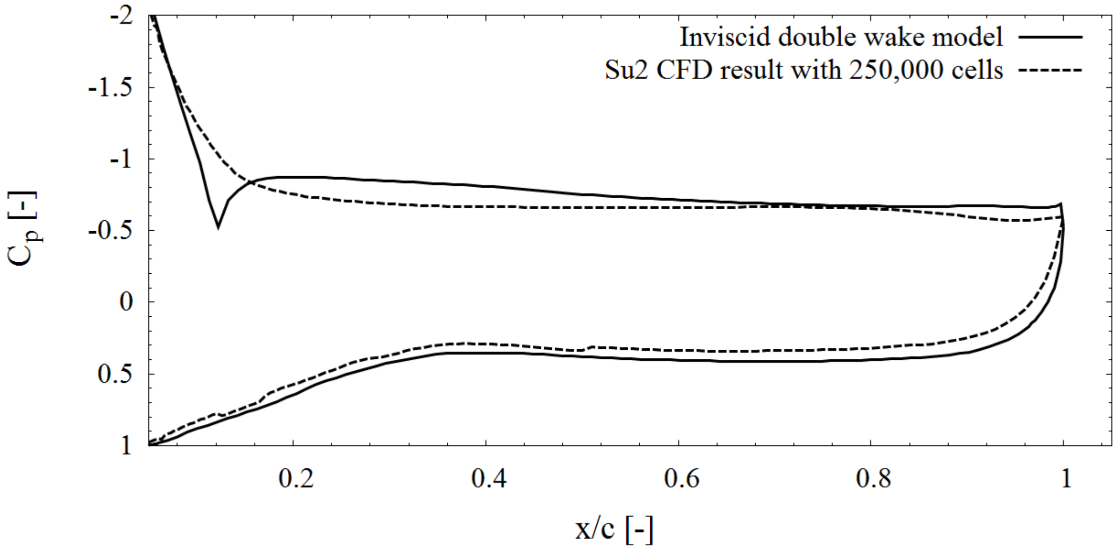

Figure 5.14: A zoom-in to pressure peak at the leading edge suction side (top) and to the separated region (bottom) for S826 airfoil of inviscid double wake model with numerical result at $Re = 3 \cdot 10^6$ and at AoA of 20°.

Figures (5.13) and (5.14) show that the double wake inviscid model results are in good agreement with that of numerical (SU2) results in the separated region. In the non-separated flow region, there is discrepancy in the calculated C_p from double wake inviscid model. This is due to the fact that the inviscid double wake model has no viscous effects. Therefore, the double wake inviscid model on coupling with viscous effects can give reasonable results and overcome the convergence problem posed by RFOIL.

5.3 Validation case with blunt trailing edge airfoil

Result for blunt trailing edge airfoil is shown in the Figure (5.15) using FFA-W3-301 30% thick airfoil. The plot shows the pressure distribution obtained from inviscid double wake model along with the experiment [23] and XFOIL results at $Re = 1.6 \cdot 10^6$ and AoA of 16.7°. The experimental data is obtained for the smooth flow over the FFA-W3-301 airfoil. The separation point for the inviscid double wake method is located at $x/c = 0.41$ and is obtained from experimental data. It can be seen that the pressure distribution in the separation region can be captured to a very good accuracy when compared to experiment. The inviscid double wake model gives more accurate result than XFOIL viscous simulation. However, it has to be considered that feeding the separation point from experiment gives added advantage to the inviscid double wake model. There is mismatch of the presure distribution between the inviscid double wake model and the experiment in the non-separated flow region. It has to be noted that the inviscid double wake model has the disadvanatge of not having viscous effects. Further, the release of wake from separation point gives a small oscillation at the separation point.

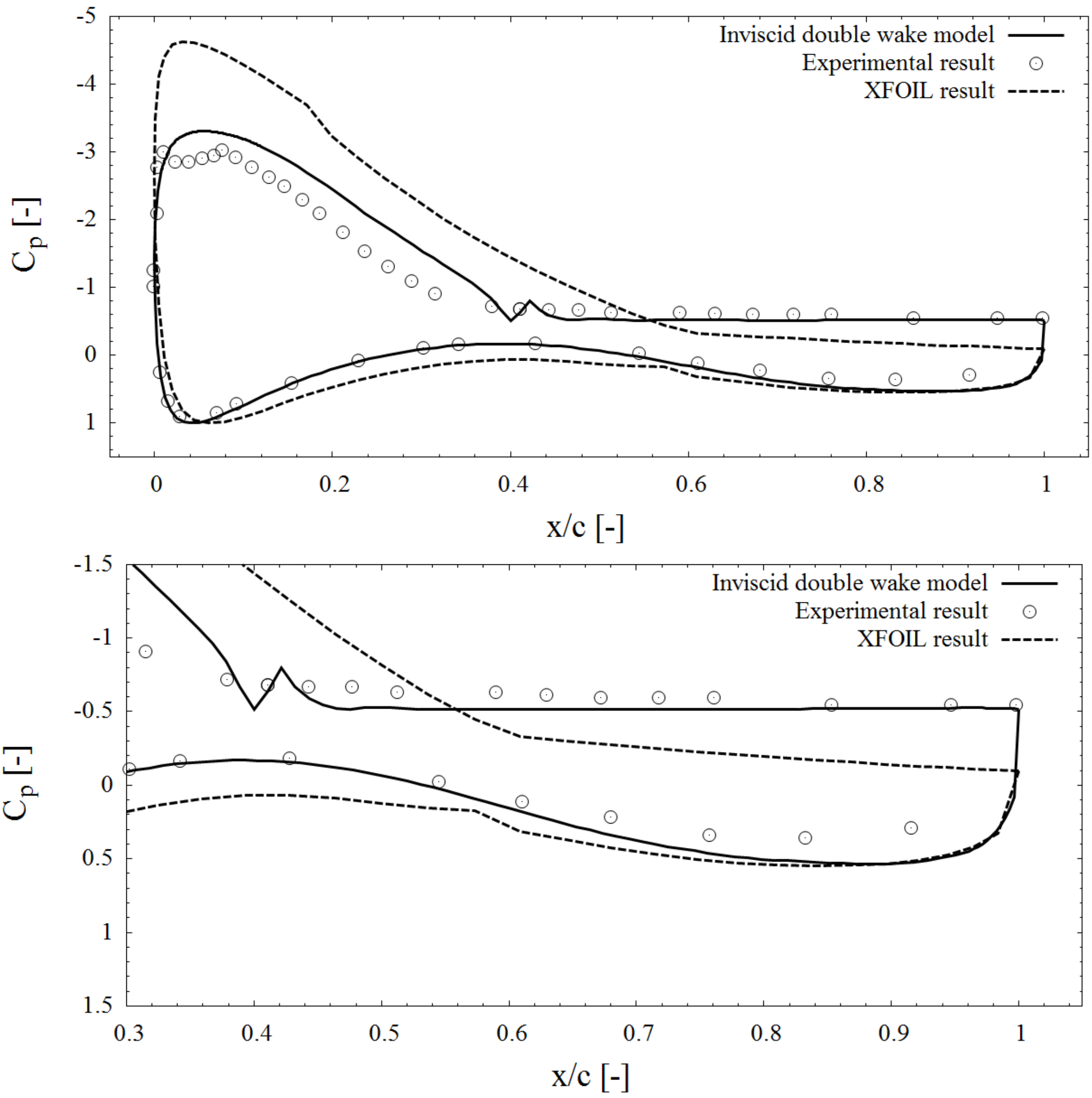

Figure 5.15: Pressure coefficients for FFA-W3-301 airfoil (top) and a zoom in to the separated region (bottom) of inviscid double wake model with experiment and XFOIL result at $Re = 1.6 \cdot 10^6$ and AoA of 16.7°.

5.4 Numerical results beyond stall

Figure (5.16) shows the pressure coefficient obtained by the double wake inviscid model for S825 airfoil at Reynolds number of $2 \cdot 10^6$ with experimental results [24]. From the experimental data it is observed that at the chosen Reynolds number of $2 \cdot 10^6$, the stall angle of attack is 12°. The near post stall characteristics is studied for angle of attack of 13° and 14°. The separation point for the double wake inviscid method is taken from the experimental data [24] to be 70% and 50% of the chord length for angle of attack of 13° and 14° respectively. The peak suction pressure tends to decrease with increasing angle of attack in the near post stall and the same is observed from the plot of inviscid double wake method at AoA of 13° and 14°.

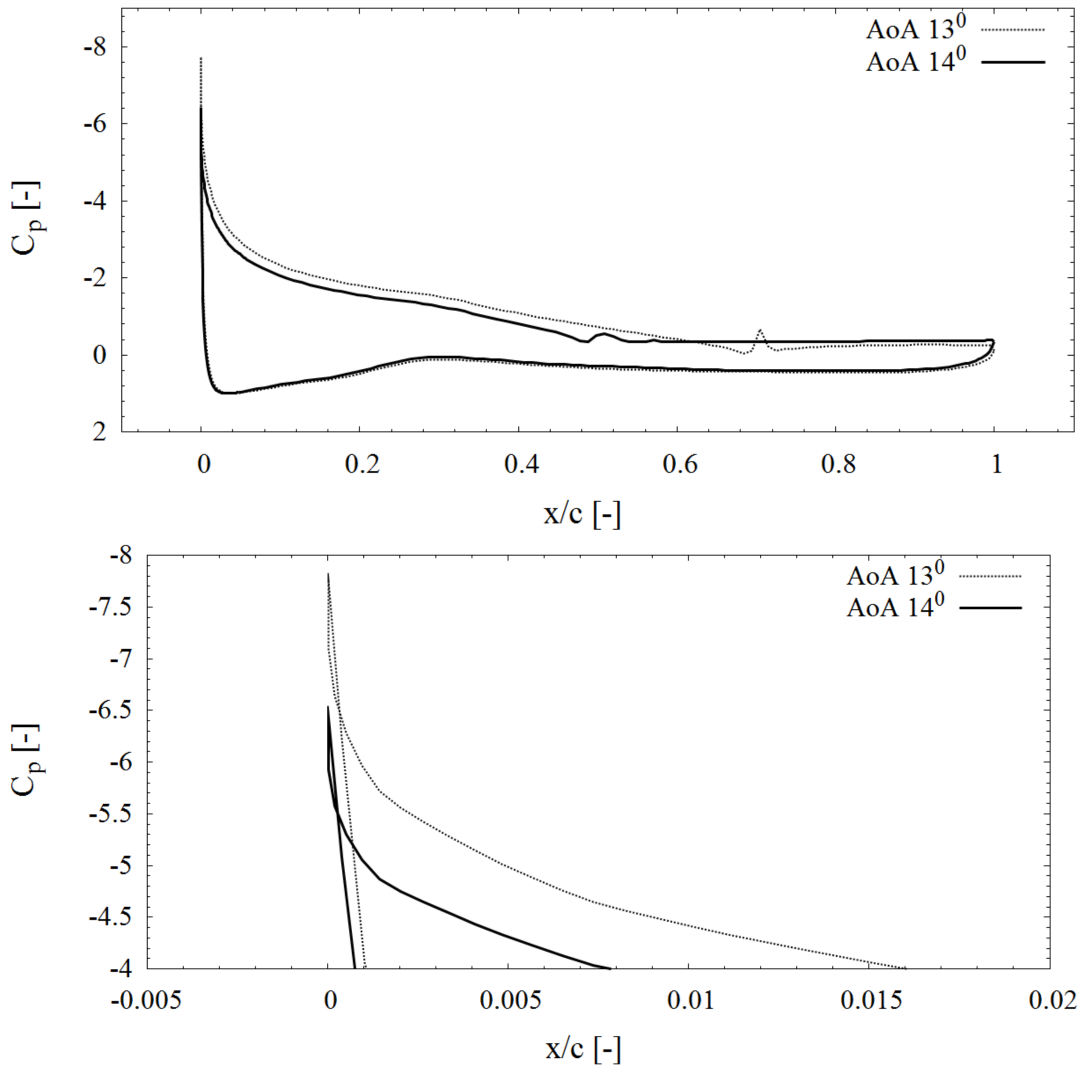

Figure 5.16: Pressure coefficients for S825 airfoil (top) and a zoom-in to pressure peak at the leading edge suction side (bottom) of inviscid double wake model at $Re = 2 \cdot 10^6$ and AoA of 13° and 14°.

Figure (5.17) and Figure (5.18) show the pressure coefficient obtained by the double wake inviscid method with the experimental result at angle of attack of 13° and 14° respectively, for S825 airfoil at Reynolds number of $2 \cdot 10^6$. It can be seen that the pressure distribution in the separation region can be captured to a very good accuracy. However, the pressure distribution calculated by the inviscid double wake model in the non-separated flow region, is comparatively different from the experimental result. The inviscid double wake model predicts higher suction peak pressure than the experiment for AoA of 13°. This is vice versa at angle of attack of 14° which can be observed from the figures. As already stated, this is due to the fact that the inviscid double wake model has no viscous effects.

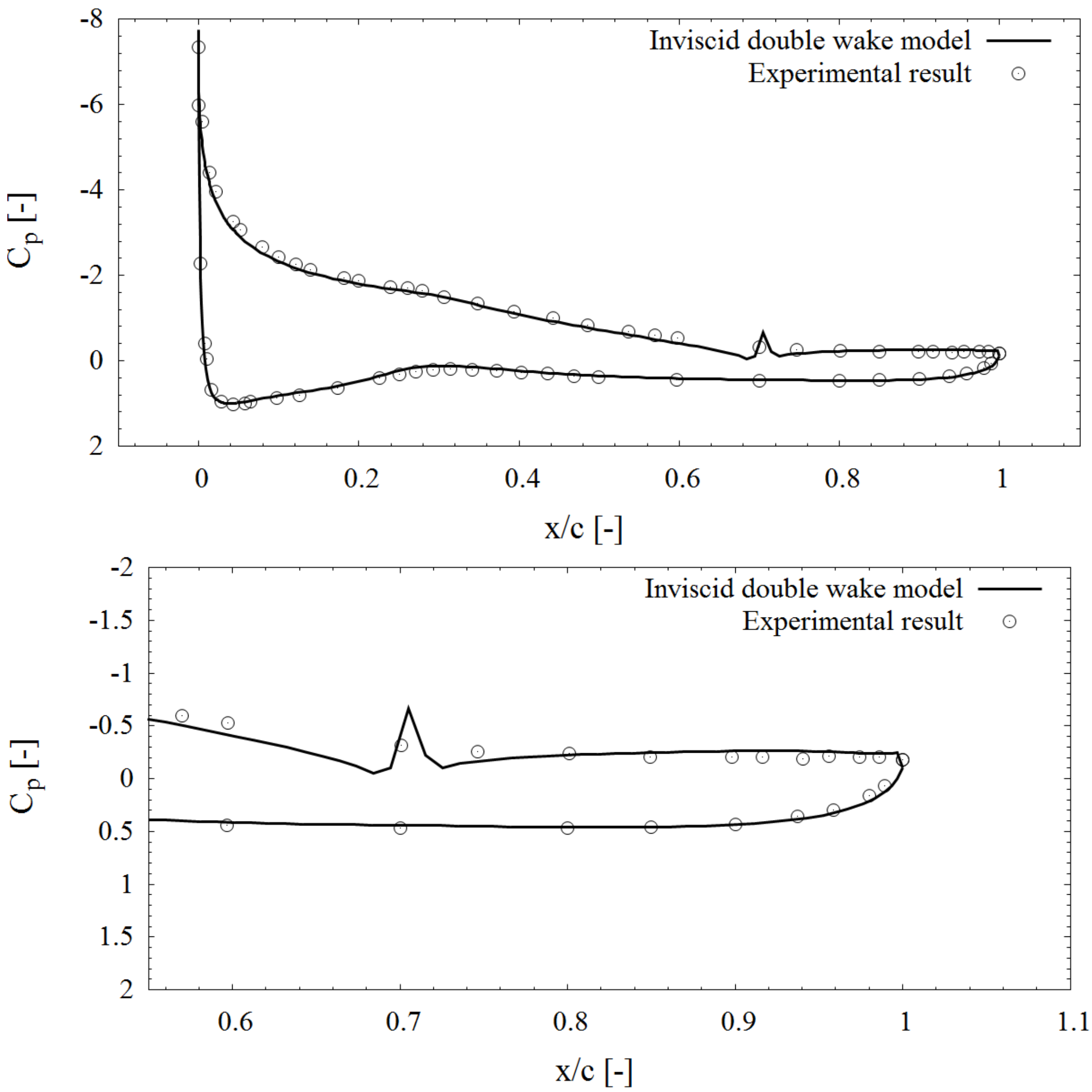

Figure 5.17: Pressure coefficients for S825 airfoil (top) and a zoom in to the separated region (bottom) of inviscid double wake model with experimental result at $Re = 2 \cdot 10^6$ and AoA of 13°.

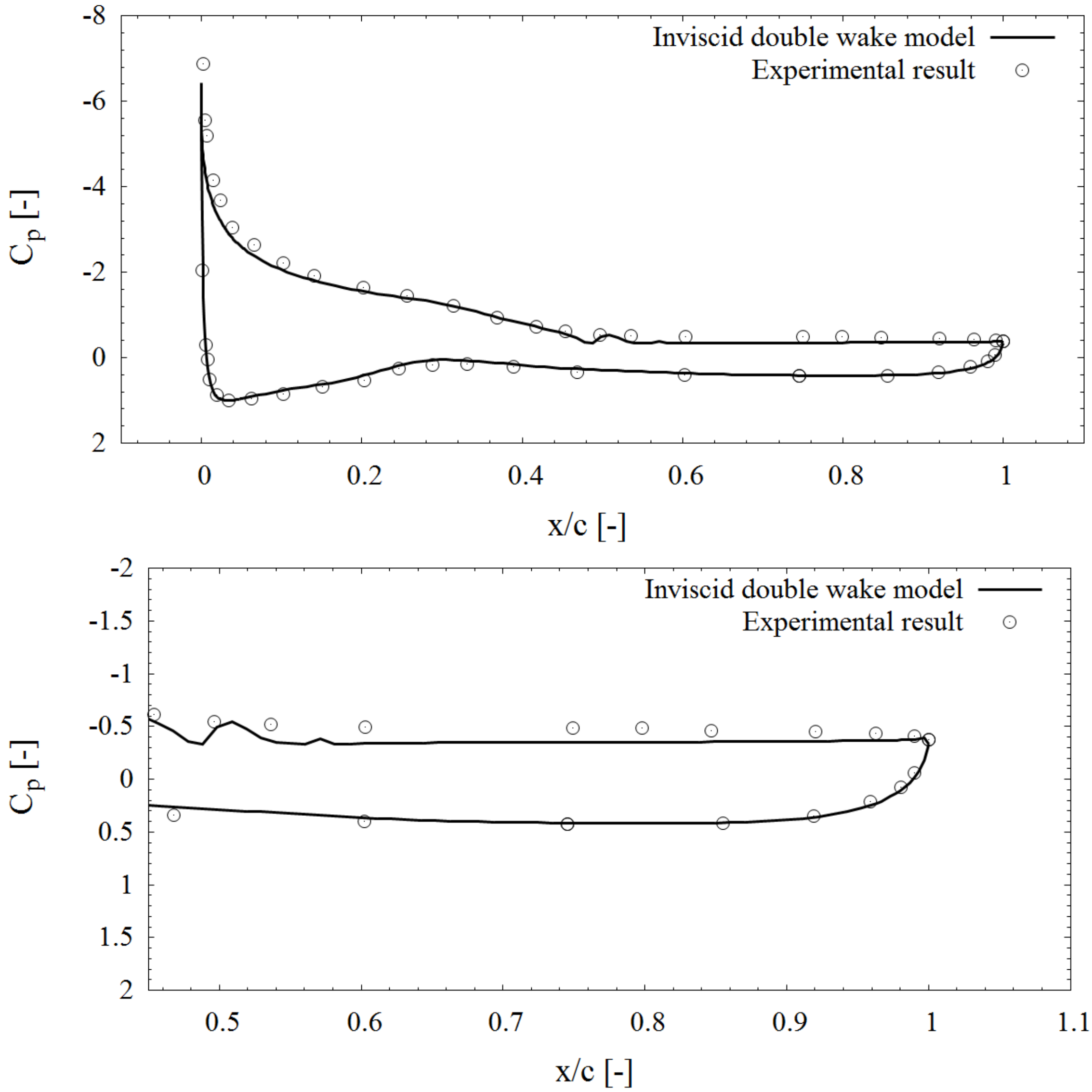

Figure 5.18: Pressure coefficients for S825 airfoil (top) and a zoom in to the separated region (bottom) of inviscid double wake model with experimental result at $Re = 2 \cdot 10^6$ and AoA of 14°.

In all the results presented, a small and sharp variation in C_p is observed at the immediate downstream of the separation point. The pressure distribution is constant in the separated flow region and so the vorticities. There is a large difference between the γ_{SEP} and the vorticity on airfoil surface in the separated region. Due to the large difference, the immediate downstream vorticity in the separated region undergoes some variation before becoming constant. The sharp change in C_p occurs as the total pressure jump is considered including the immediate downstream of separation point.

Chapter 6

Dynamic stall modelling

The lift coefficient of the airfoil increases with angle of attack until it stalls. At stalled angle of attack, static stall occurs as a result of flow separation, increasing the pressure drag thereby decreasing the performance (lift) of the airfoil. The reversal of flow in the separated region is in fact dynamic in nature. Further, dynamic stall is exhibited by the airfoil that undergoes periodic pitching under varying flow conditions. This is a complex phenomenon that need to be prevented. Hence, accurate dynamic stall model is essential to predict the phenomena and to overcome it. Unlike static stall which can be avoided by either not operating in these conditions or postponing flow separation by use of vortex generators, dynamic stall is difficult to predict and control. Dynamic stall occurs at a higher angle of attack than static stall. Dynamic stall is due to delay in the stall onset. The physics of flow separation is different for dynamic stall on comparison with static stall. On the onset of dynamic stall, the shear layer in the suction side of the leading edge rolls up forming leading edge vortex. This reduces the pressure at the leading edge and therefore increases the lift. However, the formed vortex is highly unstable and convected downstream which makes the lift to drop drastically. Also, dynamic stall leads to vibrations and high loads, making wind turbine structurally vulnerable to fatigue. Therefore, predicting the dynamic stall is much essential.

Dynamic stall models [26] can be empirical or semi-empirical. Currently, the dynamic stall models in use are semi-empirical. The models have non-linear and linear equations representing essential physics in it. However, empirical coefficients obtained from experiments for unsteady environment do exist in the models. As the dynamic models are semi-empirical, there are some disavantages in these models. They lack generality as the empirical coefficient have to be calculated for each airfoil at specific Mach number. Further, the majority of the coefficients calculated are more applicable to compressible flows. The second drwaback is the models use large number of empirical coeeficients and their quantitative description show very subtle changes which affects the accuracy of the model. Though these coefficients are predicted accurately from the experiments, the real time operating conditions for the airfoils are different from experiments. Hence the different models described in the following subsection can be used with reliance where their performance is validated with experiments.

6.1 Different types of dynamic stall models

6.1.1 UTRC α, A and B Model

This model [27, 28] is a resyntheis of unsteady load calculated for oscillating airfoil in a wind tunnel. In the attached flow conditions, the method is expressed in terms of AoA (α), $A = \dot{\alpha}c/2U_0$ and $B = \ddot{\alpha}c^2/4U_0^2$. From the measured unsteady loads the static contributions are subtracted to get the dynamic contributions of the load. For any given operating parameters, the dynamic loads is interpolated from the available dynamic data set and this contribution is added to the respective static values. This method was successful to an extent. However, the requirement of large data sets for each airfoil and every operating conditions (for every Mach number) is a huge setback of this model.

6.1.2 Gamma function model

This is also a resynthesis model [27, 28] and is based on empirical gamma function obtained for unsteady 2D oscillating airfoil. Firstly, the effective angle of attack is calculated from the Theodorsen theory [29, 6] at appropriate reduced frequency. The theory is valid for attached flows and for very thin airfoils considering them as flat plate. Secondly a correction is applied to the angle of attack from the gamma function obtained experimentally. The corrected angle of attack is then used to obtain airfoil loads from the static load curve. From this method good acuracy of unsteady airloads can be obtained but the accuracy in predicting stall onset is lost.

6.1.3 Time delay model

Unlike the previous two resynthesis models, this model [30, 27, 28] is made to describe the dynamic stall process. This model is dependent on time and two non-dimensinal time delays are used in this model. The first time delay is to capture the delay in the dynamic stall onset (the time for separation to begin) once the static stall condition has been exceeded. The second time delay is for the release of the developed leading edge vortex. Both the time delays are obtained from experiments for large number of airfoils and over a larger range of mach numbers. The result of this model shows good prediction of dynamic stall and this uses less empirical constants.

6.1.4 Gangwani's model

This model [31, 27, 28] is also based in the time domain and is similar to the time delay model. The model is made of linear and non-linear parts. However, this model uses large number of empirical coefficients obtained from the oscillating airfoil. This model gives accurate predictions of attached and separated flows. However, it looses accuracy in predicting flow reattachment after the stall.

6.1.5 Johnson's method

The semi-empirical model [27, 28] is developed from the experimental data to correct the static stall and pitching moment as a function of pitch rate. The model gives good result of lift coefficient but lacks accuracy on predicting the pitching moment.

6.1.6 Onera model

The onera semi-empirical model [27, 32] consist of a first order linear equations to contribute for the aerodynamic coefficients in the attached flow regime and second order differential equations to represent stall phenomena. This model requires large number of experimental coefficients. The lift coefficient in the differential form is given by

$$\begin{aligned} \dot{c}_l + \gamma_L c_l &= \gamma_L c_l^{ps} + (\gamma_L s_L + \sigma_L)\dot{\alpha} + s_L \ddot{\alpha}, \\ \ddot{c}_l + a_L \dot{c}_l + r_L c_l &= -(r_L \Delta c_l + e_L \dot{\Delta} c_l). \end{aligned} \tag{6.1}$$

The constants γ_L, s_L, σ_L, a_L, e_L, r_L in the equation (6.1) are determined based on experiment. However, if the experimental data are not available, only the first three constants can be taken from flat plate dataset but not the remaining constants. Further, the model is linearised on the assumption that there is little difference between static and dynamic lift coefficient which is not true with the wind turbines.

6.1.7 Snel method

This model [27, 32] has two parts as that of Onera model, linear and non- linear equations to describe attached and stalled flow respectively. This model requires no airfoil specific empirical coefficients for modelling. The prediction of the model is theoritically accurate. However, the results of the comparison study of many airfoils as described in [32] state the LB model in the section (6.1.8) gives better prediction of dynamic stall compared to Snel method.

6.1.8 Leishman-Beddoes model

The Leishman-Beddoes (LB) model [33] was developed in order to overcome the deficits of the other dynamic models described above. This model is built on the static variables as input and consists of following subsystems namely,

1. A non-linear model for attached flow to calculate unsteady aerodynamic forces.
2. A non-linear model to represent separated flow and to calculate aerodynamic forces.
3. A dynamic stall onset model with two time delays related to pressure distribution and separation point.
4. A non-linear model to account for the lift contribution from vortex formation.

Time delays used in the model are implemented in a logically determined manner to model the complex viscous effects. It has to be noted that this is the only model to take flow separation explicitely into account.

This model has less empirical coefficients in it and so it overcomes the inaccurate predictions of aerodynamic coefficients, where the empirical coefficients can not be determined corresponding to the flow phenomena. Further, all the inputs required except for the four empirical coefficients can be obtained from steady airfoil data which makes this model easier to implement. From the theory this model is the most accurate of all developed so far and so this model is used for implementation.

6.2 Implementation of the dynamic stall model

The LB model [34] is formulated using indicial functions as this proved to be a most effective solution procedure. The original LB model uses twelve state-space variable in the formulation for compressible flows. There are many adaptations of this LB model [35, 36]. For wind turbine application, this model has been adopted with several modifications and four state variables by Hansen [34], where compressibility effects are negligible. However, this model has excluded the flow separation from the leading edge (lift contribution from leading edge vortex). This below described dynamic stall model is based on Hansen with the contribution of vortex lift from the work of J.B. Vaal [37].

The model is for stationary pitching airfoil. In static scenario, the aerodynamic coefficients depend on angle of attack but in case of dynamic flow consideration they also depend on various parameters such as mean angle of attack, amplitude of oscillation and reduced frequency. The required inputs for the model are the static lift coefficient (C_l), AoA, four constants (A_1, A_2, b_1, b_2), effective velocity and the reduced frequency (k) and three time delays (T_p, T_f and T_v). The four constants that are used, are airfoil dependent and determined based on experiment.

6.2.1 Schematic representation

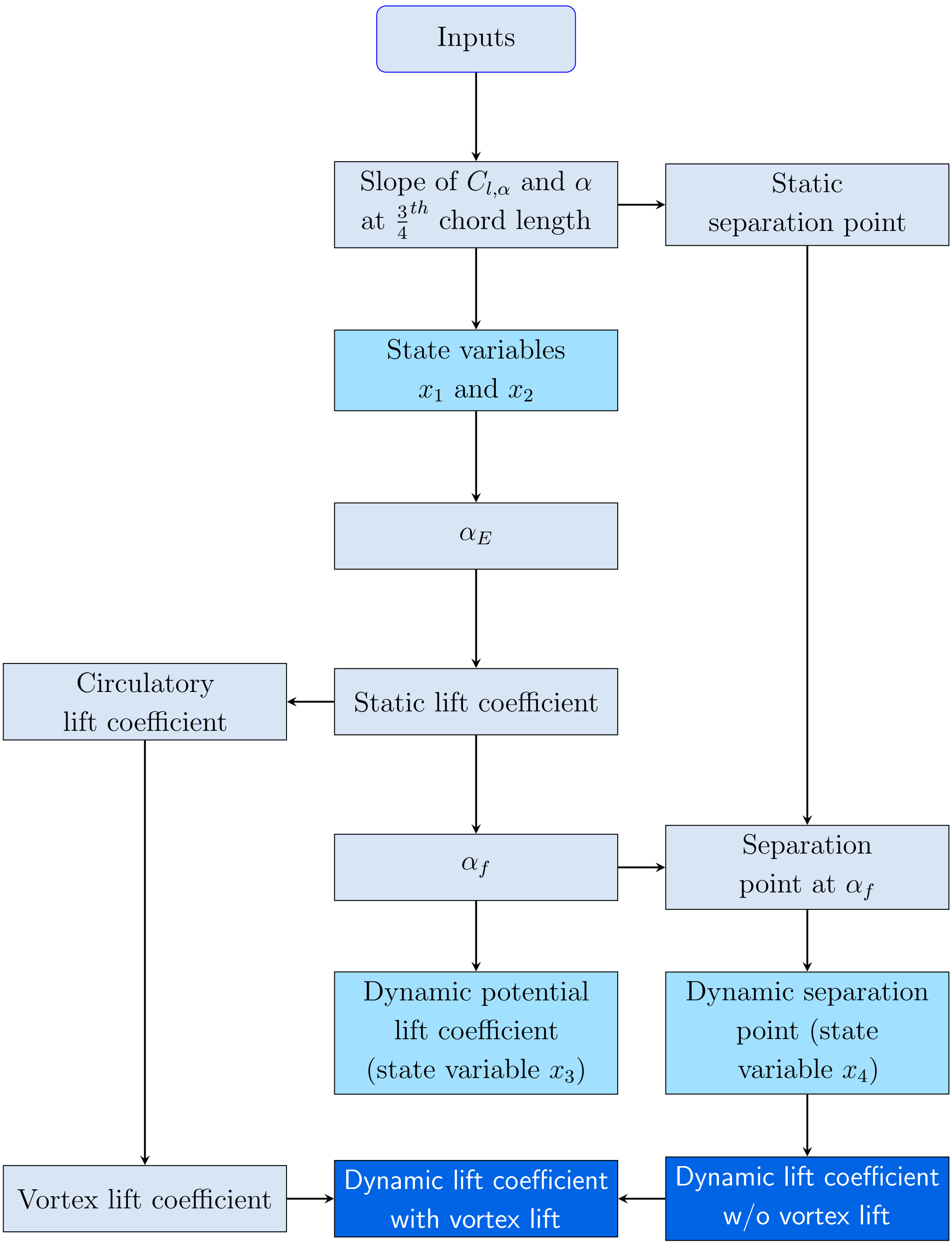

6.2.2 Attached flow

The present LB model uses Theordorsen theory of thin airfoils (maximum 15% thickness) with the modification of varying freestream velocity for attached flow modelling. For thin airfoils, the experimentally determined constants are $A_1 = 0.3, A_2 = 0.7, b_1 = 0.14$ and $b_2 = 0.53$. For airfoils of thickness larger than 15%, these constant values A_1, A_2, b_1 and b_2 used in the model need to be changed. The pressure lag is taken to be $T_p = 2.5$ which is to account for the delay of onset of dynamic stall. The separation point position lag is taken to be $T_f = 3$. The constant $T_v = 6$ is to account for the delay in the release of the formed vortex (i.e. vortex lift contribution). The constants are given in [33] and are based on compressible flow regime. Here, the values are taken for lowest available Mach number as stated in [37]. They can be changed as per requirement. The reduced frequency of wind turbine is between 0.02 to 0.1 and Leishmann specified that for these moderate reduced frequency, all the theories give same result as that of Theodorsen theory and so it is being used in this model [34].

The aerodynamic forces for the attached flow is obtained from the indicial responses for the given input. The Wagner or Küssner function are used for these models and are both applicable for incompressible flows [38]. The former gives responses for step change in the input AoA and the latter for the airfoil undergoing vertical gust near leading edge. The attached flow consists of circulatory load which starts from zero and asymtotically reaches steady state and impulsive load which dies out after initial loading. These are effectively described by the indicial response function which is described below

$$\phi(s) = 1 - Ae^{-bs}. \tag{6.2}$$

For the changing angle of attack, the indicial response function changes into Wagner function which is,

$$\phi(s) = 1 - A_1 e^{-b_1 s} - A_2 e^{-b_2 s}. \tag{6.3}$$

The above described function is used for calculating effective angle of attack. The following equation set is used to calculate the four state variables,

$$\begin{aligned}
\dot{x_1} + \frac{2U_0}{c}(b_1 + \frac{c\dot{U}}{2U_0^2})x_1 &= b_1 A_1 \frac{2U_0}{c}\alpha_{3/4}, \\
\dot{x_2} + \frac{2U_0}{c}(b_2 + \frac{c\dot{U}}{2U_0^2})x_2 &= b_2 A_2 \frac{2U_0}{c}\alpha_{3/4}, \\
\dot{x_3} + \frac{x_3}{T_p} &= \frac{C_l^{Ps}}{T_p}, \\
\dot{x_4} + \frac{x_4}{T_f} &= \frac{f_{\alpha_f}}{T_f}.
\end{aligned} \tag{6.4}$$

The family of equations as in the equation (6.4) is of the form,

$$\dot{x}_i + P_i x_i = Q_i. \tag{6.5}$$

Hence the solution as in [34] is given by,

$$\begin{aligned} x_i(t+\Delta t) &= x_i(t)(e^{-P_{bar}dt}) + \frac{Q_{bar}}{P_{bar}}(1-e^{-P_{bar}dt}), \\ P_{bar} &= 0.5(P_i^j + P_i^{j-1}), \\ Q_{bar} &= 0.5(Q_i^j + Q_i^{j-1}), \end{aligned} \tag{6.6}$$

where j indicates the time marching. Here the P_i and Q_i are assumed to be linear and any other higher order can be considered to increase the accuracy.

As the model is for stationary pitching airfoil, all the effective velocities in the model is taken to be the freestream velocity (U_0). The angle of attack is then made in the form,

$$\alpha = C + Dsin(\omega t), \tag{6.7}$$

where, C is the mean angle and D is the amplitude. From the input AoA, the effective AoA (α_E) and the quasi-steady AoA (α_f) are calculated. The slope of the static curve $C_{l,\alpha}$ is taken for the attached flow region as

$$C_{l,\alpha} = max(\frac{C_l^{st}}{\alpha - \alpha_0}), \tag{6.8}$$

where, α is the AoA and α_0 is the zero lift AoA. This model utilises angle of attack at 3/4 of the chord ($\alpha_{3/4}$) from the effective downwash ($\omega_{3/4}$). The downwash is represented as the sum of plunge velocity, pitching velocity and the acceleration component as,

$$\begin{aligned} \alpha_{34} &= \omega_{3/4}/U_0, \\ \omega_{3/4} &= \dot{h} + \alpha U_0 + 0.5c\dot{\alpha}. \end{aligned} \tag{6.9}$$

Here the plunging component ($\dot{h}$) is made zero for the analysis. The time derivative AoA is used to calculate the mass component in impulsive loading,

$$\dot{\alpha} = 2B\pi cos(\omega s). \tag{6.10}$$

As the freestream velocity is constant in this case, the dimensionless time s is given by the equation by,

$$s = \frac{2}{c}\int_0^t U_0 dt = \frac{2U_0 t}{c}. \tag{6.11}$$

The effective angle of attack can be calculated with the first and second state variables from the equation (6.4) as,

$$\alpha_E = \alpha_{3/4}(1 - A_1 - A_2) + x_1 + x_2. \tag{6.12}$$

The quasi-steady angle of attack with the delay T_p and the third state variable are calculated as,

$$\alpha_f = \frac{x_3}{C_{l,\alpha}} + \alpha_0. \tag{6.13}$$

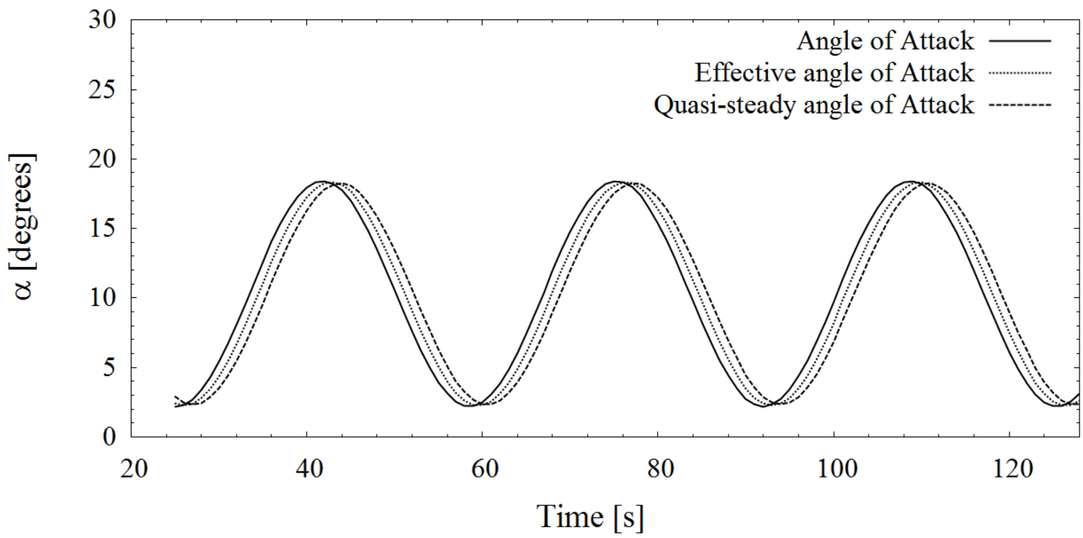

Figure 6.1: Plot of input AoA, the effective AoA (α_E) and the quasi-steady AoA (α_f) with respect to time.

Figure (6.1) shows the plot of α, α_E and α_f for NACA0012 airfoil with $C = 10.3°$ and $D = 8.1°$. It is evident from the shift in phase of the quasi-steady AoA (α_f) that it is due to the inclusion of the 3^{rd} state variable with time delay term (T_p). The effective AoA (α_E) has a smaller phase shift change with repect to the angle of attack and this is from the indicial response for the input α.

The static potential lift coefficient (C_l^{ps}) is given by,

$$C_l^{ps} = C_l^{circ} + C_l^{imp}. \tag{6.14}$$

The first term described in the equation (6.14) is the circulatory lift coefficient and the second term is the impulsive lift coefficient as a result of the mass component.

$$C_l^{imp} = \frac{\pi c(U_0\dot{\alpha} + \dot{U}_0\alpha + \ddot{h})}{2U_0^2}, \tag{6.15}$$

where, $\ddot{h}$ is the pluging acceleration and $\dot{U}_0$ is the velocity acceleration term. As the plunging component is zero in this case and the $\dot{U}_0$ term is of less order, the equation (6.15) can be re-written as,

$$C_l^{imp} = \frac{\pi c\dot{\alpha}}{2U_0}, \tag{6.16}$$

$$C_l^{circ} = C_{l,\alpha}(\alpha_E - \alpha_0). \tag{6.17}$$

The dynamic potential lift coefficient (C_l^{ds}) is given by the third state variable as calculated in the equation (6.4) and is given by,

$$C_l^{ds} = x_3. \tag{6.18}$$

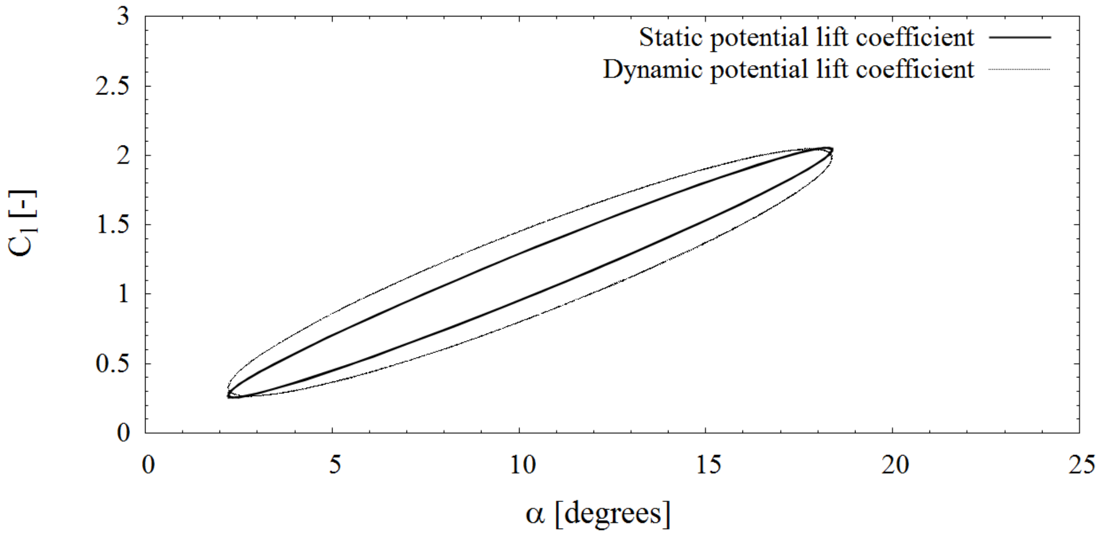

Figure 6.2: Plot of static and dynamic potential lift coefficient at various AoAs.

Figure (6.2) shows the plot of static and dynamic potential lift coefficients for NACA0012 airfoil undergoing pitching. The delay in the onset of the dynamic stall accounted by the time constant T_p, leads to increases in the dynamic potential lift compared to that of static potential lift coefficient. This is evident from the Figure (6.2).

6.2.3 Separated flow

The original LB model uses empirical correlation to determine the dimensionless static separation point (f_{st}) as stated in the equation as follows,

$$\begin{aligned} f_{st} &= 1 - 0.3 \quad e^{\frac{\alpha-\alpha_0}{S_1}}, \quad \text{if } \alpha > \alpha_0, \\ f_{st} &= 0.04 + 0.66 \quad e^{\frac{\alpha-\alpha_0}{S_2}}, \quad \text{if } \alpha < \alpha_0, \end{aligned} \tag{6.19}$$

where S_1 and S_2 are experimentally determined constants. The lift coefficient for simple trailing edge separated flow is given by Kirchoff and can be rearranged to obtain the f_{st} as described in the equation below

$$f_{st} = (2\sqrt{\frac{C_l^{st}}{C_{l,\alpha}(\alpha - \alpha_0)}} - 1)^2. \tag{6.20}$$

The relation is obtained in such a way that the separation point is always between 0 and 1 as this is the non-dimensional chord length of the airfoil. This correlation is implemented in the model as it does not require any experimentally determined constants.

Figure (6.3) shows the non-dimensional static separation point for various AoAs for NACA0012 airfoil stalling at 13°, with the above mentioned mean AoA and amplitude of pitching airfoil.

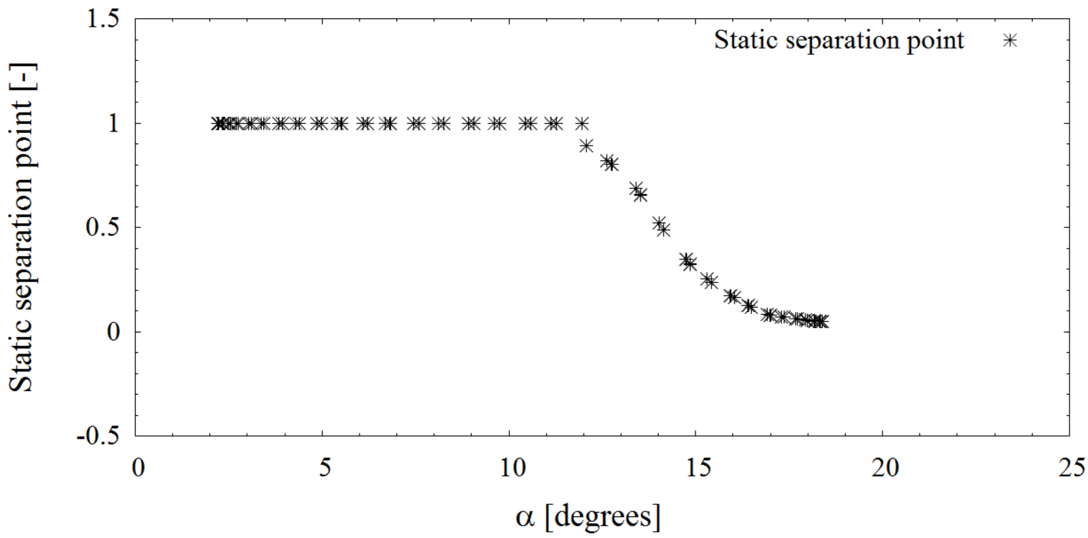

Figure 6.3: Non-dimensional static separation point for various AoAs.

The lift coefficient for fully separated flow is obtained as described by the following equations based on whether the flow is separated or attached respectively

$$C_l^{fs} = \frac{C_l^{st} - C_{l,\alpha}(\alpha - \alpha_0) f_{st}}{1 - f_{st}}, \tag{6.21}$$

$$C_l^{fs} = \frac{C_l^{st}}{2}. \tag{6.22}$$

The non-dimensional dynamic separation point (f_{dy}) is obtained as the 4^{th} state variable from the equation (6.4) along with α_f instead of α using the equation (6.20). The dynamic separation point is indicated in the Figure (6.4) for NACA0012 airfoil.

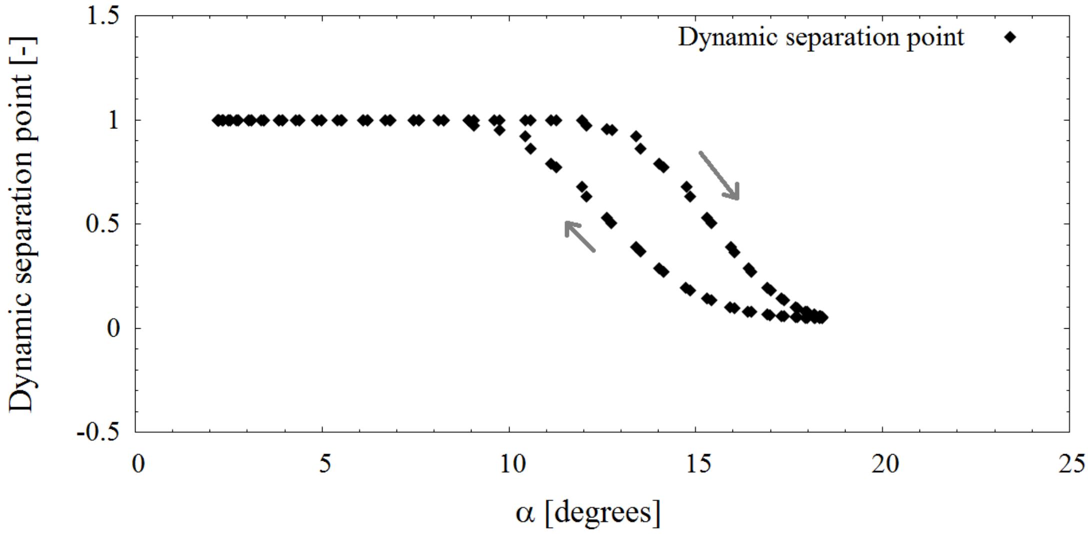

Figure 6.4: Non-dimensional dynamic separation point for various AoAs.

(Figure 6.4) shows dynamic separation point as a function of α. It can be seen that the flow remains attached when the angle of attack increases until the separation point just before the stall angle of 13°. In this region the dynamic separation point remains equal to one. Once the separation sets in, the separation point drops less than one and move towards the leading edge as long as α is increased. On pitching the airfoil to decrease α, the separation point increases and the flow tends to reattach but at an angle very small compared to the onset of separation in upward stroke. This hysteresis behaviour is expected in dynamic stall due to the delays associated with the phenomena.

6.2.4 Vortex lift contribution

Dynamic stall phenomena involves the formation of leading edge vortex and disappearance of the same at a later point of time. The contribution of lift from the leading edge vortex formed is given by the relation,

$$C_v = C_l^{circ}(1 - \frac{(1+\sqrt{f_{dy}})^2}{4}), \tag{6.23}$$

where, C_v is the increment of the vortex lift calculated as a difference between the circulatory lift coefficient given in equation (6.17) and the lift coefficient from Kirchoff's relation given in equation (6.20). The vortex lift is given by,

$$C_l^{vor}{}_n = C_l^{vor}{}_{n-1} \quad e^{\frac{\Delta s}{T_v}} + (C_{v_n} - C_{v_{n-1}})e^{\frac{\Delta s}{2T_v}}, \tag{6.24}$$

where, Δs is the change in dimensionless time constant and T_v is the time constant for vortex lift contribution. Following this, the total lift coefficient can also be calculated as a combination of fully attached, fully separated lift coefficient and vortex lift coefficient based on the dynamic separation point

$$C_l^{ds} = C_{l,\alpha}(\alpha_E - \alpha_0)x_4 + C_l^{fs}(1 - x_4) + \frac{\pi \dot{\alpha} c}{2U_0} + C_l^{vor}. \tag{6.25}$$

Figure (6.5) shows the plot of dynamic lift coefficient along with the dynamic separation point for S809 airfoil. The dynamic phenomena is shown for pitching airfoil with mean angle (C) 13° and amplitude (D) 10.2°. The numbers in the figure indicate different states. During the pitching up motion of airfoil, the flow remains attached from state one to state two. At state two, the separation starts which is indicated by dynamic separation point becoming less than one. At state three, the separation point reaches the leading edge of the airfoil and the formed leading edge vortex begins to convect. Therefore the lift coefficient decreases further. Then the flow reattaches at state four. During the pitching down motion of airfoil, the dynamic lift coefficient changes but with the hysteresis.

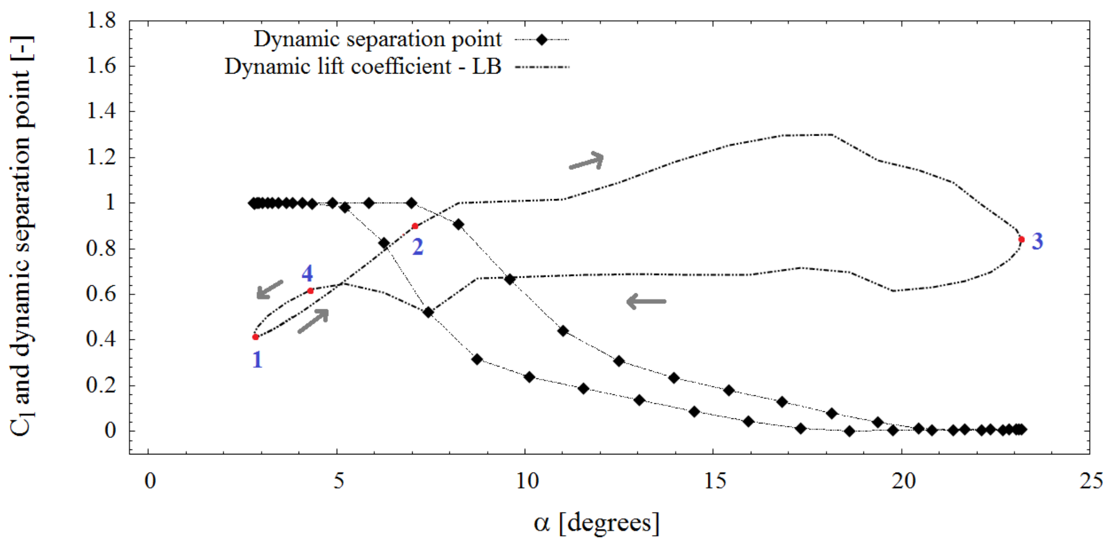

Figure 6.5: Plot of dynamic lift coefficient for S809 airfoil from LB model with non-dimensional dynamic separation point.

The formulated dynamic stall model has to be validated with an experiment. The wind tunnel experimental results of Ohio state University [37] conducted at Reynolds number of $1.2 \cdot 10^6$ for S809 airfoil is used to compare with the LB model.

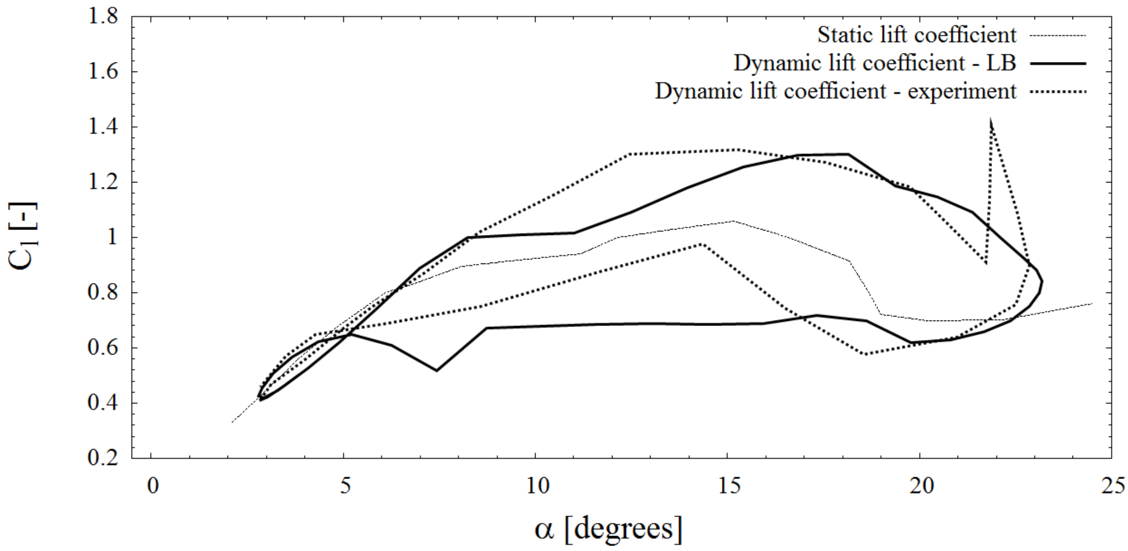

Figure 6.6: Plot of dynamic lift coefficient from LB model and experiment for S809 airfoil at reduced frequency of k=0.042 .

Figure (6.6) shows the dynamic stall lift coefficient from LB model and experiment along with that of static stall lift coefficient. The dynamic phenomena is shown for pitching airfoil with $C = 13°$ and $D = 10.2°$. During the upward stroke, the dynamic lift coefficient increases and the stall is delayed with the overshoot in the maximum lift. This phenomena is due to the vortex formation in the leading edge causing the pressure to drop thereby increasing the lift. However, the formed vortex is highly unstable and so it is convected downstream and as a result the lift drops. During the beginning of downstroke of the airfoil, the lift coefficient increases again, but with the expected hysteresis. Then the lift coefficient follows the hysteresis for the remaining of the downstroke. From the result, it can be seen that the dynamic stall model is in good agrement with that of the experiment expect in some regions in downstroke. Also, there is discrepancy in the model to predict the peak at the maximum AoA. The discrepancy could be the result of the assumed constants and time lags which are originally developed for the compressible flows. Further, the constants used for the attached flow model of LB are experimentally determined based on Theodorson theory which is applciable for airfoil of maximum 15% thickness but the airfoil used here is S809 which is 21% thick.

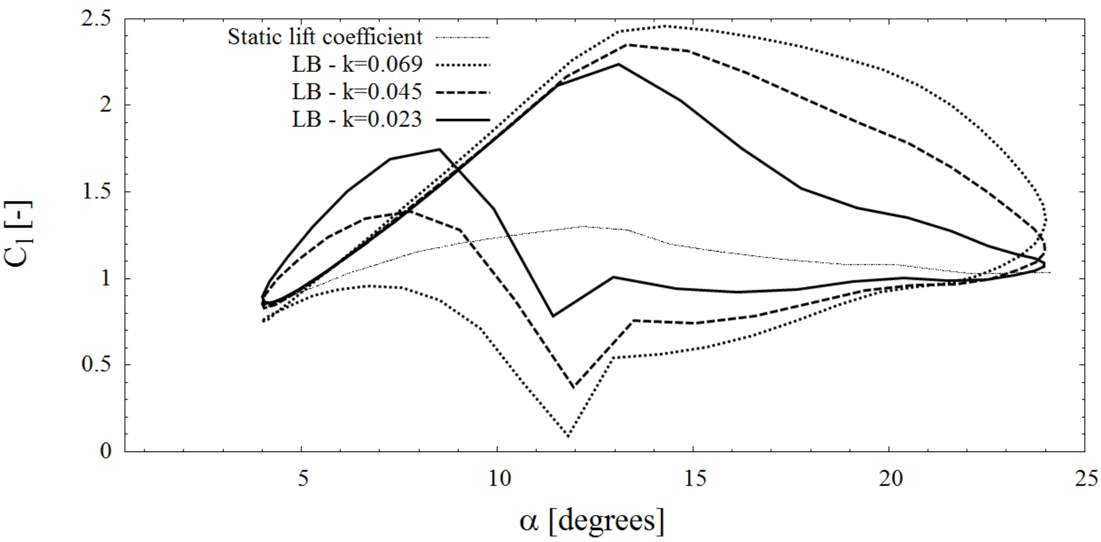

Figure 6.7: Plot of dynamic lift coefficient from LB model for NACA4415 airfoil at reduced frequency of k=0.023, k=0.042 and k=0.069 .

Figure (6.7) shows the plot of dynamic stall lift coefficient for pitching NACA4415 airfoil at the Reynolds number of $1.2 \cdot 10^6$ with $C = 14°$ and $D = 10°$. The plot includes the dynamic stall model at three different reduced frequencies namely $k = 0.023, k = 0.045$ and $k = 0.069$. The plot clearly shows that increasing the pitching frequency changes the hysteresis loop. The higher pitching frequency ($k = 0.069$) results in increased lift coefficient in the upward pitching motion and reduction of the same during the downward motion compared to smaller pitching frequency ($k = 0.045$). This is the expected physical behaviour and the model captures this behaviour with a fairly good accuracy.

Chapter 7

Conclusions and further work

7.1 Double wake invscid method

The separated flow is marked by the flow reversal and vortex shedding. In the potential unsteady flow, the vortex shedding is modelled with the vortex blobs, vortex rings or filaments evolving with time and convected downstream from the seperation point. In steady state approach, the vorticity convection in the separated potential flow is modelled with the wake sheets evolving from the trailing edge and from the separation point. Unlike the previous works of steady state simulation with vortex method which uses wake factor or predetermined shape to determine the initial wake shape, the present implementation is based on the induced velocities from the airfoil surface vortices with negligible local vorticity at the immediate downstream of the separation point. The negligible local vorticity is to convect the wake downstream from the separation point. Two vortex sheets of opposing vortices as a result of Kutta condition, leads to isolated region in between the two wakes. The Kutta condition facilitates the constant pressure region. With the help of Bernoulli's theorem the pressure jump for the separated region is added and accurate pressure distribution is calculated. In the potential flow, vorticity is a kinematic property and once created can only be convected (based on Kelvin's ciruclation theorem). This convected vorticity along the wakes sheet is used to calculate the source of the vorticity (i.e. vorticity distribution over the airfoil surface) in every iteration. This process of regulating the vorticity production based on the convected vorticity make the solution intact in the separated region.

From the results section (5), for all the airfoils namely s825, s826, NACA63415 and FFA-W3-301 tested for various Reynolds number and AoA, it is evident that the inviscid double wake model can give better C_p distribution than XFOIL in the separated flow region with separation point fed from the experimental data. This indicates that the inviscid double wake model is capable of predicting good results if the separation point is known accurately. Also, this method can reproduce results closer to that of experimental and CFD results in the separated flow region. From the initial wake shape to convergence, it takes 4 to 6 iterations to get the final results. Further, it is evident from the analysis of S826 airfoil at very high AoA, where viscous solution is unavailable from industry standard aerodynamic design tool (RFOIL) owing to convergence failure, the double wake inviscid model gives accurate result in the separated region. Combining the double wake inviscid model with viscous calculation for these high AoA would help in overcoming the convergence problem. Also, this combination is expected to improve the lift prediction.

There are few shortcoming of this double wake inviscid approach: Firstly, the small hump occurs at the separation point due to the wake release. Secondly, in the non-separated flow region, the calculated C_p lacks accuracy in comparison to the experiment or CFD data as there are no viscous effects. These deficits can be overcome by coupling the double wake inviscid model with the viscous effects which is explained later in the section. The other limitation is that the separation location has to be provided externally for the double wake inviscid model. The separation point can be obtained from the first iteration of single wake inviscid-viscous calculation (RFOIL) where the skin friction becomes negative indicating flow separation for steady state solution. However, for high angle of attacks, this is not feasible due to convergence failure with single wake inviscid-viscous calculations.

The results obtained by inviscid double wake model shown in section (5) include both conventional sharp trailing edge and blunt trailing edge airfoils and the pressure distribution is predicted very accurately in the separated flow region. Hence as a future work the same implementation procedure as described below, can be followed in RFOIL for all the airfoils. As the region enclosed between the double wake has negligible vorticity i.e. negligible shear, no velocity correction is required from the viscous flow for the separated region. Figures (7.1) and (7.2) show the viscous-inviscid solution scheme for RFOIL and coupling of viscous effects with the double wake inviscid model, respectively.

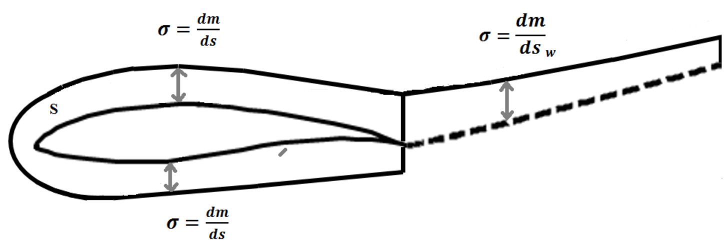

Figure 7.1: RFOIL viscous-inviscid scheme.

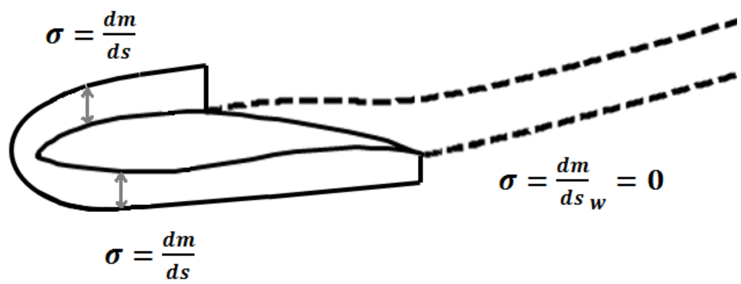

Figure 7.2: Viscous coupling with double wake inviscid model.

In RFOIL, the inviscid solution is calculated and the viscous effects are added through strong viscous-inviscid coupling. This is done starting from the stagnation point and marching towards the trailing edge in the pressure side and towards the trailing edge and along the wake in the suction side of the airfoil. For coupling the double wake inviscid model with viscous effects, the converged double wake solution would be fed as input and the viscous correction can be obtained with strong coupling only in the non-separated flow region. The solution scheme here is obtained by marching from the stagnation point towards the trailing edge in the pressure region and till the point of separation in the suction side of the airfoil. This implementation can overcome the present convergence problem of RFOIL in the separated flow region and expected to improve the lift prediction. After the viscous coupling with the double wake inviscid model, the influence of number of wake panels on the solution for wide variety of airfoils and at different angles needs to be studied.

7.2 Dynamic stall model

The Leishman-Beddoes (LB) dynamic stall model is implemented for pitching airfoil for a wind turbine application. The semi-empirical LB model uses minimum number of constants and all the other inputs can be provided from the static airfoil results. This makes the model efficient for different airfoils and more reliable. The model captures the dynamic flow phenomena effectively and predicts lift coefficient at different pitching frequency replicating the physical behaviour, which are evident from the results. It can model the hysteresis behaviour of the dynamic stall closer to experimental results but there are some discrepancies in the values of the dynamic lift coefficient which is possibly due to the use of the constants that are essentially for the compressible flows. Further, Theodorson theory is used to calculate the separation point to avoid two other empirical conatnts. This limits the usage of the model for thin airfoils of thickness less than 15%.

Bibliography

[1] M. Vezza and R. A. McD. Galbraith. An inviscid model of unsteady aerofoil flow with fixed upper surface separation. *International Journal for Numerical Methods in Fluids*, 5(6):577–592, 1985.

[2] N. R. Garcia. *Unsteady Viscous-Inviscid Interaction Technique for Wind Turbine Airfoils*. PhD thesis, Technical University of Denmark, April 2011.

[3] V. A. Riziotis and S. G. Voutsinas. Dynamic stall modelling on airfoils based on strong viscous - inviscid interaction coupling. *International Journal for Numerical Methods in Fluids*, 56:185–208, 2008.

[4] A. Zanon and P. Giannattasio. *A vortex panel method for vawt in dynamic stall*. PhD thesis, Università degli Studi di Udine, 2011.

[5] L. Marion, N. R. Garcia, and J. N. Sørensen. Inviscid double wake model for stalled airfoils. *Journal of Physics: Conference Series*, 524(1):012132, 2014.

[6] J. Katz and A. Plotkin. *Low-Speed Aerodynamics , Second Edition*, volume 2. Cambridge university press, 2010.

[7] R.P.J.O.M. van Rooij. Modification of the boundary layer calculation in RFOIL for improved airfoil stall prediction. Technical Report IW-96087R, Delft University of Technology, Delft, The Netherlands, 1996.

[8] M. Drela. XFOIL: An Analysis and Design System for Low Reynolds Number Airfoils. In *Low Reynolds Number Aerodynamics*, pages 1–12. Springer Berlin Heidelberg, 1989.

[9] G. Ramanujam, H. Ozdemir, and Harry W. Hoeijmakers. Improving Airfoil Drag Prediction. *34th Wind Energy Symposium*, (January):1–12, 2016.

[10] G. Ramanujam and H. Özdemir. Improving airfoil lift prediction. In *35th Wind Energy Symposium*, number AIAA 2017-1999 in AIAA SciTech Forum, Grapevine, Texas, 9-13 January 2017.

[11] M. Drela and M. B. Giles. Viscous-inviscid analysis of transonic and low Reynolds number airfoils. *AIAA Journal*, 25(10):1347–1355, 1987.

[12] M. Drela. Integral boundary layer formulation for blunt trailing edges. *AIAA Journal*, (10), 1989.

[13] M. Drela and M. B Giles. Viscous-Inviscid Analysis of Transonic and Low Reynolds Number Airfoils. *American Institute of Aeronautics and Astronautics Journal*, 25(2):1–9, 1986.

[14] P. Dini and M. D. Maugmer. A computationally efficient modelling of laminar separation bubbles. Technical Report NAG-1-778, The Pennsylvania State University, July 1990.

[15] S. G. Voutsinas and V. A. Riziotis. A viscous-inviscid interaction model for Dynamic stall simulations on airfoils. *American Institute of Aeronautics and Astronautics*, pages 185–208, 1999.

[16] N. R. Garcia, A. Cayron, and J. N. Sørensen. Unsteady Double Wake Model for the Simulation of Stalled Airfoils. *Journal of Power and Energy Engineering*, 3:20–25, July 2015.

[17] B. C. Basu and G. J. Hancock. The unsteady motion of a two-dimensional aerofoil in incompressible inviscid flow. 87:159–178, 1978.

[18] F. A. Dvorak, B. Maskew, and B. L. Rao. An investigation of separation models for the prediction of $C_{l_{max}}$. Technical Report 6, Analytical methods, Inc., Bellevue, Washington 98004, February 1979.

[19] F. Palacios, M. R. Colonno, A. C. Aranake, A. Campos, S. R. Copeland, T. D. Economon, A. K. Lonkar, T. W. Lukaczyk, T. W. R. Taylor, and J. J. Alonso. Stanford University Unstructured (SU2): An open-source integrated computational environment for multi-physics simulation and design. *AIAA*, January 2013.

[20] K. F. Sagmo, J. Bartl, and L. Sætran. Numerical simulations of the NREL S826 airfoil. *Journal of Physics: Conference Series*, 753, 2016.

[21] N. Y. Aksnes. Performance Characteristics of the NREL S826 Airfoil. *M.Sc. Thesis - Norwegian University of Science and Technology*, 2015.

[22] C. Bak, P. Fuglsang, J. Johansen, and A. Ioannis. Wind Tunnel Tests of the NACA 63-415 and a Modified NACA 63-415 Airfoil. Technical Report Risø-R-1193(EN), Risø National Laboratory, Roskilde, Denmark, 2000.

[23] P. Fuglsang, I. Antoniou, K. S. Dahl, and H. A. Madsen. Wind tunnel tests of the FFA-W3-241, FFA-W3-301 and NACA 63-430 airfoils. Technical Report Risø-R-1041(EN), Risø National Laboratory, Roskilde, Denmark, December 1998.

[24] D. M. Somers and J. Tangler. Design and Experimental Results for the S825 Airfoil. Technical Report NREL/SR-500-36345, NREL, National Renewable Energy Laboratory, January 2005.

[25] H. Schlichting. *Boundary Layer Theory.* Mc Graw Hill, eighth edition, 1979.

[26] J. G. Leishman and G. L. Crouse. State-space model for unsteady airfoil behavior and dynamic stall. *AIAA/ASME/ASCE/AHS/ASC 30th Structures, structural dynamics and materials Conferences. Mobile, Alabama*, (89-1319):11, April 3-5 1989.

[27] J. G. Leishman. *Principles of Helicopter Aerodynamics, Second Edition.* Cambridge university press, 2006.

[28] T.S.R. Reddy and K.R.V. Kaza. A comparative study of some dynamic stall models. Technical report, March 1987.

[29] T. Theodorsen and L. E. Garrick. General potential theory of arbitrary wing sections. Technical Report 452, National advisory committee for aeronautics, 1940.

[30] W. Sheng, R. A. McD. Galbraith, and F. N. Coton. A Modified Dynamic Stall Model for Low Mach Numbers. *Journal of Solar Energy Engineering*, 130(3):031013, 2008.

[31] T. S. R. Reddy and K. R. V. Kaza. Analysis of an unswept propfan blade with a semiempirical dynamic stall model. Technical Report NASA-TM-88917, The University of Toledo and Lewis Research Center, Ohio, 1989.

[32] J.G. Holierhoek, J. B. de Vaal, A. H. van Zuijlen, and H. Bijl. Comparing different dynamic stall models. *Wiley Online Library*, 2012.

[33] T. S. Beddoes and J. G. Leishman. A Semi-Empirical Model for Dynamic Stall. *Journal of the American Helicopter Society*, 34(3):3–17, 1989.

[34] M. H Hansen, M. Gaunaa, and H. A. Madsen. A Beddoes-Leishman type dynamic stall model in state-space and indicial formulations. Technical Report Risø-R-1354(EN), Technical University of Denmark, 2004.

[35] J. G. Leishman and T. S. Beddoes. A semi-empirical model for dynamic stall. *American Helicopter Society*, page 15, June 1986.

[36] J. W. Larsena, S. R. K. Nielsena, and S. Krenk. Dynamic stall model for wind turbine airfoils. *Journal of Fluids and Structures*, (0889-9746):959–982, May 2007.

[37] J. B. de Vaal. Heuristic modelling of dynamic stall for wind turbines. Technical Report IW-96087R, Delft University of Technology, Delft, The Netherlands, 2009.

[38] C. Chantharasenawong. *Nonlinear Aeroelastic Behaviour of Aerofoils Under Dynamic Stall*. PhD thesis, May 2007.